The Hong Kong Polytechnic University

Department of Electrical Engineering

Design and Optimisation of the Performance of Switched Reluctance Motor Drives

Ka Fai WONG

A thesis submitted in partial fulfilment of the requirements
for the Degree of Doctor of Philosophy

August, 2008

CERTIFICATE OF ORIGINALITY

I herby declare that this thesis is my own work and that, to the best of my knowledge and belief, it reproduces no material previously published or written, nor material that has been accepted for the award of any other degree or diploma, except where due acknowledgement has been made in the text.

_______________________ (Signed)

______WONG Ka Fai______ (Name of Student)

Dedication

To my parents, Siu Hing and Kwok Ming

Abstract

Switched reluctance machine (SRM) has been gaining increasing attentions from researchers and industries decades ago. Because of its simple mechanical structure, low moment of inertia, high power density, low manufacturing cost, and high reliability, it is considered as a strong competitor to induction motor. Because SRM usually operates in regions of high magnetic saturation in order to realise high power density, there are inevitable nonlinearities among flux-linkage, phase current, electromagnetic torque and rotor position. Nonlinearities complicate SRM drive system simulation studies, which are now becoming indispensable tools for performance evaluation and controller design. SRM also suffers from having a relatively high torque ripple using simple current control. Hence, the use of SRM in applications demanding high performance becomes challenging. This thesis concentrates on studies of SRM in respect to non-linear computer simulation model, online torque estimation, instantaneous torque control and position control.

A computer simulation model with nonlinear magnetic and torque characteristics is presented. Since the model is developed under MATLAB/ SimPowerSystems, it can be used to simulate SRM, power drive and its associated control algorithm simultaneously. User defines the magnetic data and considers both self and mutual coupling as well as the necessary mechanical parameters which are acquired from experiments. The configuration of the power drive and control algorithm can be altered using appropriate graphical user interface. Simulation results show that the model is accurate and effective, as all the simulation results obtained from the developed model have been fully validated experimentally.

To estimate the electromagnetic torque online, a torque estimator for SRM under hysteresis current control is proposed. The co-energy of the phase is estimated based on a few pre-measured machine parameters. The co-energy, rotor position and phase current are stored in the memory. In the next switching cycle that follows, the newly estimated co-energy and the stored value are used to estimate the instantaneous torque using the principle of co-energy. Simulation and experiment results demonstrate that the outputs of the proposed estimator are similar to those based on cubic spline model.

In regard to torque ripple reduction, a torque controller based on co-energy control is developed. For this controller a co-energy profile is firstly deduced from pre-measured low-current magnetic characteristics of the SRM. Since co-energy is proportional to the electromagnetic torque in both linear and nonlinear regions, the required co-energy can be calculated from the co-energy profile and torque command. With the use of an online co-energy estimator, the controller can regulate the co-energy to follow the command. Computer simulation and experiment confirm that under co-energy control, the torque contribution of each phase can be controlled to reduce output torque ripple significantly. In addition, the controller requires less memory and less pre-measured machine data, in contrast to traditional current control schemes. The torque controller is then extended from one-quadrant to four-quadrant operation, to achieve torque ripple reduction in both motoring and generating modes at both directions.

An algorithm for rotor position control is developed on top of the torque control scheme. The position control loop and torque control system are connected in cascade. The position controller and co-energy controller are designed utilising the principles of two-degree of freedom internal model control, which is a model-based controller with improved disturbance rejection. The parameters of the controllers are expressed in terms of basic machine parameters and user-selected system response time constants. The simulation and laboratory outputs of the systems ascertain the robustness of the proposed algorithm against parameter mismatch.

Publications Arising from this Thesis

During the period of study, 3 journal papers and 2 international conference papers have been produced, where one journal paper has been published, and two journal papers have been accepted, while one conference paper has been presented and one has been accepted. The details of the papers are listed below:

[1] Wong, K. F., Cheng, K. W. E., Ho, S. L., and Yang, S. Y.: ‘Online torque estimator of switched reluctance motor running under hysteresis current control’. 12th Biennial IEEE Conference on Electromagnetic Field Computation 2006, April–May 2006, Miami, Florida, USA, pp. 332

[2] Wong, K. F., Cheng, K. W. E., and Ho S. L.: ‘Simulation of switched reluctance motor based on a combination of circuit-oriented and signal-oriented approaches using Matlab/SimPowerSystems’, *Electr. Power Comp. Sys.*, 2007, **35**, (2), pp. 205–219

[3] Wong, K. F., Cheng, K. W. E., and Ho S. L.: ‘Instantaneous torque control of switched reluctance motor based on co-energy control’, *IET Electr. Power Appl.*, (accepted for publication)

[4] Wong, K. F., Cheng, K. W. E., and Ho S. L.: ‘Four-quadrant instantaneous torque control of switched reluctance machine at low speed based on co-energy control’, *IET Electr. Power Appl.*, (accepted for publication)

[5] Wong, K. F., Cheng, K. W. E., and Ho, S. L.: ‘Low cost high-side gate drive power supply for switched reluctance machines’. International Conference on Power Electronics Systems and Applications 2009, (accepted)

Acknowledgements

I would like to express my gratitude to my supervisors, Professor Ka Wai Eric Cheng, Professor Siu Lau Ho, and Dr. Tze Fun Chan, for their continuous support and guidance throughout the course of study. Their professional knowledge, practical experiences, and rigorous working attitudes nourish my research study. In fact, I enjoy discussions with them, which often inspire many new ideas to help overcoming theoretical difficulties.

I would also thank the technician of the General Power and Machine Laboratory, Mr. Chun Kit Cheung; and the senior technician, Mr. Chun Wing Lee, for their technical support on electrical machine installation and mechanical fitting. Furthermore, I appreciate the administrative supports of the General Office of the department and the Research Office.

I am deeply indebted to my co-workers, Dr. Xiangdang Xue and Dr. Jianfei Pan for their advice and assistance. Their researches on switched reluctance motor help a lot on this project, especially during the initial stage of this project and in the procurement of the necessary testing equipments.

I gratefully acknowledge the supports from the Department of Electrical Engineering, in terms of finance, studentship, and facilities, which form the foundation of this research project.

Lastly, I would like to give special thanks to my parents, Mrs. Siu Hing Wong and Mr. Kwok Ming Wong; and my sister and brother, Mrs. Ka Yuen Lee and Mr. Ka Chung Wong, for their unreserved warm loves and back-up.

Table of Contents

List of Figures

List of Tables

List of Symbols

B	friction coefficient, Nms/rad
e	back electromotive force, V
$F(s)$	transfer function of a low pass filter
F_s	sampling frequency, Hz
$G(s)$	transfer function of a plant
$\hat{G}(s)$	transfer function of a plant model
$G_c(s)$	transfer function of a controller
i_{phase}	phase current, A
J	moment of inertia, kgm^2
k	ratio of bulk inductance to incremental inductance
K_p	proportional constant of proportional-integral controller
l	incremental inductance, H
l_m	modelled incremental inductance, H

L	bulk inductance, H
m	number of phase
p_{jk}	coupling coefficient between phase j and k
$Q(s)$	setpoint filter of 2-degree of freedom internal model controller
$QQ_d(s)$	feedback controller of 2-degree of freedom internal model controller
R	winding resistance, Ω
R_m	modelled winding resistance, Ω
T	phase torque, Nm
T^*	phase torque command, Nm
T_{cmd}	electrical torque command, Nm
T_e	electrical torque, Nm
T_i	integrator constant of proportional-integral controller
T_{load}	load torque, Nm
v_{phase}	phase voltage, V

v_{dc}	DC link voltage, V
V_D	forward voltage drop of power diode, V
V_T	on-state voltage drop of transistor, V
W_c	co-energy of a phase, J
W_c^*	co-energy command of a phase, J
$W_{c\ norm}$	normalised co-energy, J/Nm
ε	filter time constant, s
θ	mechanical rotor position, rad
θ_{ph}	relative rotor position of the phase, rad
θ_{phase}	phase shift of rotor positions between phases, rad
λ	flux linkage, Wb turn
λ_a	flux linkage at the aligned position, Wb turn
λ_u	flux linkage at the unaligned position, Wb turn
λ_{phase}	estimated flux linkage, Wb turn

λ_{jk}	flux linkage of phase *j* due to current *k*, Wb turn
ω	rotor speed, rad/s

1 Introduction

1.1 Background

Switched reluctance machine (SRM), also known as variable reluctance machine, was first constructed in the mid nineteenth century [1, 2]. The development of it, however, slowed down in the early years due to insurmountable limitations arising from switching devices and materials. In the 20's of the twentieth century, variable reluctance stepper motor, which has operating principles similar to those of SRM, was invented for open-loop position control. By the 60's, because of the advancement of power electronics, modern SRM was re-visited for adjustable speed applications. Since then, SRM gains attentions from researchers and industries again. The power drive and machine design advanced significantly towards the later part of last century. With the advent of microprocessors [3, 4] and programmable logic technologies [5–8] in the late 80's, the performances of SRM further improved. They allow implementation of sophisticated control algorithms without complex hardware. High volume and commercial applications of SRM then started. Nowadays, SRM is considered as a potential replacement of induction motor in high-end variable speed drives.

SRM has been applied to numerous industrial and commercial applications. As an example of small power applications, it is used as the servo drive of a Hewlett-Packard plotter, which outputs a maximum power of 53 W. It is also used in air-compressors, washers and door actuator systems. For high-power SRMs, they are finding applications as traction systems by LeTourneau in North America, in electrical coach buses in Mainland China, mine drives in Britain. In addition, SRM is employed as motor/generator for hybrid electric vehicles that require four-quadrant operations.

The major advantages of SRM are attributed to its simple and robust mechanical structure. The rotor has neither windings nor permanent magnets, so the manufacturing and material costs are low. It also tolerates high operating temperature. Because of the rotor construction, the moment of inertia of the rotor is low and the starting torque is high. High-speed operation and wide operating range are permitted. As the rotor and stator of SRM are brushless, the maintenance requirement is as low as that of induction motor. Like induction motor, it can be used in explosive and hazardous environment. Due to the independence of winding phases, multi-phase SRM can endure both short-circuit and open-circuit faults of the winding, although its performance is degraded if such faults have developed.

There are disadvantages in SRM which may restrict their popularity in industrial application. For example, acoustic noise is often observed in SRM because of its double saliency and deep magnetic saturation. In addition, it suffers from having high torque ripples if it is driven by simple current control algorithm. SRM also requires phase commutation for continuous torque production, hence a power converter is necessary. It cannot function with direct on line starting. Position sensor or estimator is needed for commutation, which may increase the maintenance efforts and computational burden. Because of the appearance of non-sinusoidal waveforms, the phase currents are rich in harmonic components. The base frequency of the harmonics is proportional to the rotor speed which obviously is varying, hence the design of harmonic filter becomes difficult and electromagnetic interference is thus a concern.

1.2 Review of researches on switched reluctance motors

1.2.1 Basic principle of SRM

1.2.1.1 Torque production

Fig. 1.1 shows the mechanical structure of an SRM with 8 stator poles and 6 rotor poles (8/6 SRM) with 4 phases. When the windings of phase 1 are excited, flux-linkage develops between the stator and rotor poles. The flux-linkage produces a tendency to align the poles [9], and hence produces an electromagnetic torque in anti-clockwise direction. As the rotor rotates, excitation in phase 1 is extinguished and phase 2 is energised to continue the torque production. If the phases are excited and extinguished consecutively at appropriate rotor positions, a continuous torque is produced. For torque output at the clockwise direction, phase 3 is energised at the time instant as shown in Fig. 1.1. Then phase 2 is excited and so on. The SRM operates in motoring mode when the directions of rotation of the rotor and torque output are the same. It works in the generating mode when the directions are opposite.

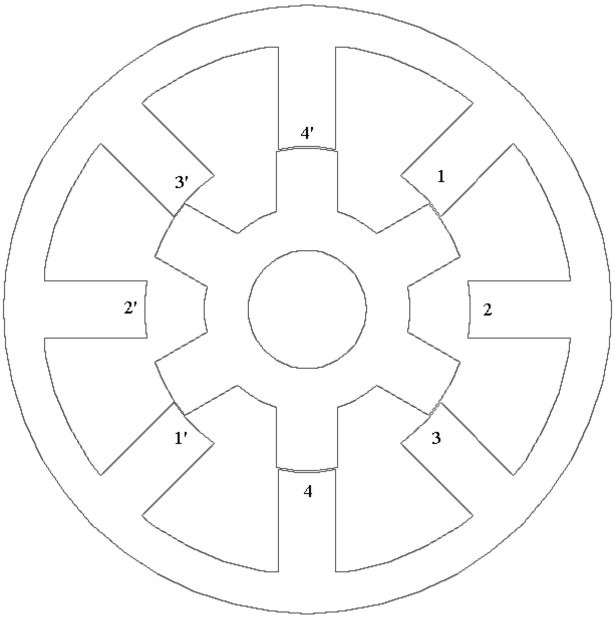

Fig. 1.1 Mechanical structure of an 8/6 SRM

For an SRM without magnetic saturation and mutual coupling [10], the flux linkage λ is expressed as:

$$\lambda(\theta, i) = L(\theta)\, i \tag{1.1}$$

where L is the bulk inductance of the phase, θ is the rotor position, and i is the phase current. The inductance L increases when the overlap between stator and rotor pole faces increases. It reaches a maximum when the poles are aligned with each other and reaches its minimum when the poles are unaligned. Co-energy is defined as:

$$W_c(\theta, i) = \int_0^i \lambda(\theta, i)\, di \tag{1.2}$$

By substituting (1.1) into (1.2), the co-energy of the phase is:

$$W_c(\theta, i) = \frac{1}{2} L i^2 \tag{1.3}$$

The instantaneous electromagnetic torque output of the phase, which is the derivative of the co-energy with respect to rotor position, is:

$$T(\theta, i) = \left. \frac{\partial W_c}{\partial \theta} \right|_{i=\text{constant}} \tag{1.4}$$

Substituting (1.3) into (1.4), the torque is expressed as:

$$T = \frac{1}{2} i^2 \frac{dL}{d\theta} \tag{1.5}$$

From (1.5), one can observe that the direction of torque is independent of the direction of the phase current. It is, instead, dependent on the slope of the inductance profile. Also, the magnitude of the torque is proportional to the square of the phase current at each rotor position.

In order to make full use of the magnetic materials so as to make the machine more compact, SRM is often driven into regions with deep magnetic saturation. The relationships among bulk inductance of the phase, phase current, and rotor position become non-linear functions, as demonstrated by the laboratory measurement shown in Fig. 1.2, where 0° and 30° correspond to the unaligned and aligned positions, respectively. The profile between 30° and 60° is the mirror image of that between 0° and 30° along the aligned position. The profile repeats afterwards with a period of 60°.

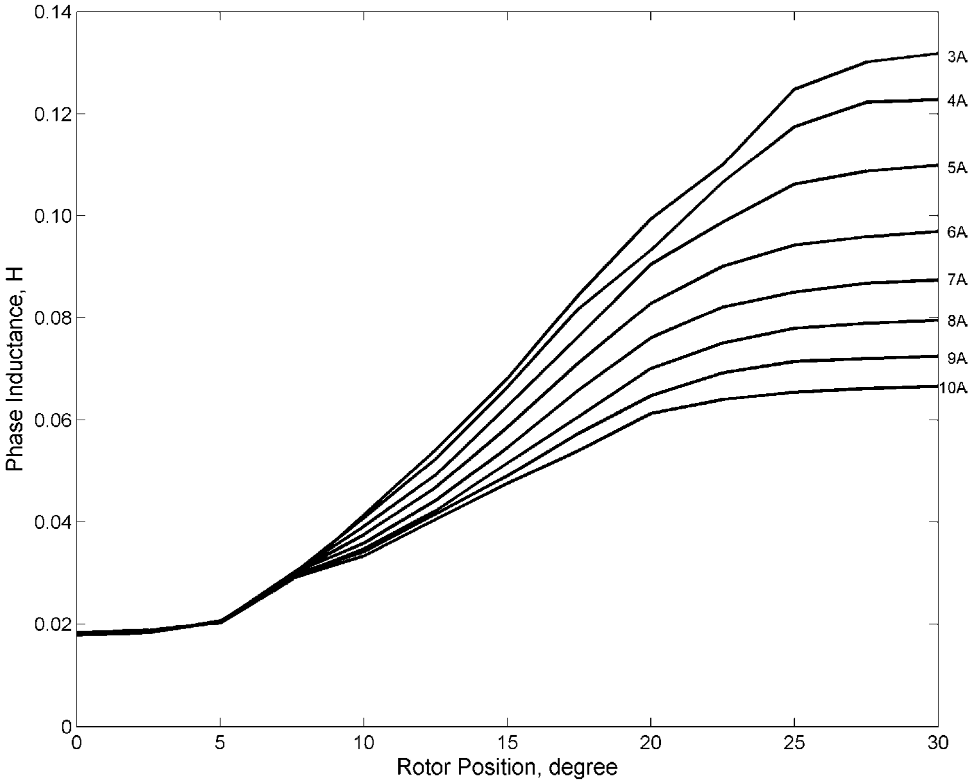

Fig. 1.2 Inductance profile of an 8/6 SRM with different phase current

At the unaligned position, the phase inductance changes slightly with the phase current, because of the relatively long airgaps between poles. At the aligned position, the inductance decreases significantly with an increase in current. It is because the airgaps become shorter and the poles are saturated at high current.

The concepts of co-energy as shown in (1.2) and (1.4) are applicable to cases with magnetic saturation. However, the integral for co-energy calculation cannot be evaluated directly because of non-linearity, unless an analytic model of inductance or flux linkage is available. Applying numerical integration to (1.2) and numerical differentiation to (1.4), the phase torques derived from the experimental magnetic data are depicted in Fig. 1.3.

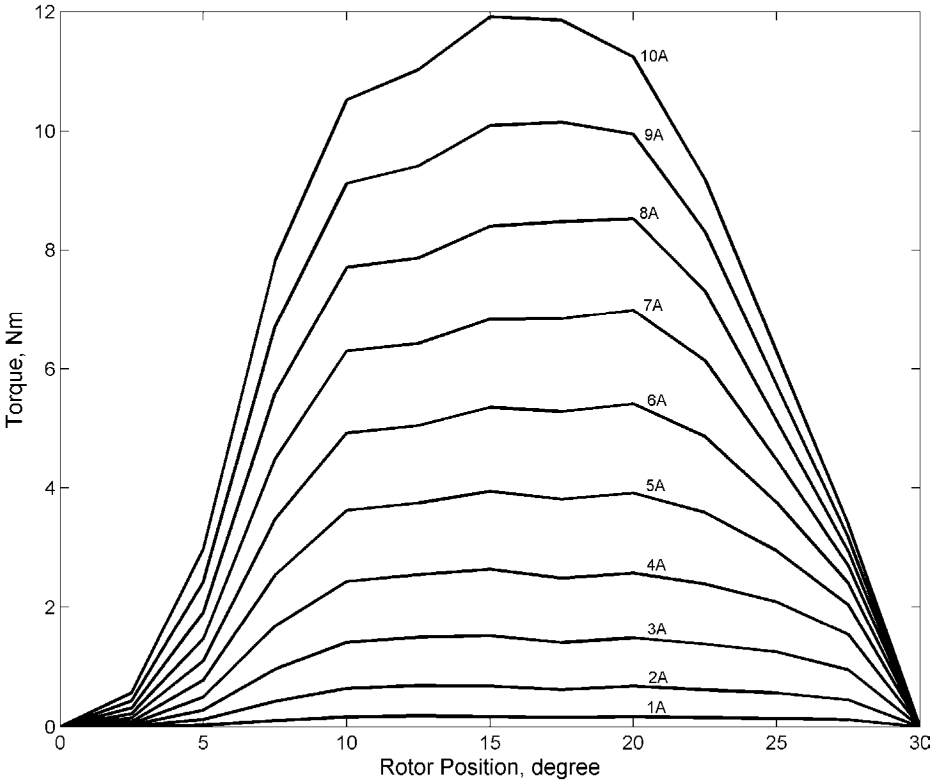

Fig. 1.3 Phase torque of an 8/6 SRM with different phase current

1.2.1.2 Traditional power drive and control

As the windings of SRM only require unidirectional current flow [11], asymmetric half-bridge is a commonly used topology for the power drive. One phase of the bridge is shown in Fig. 1.4. When both transistors are switched on, the voltage of the DC-link is applied to the winding. Energy is transferred from the DC-link into the winding. While current is conducting through the winding, if one of the transistors is off, the winding is in free-wheeling mode and receives zero voltage. When both transistors are off, the DC-link voltage is applied with a reversed polarity until current ceases. The energy stored in the windings is therefore reverted back to the DC-link.

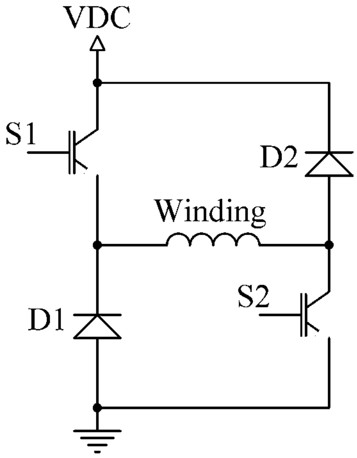

Fig. 1.4 Asymmetric half-bridge for one phase of SRM

The equation describing the electrical dynamics of a phase winding is:

$$v = iR + \frac{d\lambda}{dt} \tag{1.6}$$

$$v = iR + l\frac{di}{dt} + \frac{d\lambda}{d\theta}\omega \tag{1.7}$$

where v is the applied voltage across the winding, R is the winding resistance, l is the incremental inductance of the phase, and ω is the rotor speed. The last term is considered as the back-electromotive force (back-EMF), which is proportional to the speed at each rotor position.

For low speed applications, pulse-width modulation (PWM) current control [12] is usually employed to control the SRM. The most simple control strategy is hysteresis control. A hysteresis band is set for the phase current. When the relative rotor position of the phase is in the active region, the transistors are switched on to energise the winding. If the current meets the upper bound of the band, one or both of the transistors are switched off. When the current drops to the lower bound, both transistors are on again to excite the winding. The process repeats itself to keep the current within the band, until the rotor position is out of the active region. In the inactive region, both transistors are off to extinguish the current. Under this control scheme, the user has to specify the active region and defines the current hysteresis band for the controller.

As an alternative, PWM current control can be implemented with a constant frequency PWM instead of hysteresis. A current feedback controller varies the duty cycle of the PWM voltage to regulate the phase current according to the command value. The harmonic contents of the voltage and current are more predictable than those under hysteresis control, and can be filtered readily. In addition, the current and torque waveforms contain less high-frequency ripples if PWM current control is employed.

For high-speed operations, single pulse mode is used. Both the transistors are turned on in the active region and turned off in the inactive region. There is no chopping for current regulation. The current waveform is determined by the phase inductance and back-EMF. To control the current, only the period and positions of the active region can be altered. The operation mode usually changes from PWM current control to single pulse mode automatically as the rotor speed increases when the back-EMF increases to a level which is higher than the DC-link voltage. In other words, the DC-link voltage is insufficient to overcome the back-EMF and regulate the current in single pulse mode.

1.2.2 Computer simulation

Computer simulation is increasingly indispensable for the performance evaluation of SRM and for the design of its controllers, because the implementation of hardware prototype is generally very expensive and time consuming. Computer simulation algorithms can be broadly classified into position domain and time domain categories.

1.2.2.1 Position domain simulation

Early stage of computer simulation focuses on the analysis of magnetic characteristics. With the knowledge of geometric and magnetic data, finite element method (FEM) [9, 13, 14], and magnetic circuit [15] are used to analyse the flux linkage and torque output of SRM. By repeating with different phase currents and rotor positions, a profile of magnetic and torque data can be obtained. Although the result is accurate and the method is useful for machine design, it is computationally very expensive. Even with modern computers, FEM still takes a long time to obtain its solution. Also, it cannot simulate the design of controller, which usually operates in time domain rather than position domain.

Because of the drawbacks of using FEM, some researchers develop analytical models to describe the magnetic features of SRM. With some flux data points obtained from calculation [16], FEM [17, 18], or measurement [19, 20], analytical models are developed to interpolate the data [21]. Since there are analytical expressions of the magnetic characteristics, the torque expression can be derived. It can simulate simple control algorithms, such as single-pulse mode [17, 19]. The flux-linkage and current are computed, while the rotor position is changed in steps.

Although the analytical models are less accurate than FEM, they are usually sufficient for the preliminary design of SRM with moderate computational burden. However, the use of analytical models in position domain, as with FEM, cannot simulate the controller, especially for applications to motion control, which requires time domain simulation.

1.2.2.2 Time domain simulation

Because of the advent of power electronic control which stimulates renew interests on SRM, many researchers utilise electronic circuit simulation software to study the behaviour of SRM in time domain. Commonly used software package includes SPICE [22–25], TCAD [26], Saber [27, 28], and EMTP [29, 30]. The magnetic model of an SRM is converted into a circuit model, which usually consists of variable inductances and voltage sources. The flux-linkage and torque are represented by equivalent voltage or current signals. The circuit is then connected to the power drive and controller that are constructed from the circuit library. The method has been found to simulate the performance of power electronic switching accurately. However, the need to convert the magnetic model and controller into their corresponding equivalent circuit is the major drawback of this approach. If complex digital control algorithms are modelled, the conversion is tedious and inflexible.

Instead of circuit simulators, a signal simulator, MATLAB/Simulink, is also commonly used to simulate SRM [31–34]. The SRM model is described with signal flow under Simulink, and is then connected to a controller. Depending on the required level of simulation details, the effects of power drive can be studied after converting the controlling sequence into signal flow. As Simulink contains a wealth of libraries for signal processing and control, one can rapidly develop sophisticated control algorithms without extensive effort of programming. Also, it permits seamless connection to external hardware for prototyping and tuning of parameters. The signal simulator approach is commonly employed to design controller, and in the analysis of its interaction with SRM. In contrast to that of circuit simulator, the drawback of signal simulator is the need to convert the power drive into signal flow.

Some researchers prefer using customised programmes, for example using MATLAB/M-file [35] and Pascal [21], for simulation. The developers have to write programmes to calculate the states of the machine, power drive and controller, and then perform numerical integration to move one step at a time. The process repeats until the end condition is met. It offers good flexibility for modelling and simulation, at the expense of heavy programming effort. Since it does not take advantage of readily available libraries, the initial development based on such approach may require a long time and it is therefore expensive.

For high accuracy simulation, field-circuit-motion coupled simulation with FEM [36– 40] is used. The electronic circuit, magnetic field and mechanical motion are coupled as a single problem. At each time-step, the solution is solved with FEM. After stepping through the simulation period, a time series of circuit, magnetic and mechanical states is obtained. The major advantage of this method is the very high accuracy of the solution, as the simulator considers all three domains simultaneously and iteratively refines the numerical solution. However, this method has high computation and data storage requirements, which is not preferable for quick evaluation of performance.

1.2.3 Torque estimation and control

To control the torque output of SRM for high-grade control, it is natural to estimate the torque online first. Average torque [41] generated by each phase can be estimated with the principle of co-energy loop, which is estimated from the product of the phase current and flux-linkage. For instantaneous torque estimation, look-up tables [42, 43] are used. Phase current, and flux-linkage or rotor position, are the inputs of the tables obtained using *a priori* measurement. The major flaw of this scheme is the large data storage of the tables. To reduce the memory requirement on the pre-stored magnetic data, polynomial function [44], analytical model [45], and piecewise linear and exponential functions [46] are used. It is less accurate than the table-look-up scheme and needs a little bit more computational time. Use of artificial neural network (ANN) [47] for torque estimation eliminates the need of pre-measurement, and takes care of the change of parameters over time, but the iterative nature of ANN requires training before the torque profile is obtained.

As for torque control, the main aim is to reduce the torque ripple output, especially during phase commutation. It can be classified into mechanical construction and electronic control method. An example of mechanical construction is to adjust the pole arcs of the stator and rotor poles [48] so the torque ripples during phase commutation can be alleviated. Mechanically stacking of several SRM segments with appropriate phase shifts [49] is also an effective measure. This approach results in simple electronic controller that only carries out constant phase current control during the torque-producing regime. The drawback of mechanical method is the inflexibility due to need for specific design considerations at the machine design stage.

Electronic control method is to control the terminal voltages or currents so the phase torque and hence torque ripple can be controlled. An early stage example of electronic control is current profiling [48, 50 – 56]. The SRM torque-current-position characteristics are pre-measured and stored in computer memory; or modelled as analytical equations. With different phase torque commands at each rotor position, the corresponding current commands are obtained from memory. The phase currents are then controlled according to the commands. The success of the scheme depends on the measurement quality of the machine characteristics and modelling. As with most table-look-up methods, the major weakness of such scheme is the large storage requirement. In addition, current control using voltage-source power converter results in variable control process gain because of variations in the phase inductances. It needs special consideration on controller design based on machine parameters [29, 31, 57], for satisfactory dynamic performances. Self-tuning controller [58, 59], ANN [60–62], and adaptive fuzzy logic controller [63], which are based on advanced control techniques, have also claimed success in torque ripple reduction. However, these controllers have limited applications because of excessive computational power requirements and long settling time for self-tuning.

Direct instantaneous torque control, using phase torque as feedback variables, are presented in [43, 64, 65]. The torque-current-position or torque-current-flux linkage relationship is first measured offline and stored in computer memory. During on-line operation, the memory is used to estimate the torque output of each phase. With the estimated phase torques as feedback, the terminal voltages are controlled accordingly to allow the phase torques to follow the torque command. In terms of accuracy, the performance of the scheme is similar to that of current profiling. However, in terms of feedback controller design, it is more complex. Because the process gain of torque-to-current translation varies between rotor positions and is not easily predicable, the design of the controller feedback gain becomes difficult, thus simple hysteresis feedback is commonly used.

1.2.4 Motion control

Though SRM possesses advantages of low rotor inertia, high operating temperature and little maintenance requirements, which are ideal for position servo, most literatures focus on speed control [9], [66– 72]. [9, 66] present the use of a traditional proportional-integral (PI) speed regulator together with an inner current loop in cascade. [67, 68] implement nonlinear controllers instead of a simple PI regulator for speed regulation. [69] uses genetic algorithm (GA) to tune the PI controller, which produces similar outcomes as the use of nonlinear controller, but requires more on-line computational power. The use of ANN [70] eliminates the use of PI controller, but requires pre-acquired data to train the controller. As explained by [71, 72], when speed signal is calculated from the position encoder, it contains significant quantisation noise, which may require filtering and impose limits in applications that operate with speed feedback.

On top of the speed loop, a position controller can be cascaded [66, 68, 71–73] for position control. The construction of the motion controller becomes a three-loop structure, which contains position, speed and current loops in cascade. As the bandwidth of the outer loop is in general smaller than the inner one, the three-loop structure results in slow dynamic response. In addition, the tuning problem of the parameters of the controllers becomes complicated. Even if self-tuning controllers, such as auto-disturbance rejection controller (ADRC) [68] and adaptive fuzzy logic controller [73], are used, it is necessary to tune more than 10 controller parameters based on trial and error.

Position control without speed loop is demonstrated in [74, 75]. [74] uses classical proportional-integral-derivative (PID) to control the force command, which is then translated into current commands according to the magnetic characteristics for current control. As mentioned by [68], the drawbacks of PID are the amplification of noise signals due to the derivative operator, and the tuning of the controller parameters requires compromise between response time and overshoot. [75] presents a self-tuning controller for position control. It estimates the mechanical parameters of the machine online and then adjusts the controller parameters accordingly. After tuning, the servo system has fast dynamic response and is free from overshoot. The major flaw of the self-tuning regulator is the completion time of tuning. For the controller described, it takes about 8 s to finish the estimation, which is too long for dynamic applications.

1.3 Objectives and organisation of this thesis

The objectives of this thesis are to develop a computer simulation model to simulate the operation of SRM, to derive an online torque estimator, to establish an instantaneous torque controller, and to control the rotor position of the SRM. The scope and organisation of this thesis are outlined as follows:

Chapter 2 presents a computer simulation model for multiphase SRM, which combines both circuit-oriented and signal-oriented approaches using MATLAB/ SimPowerSystems. It takes the advantages of both approaches. The SRM model is connected to the power drive with electrical circuit representation, and to the controller and mechanical system with signal flow connections. The detailed magnetic characteristics of SRM, considering magnetic saturation and mutual coupling, are stored in tabular form. The power drives are simulated with circuit-oriented approach that can represent the electrical connections and topology without translation into signal flow. Simultaneously, the electronic controller and mechanical system are modelled with signal-oriented approach, which permits easy alterations to controller design and load modelling. The simulation outputs match the experimental waveforms, which confirm the validity of the simulation model. The model provides convenient means to simulate the SRM, power drive, controller, and their interactions.

An online instantaneous torque estimator for SRM under hysteresis current control is developed in Chapter 3. When the SRM is operating in hysteresis current mode, the terminal voltages, phase currents and rotor position are acquired. The flux linkages of each phase are then evaluated accordingly. A Fröhlich-like model, together with a few pre-measured magnetic parameters, is used to estimate the co-energy online, with magnetic saturation taken into consideration. The co-energy and the corresponding rotor position are stored in computer memory. In the next switching cycle, the newly estimated co-energy, stored co-energy, and rotor positions are used to calculate the instantaneous torque, based on the principles of co-energy. Computer simulation and experiment show that the estimator output is similar to that using cubic spline model, which is a commonly used model for SRM modelling.

In Chapter 4, an online instantaneous torque controller is developed. The low-current magnetic characteristics of the SRM are first measured offline. Based on the characteristics, the co-energy and phase torque output are evaluated. Hence, a co-energy profile for unit torque is calculated. As the co-energy is largely proportional to the phase torque, extending from low current to saturating regions, the co-energy profile is used to evaluate the required co-energy for the specified phase torque command. During online operation, the co-energy commands of each phase are calculated from the profile, a simple torque-sharing function, and the desired electromagnetic torque. A co-energy regulator is designed to regulate the co-energy of each phase to follow the command. Stability analysis of the control system shows that the design of controller is simple, even though the phase inductance varies significantly. A co-energy estimator based on a Fröhlich-like equation is utilised to estimate the co-energy for online feedback. The effect of magnetic saturation is considered during the estimation of co-energy. Simulation and experiment proves that the proposed scheme is effective to control the torque output of each phase, thereby reducing the overall torque ripple of the electromagnetic torque.

Chapter 5 further extends the instantaneous torque controller into four-quadrant operation. The instantaneous torque control of SRM in motoring and generating modes in both clockwise and anti-clockwise rotations are investigated. The principle of torque control is based on co-energy control, which is derived in Chapter 4. The rotor position is manipulated to fulfil the excitation sequence requirements for four-quadrant operation. For torque output in the clockwise direction, rotor position of phase 1 is used as the reference rotor position. The relative rotor positions of other phases are developed from phase 1 by adding phase shifts. As for torque output in anti-clockwise direction, the rotor position of phase 1 is mirrored along the aligned position. By subtracting phase shifts, the relative positions of other phases are derived. The scheme is intrinsically capable to operate in both generating and motoring modes, without any change in controller parameters or structure. The co-energy controller is designed with the concept of internal model control, which reduces the problem of controller parameters tuning into the selection of closed loop bandwidth or settling time. Also, the torque-speed limits of SRM are analysed in details, in terms of the basic machine parameters. Computer simulation and laboratory results verify the stability of the scheme. In contrast to traditional constant current control method, the proposed system demonstrates improvement in torque ripple reduction, for motoring and generating modes.

In Chapter 6, a rotor position controller is built on top of the four-quadrant torque controller developed in Chapter 5. With the torque controller based on co-energy control as the inner loop, a position controller is designed to control the rotor position of an SRM. The concept of torque control is similar to that proposed in Chapters 4 and 5, but the co-energy estimator is improved with an advanced magnetic model, which is more suitable to low-speed and static applications. Both the co-energy and position controllers are designed with the principles of two-degree of freedom internal model control. As the controllers can effectively reject disturbance within a short time, they require no feedforward control, which needs excessive plant information. It also has the beauty of internal model control, as the only custom parameters required are the settling times. In addition, the proposed position controller eliminates the use of speed loop, and hence the number of control loops is reduced from three to two. The structure of the control system and dynamic response are thus enhanced, in comparison with traditional three-loop structure. Computer simulation and experiment are presented to show the system is operating as designed. Robustness of the system against variation of the modelled process plant is also confirmed.

Chapter 7 summarises the contributions of this thesis. The contributions include the development of a computer simulation model, online instantaneous torque estimator, instantaneous torque controller and rotor position controller. It also describes possible future research and development works on SRM.

2 Development of Computer Simulation Model of Switched Reluctance Motor

2.1 Introduction

Magnetic saturation and double salient structure are the two main characteristics of SRM. They result in non-linear and non-sinusoidal relationships among phase current, flux linkage, output torque and rotor angle. When compared with DC motors, these nonlinearities introduce complexities in the modelling, simulation and control of SRM. As pointed out in Chapter 1, most researchers utilise either circuit-oriented or signal-oriented approach to simulate the behaviours of SRM. Both approaches have their pros and cons, and if the merits of the two approaches are combined intelligently, they can be complementary to each other.

The objective of this chapter is to establish an SRM model based on a combination of circuit-oriented and signal-oriented approaches using MATLAB/ SimPowerSystems. With such approach, the power drive of SRM is modelled with circuit-oriented approach, whereas the electrical and mechanical systems as well as the control algorithm are simulated with signal-oriented approach. This arrangement inherits the advantages of both approaches because it offers flexibility when studying different circuit configurations, while at the same time allows easy modification of the control algorithm. No manual conversion of electronic circuit into signal flow is required.

The model considers the effects of both self-coupling and mutual-coupling on flux linkage and torque production. The self-inductance and mutual-inductance are obtained experimentally. The torques are then calculated from the inductances based on the concept of co-energy. The data are stored as look-up table for subsequent simulation. Cubic splines are used to interpolate the values between data points. The simulated currents are compared with the measured waveforms to verify the proposed simulation model.

2.2 Characteristic of SRM

2.2.1 Flux linkage expression

When a voltage is applied across the motor winding, the flux equation neglecting the mutual inductance can be written as:

$$\lambda_{jj} = \int \left(v_j - i_j R \right) dt \tag{2.1}$$

where λ_{jj} represents the flux linkage of phase j, which is a function of the phase current and rotor angle, v_j represents the applied phase voltage, i_j represents the phase current, and R is the winding resistance.

Considering the mutual coupling between phases, the flux equation becomes:

$$\lambda_{jj} = \int \left(v_j - i_j R \right) dt - \sum_{\substack{k=1 \\ k \neq j}}^{m} p_{jk} \lambda_{jk} \tag{2.2}$$

where λ_{jj} represents the self-flux linkage, λ_{jk} represents the mutual flux linkage of phase j due to the current in phase k, m represents the number of phases, p_{jk} is a coupling coefficient to account for the effect of magnetic polarities as mentioned in

[20, 28]. p_{jk} is either 1 or -1, depending on the directions of the phase currents, winding configuration and rotor position.

The self-flux linkage of equations (2.1) and (2.2), and the rotor position can be used to find the phase current. As the relationships among flux, rotor position and current are non-linear and machine-dependent, the phase current is obtained from a look-up table, which is derived either experimentally or from finite element method. In this chapter, the data acquired from experiment, as given in Appendix 8.1, are used.

2.2.2 Torque production

The torque production of each phase is usually described in terms of its co-energy W_{jj}. Neglecting mutual inductance, co-energy is the integral of flux linkage with respect to current:

$$W_{jj} = \int_0^{i_j} \lambda_{jj} di_j \tag{2.3}$$

The phase torque T_j is the partial derivative of the co-energy with respect to the rotor angle θ:

$$T_j = \frac{\partial W_{jj}}{\partial \theta} \tag{2.4}$$

The instantaneous electrical torque output T_e is the sum of the phase torques:

$$T_e = \sum_{j=1}^{m} T_j \tag{2.5}$$

To include the effect of mutual inductance, the co-energy W_{jk} due to mutual coupling is considered:

$$W_{jk} = \int_0^{i_j} p_{jk} \lambda_{jk} di_j \tag{2.6}$$

The influences of current i_j on magnetic saturation and hence on flux linkage λ_{jk} are assumed to be negligible in the calculation. As the currents i_j and i_k are generally small when both phases conduct simultaneously, in contrast to their peak values, the above assumption is generally valid.

The torque arisen from mutual coupling is:

$$T_{jk} = \frac{\partial W_{jk}}{\partial \theta} \tag{2.7}$$

The instantaneous electrical torque becomes:

$$T_e = \sum_{j=1}^{m} T_j + \sum_{j=1}^{m} \sum_{k<j}^{m} T_{jk} \tag{2.8}$$

For the torque component arising from mutual coupling, only the effect of phase $k<j$ is considered because the torque developed by two simultaneously excited phases needs to be calculated once only.

2.2.3 Mechanical system

The mechanical system of the SRM is described by the following equations:

$$\omega = \int \frac{1}{J}\left(T - T_{Load} - B\omega\right) dt + \omega_0 \tag{2.9}$$

$$\theta = \int \omega \, dt + \theta_0 \tag{2.10}$$

where J is the moment of inertia, T_{Load} is the load torque, B is the friction coefficient, ω_o is the initial velocity, and θ_o is the initial rotor position.

2.3 Simulation model

The simulation model of an 8/6 SRM system, of which the power drive and motor data are illustrated in Fig. 2.1 and Table 2.1, respectively, consists of three modules as shown in Fig. 2.2. The controller outputs the gate drive signals according to the rotor position and phase currents. The power drive then switches the power electronic devices accordingly. The devices are connected to the SRM via electrical connections. The SRM module models the electrical and mechanical characteristics of the SRM.

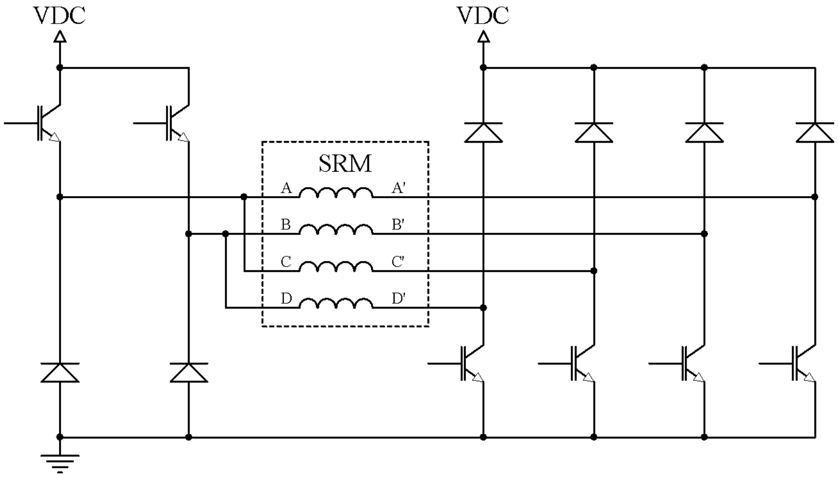

Fig. 2.1 Power drive of the SRM system

Table 2.1 Motor data

Motor rated voltage	260 VDC
Motor rated power	3 kW
Motor rated speed	50-2000 RPM
Number of stator poles	8
Number of rotor poles	6
Winding resistance	0.687 Ω

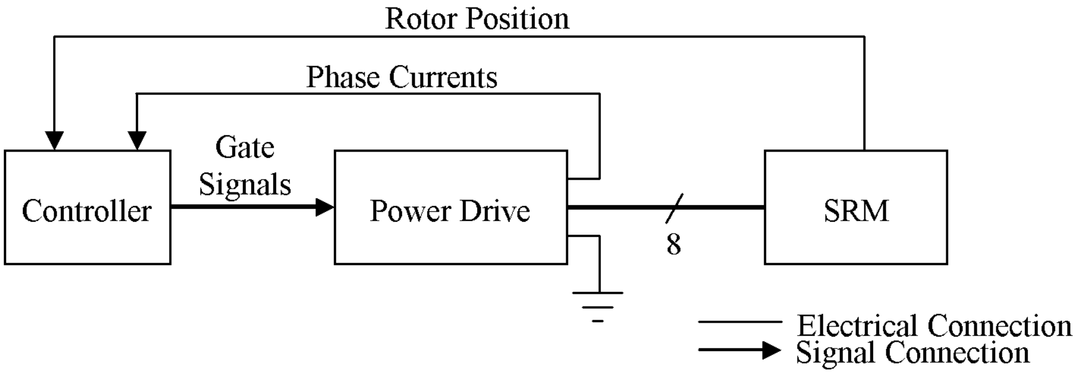

Fig. 2.2 MATLAB/SimPowerSystems implementation of the simulation model

2.3.1 SRM

The SRM module simulates the electrical and mechanical behaviours of the SRM. Fig. 2.3 shows the details of the module.

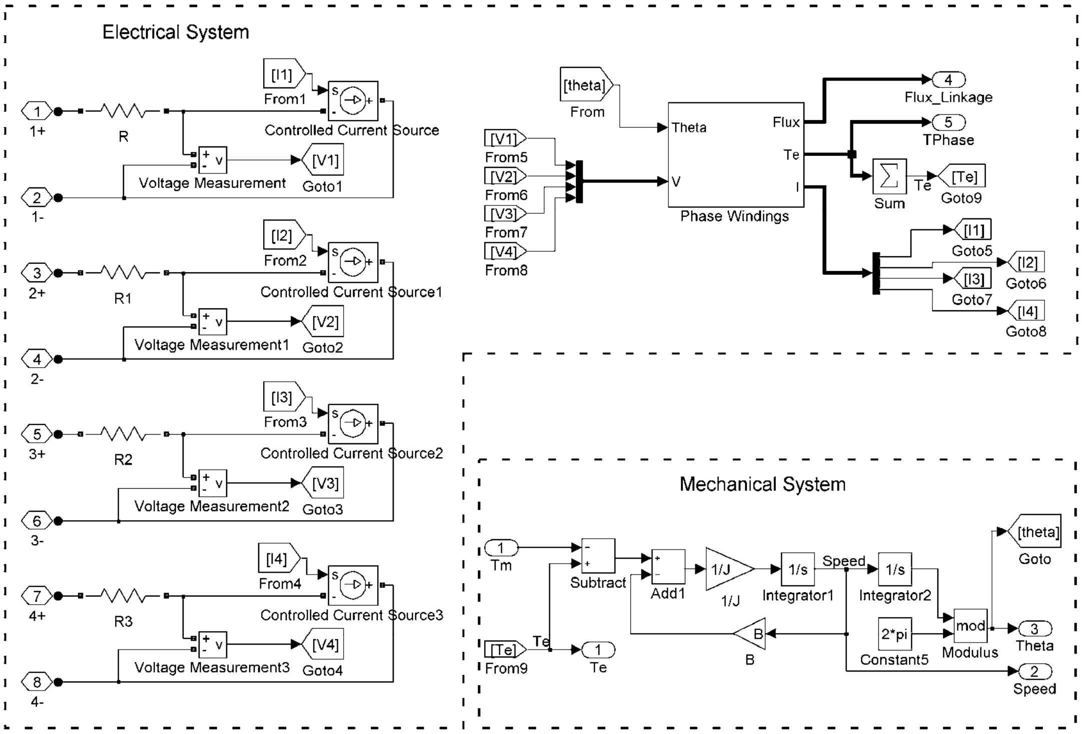

Fig. 2.3 SRM module

Each phase is simulated by a fixed resistor and a controlled current source. They model the corresponding phase resistance and the variable inductance of the winding, respectively. The rotor angle is calculated from the mechanical expression (2.10), and the measured voltages, V_1-V_4, which are equal to the phase voltage less the resistor voltage drop. The mutual flux linkages are first obtained from the currents and rotor position using a look-up table. Then, the self-flux linkages are obtained according to (2.2). The self-fluxes and the rotor angle are then used in conjunction with a look-up current table and cubic spline interpolation in order to estimate the corresponding phase current. The flux and the rotor angle are then used to calculate output torque in the Phase Windings block (Fig. 2.4). The controlled current sources are governed by the current signals inside the SRM module.

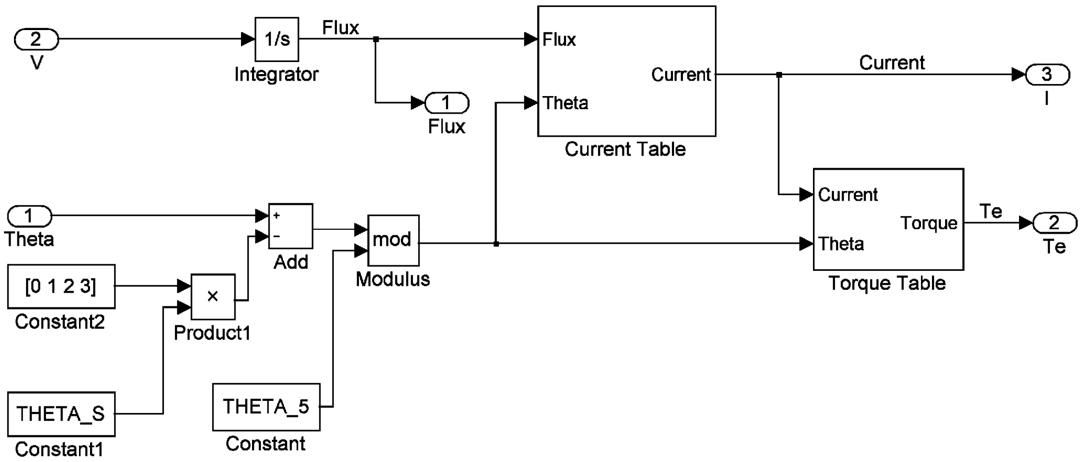

Fig. 2.4 Phase windings block

As for torque production, two look-up tables are prepared during the initialisation of the simulation according to (2.3), (2.4), (2.6), and (2.7). Phase currents and rotor angle are the inputs of the look-up tables, while the outputs are the phase torques. The phase torques are summed together to give the instantaneous electrical torque as stated in (2.8). The rotor angle and velocity are obtained in the mechanical system as described by (2.9) and (2.10).

2.3.2 Power drive

The power drive (Fig. 2.5) contains a number of switching devices to control the power flow process. Most of the connections are electrical connections, hence different power electronic converter topologies can be evaluated easily. The connections are modelled according to the physical connections of the converter without any manual translation. In this chapter, the asymmetric half-bridge of the 1.5q switches configuration [9], also known as the 2(n+1)-switch circuit [1], is used. While each phase has a switch for commutation, a switch is used for every pair of remote phases. Models of insulated gate bipolar transistors (IGBTs) and diodes are taken directly from the library of MATLAB/SimPowerSystems, and the snubbers are built from a combination of diode, resistor and capacitor. The models of the IGBT and diode, as provided by the library, include a detailed consideration of parameters, such as forward voltage, internal inductance and tail current, which are necessary to describe the behaviours of the devices accurately. In this application, the data of IRG4PC50UD and MUR1650 are used as the parameters of the IGBT and diode models, respectively.

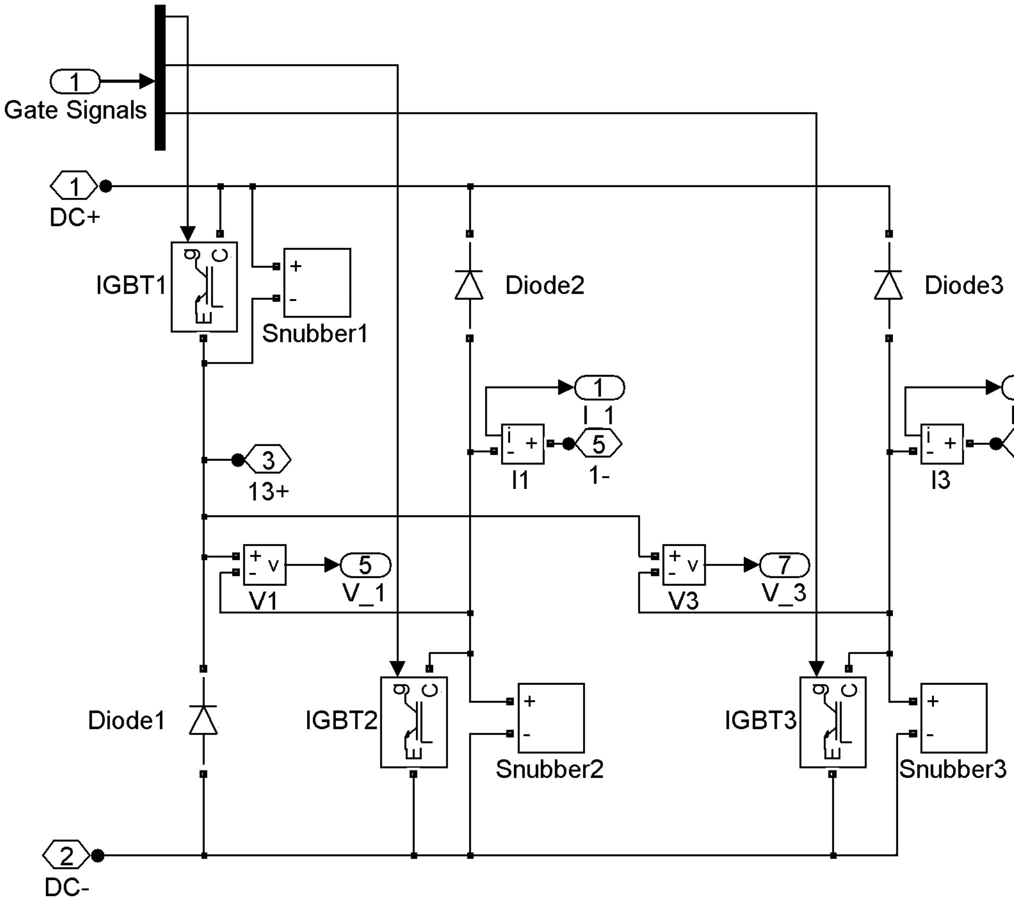

Fig. 2.5 Power drive module (only phase 1 and phase 3 are shown in details)

2.3.3 Controller

The controller is synthesised with the graphical entry environment under MATLAB/Simulink. Three common control strategies are attempted. For low speed operation, soft chopping or hard chopping hysteresis current regulator is employed. For high speed operation, single voltage pulse is used.

At low speed, the phase current is regulated within a hysteresis band. When the phase current is lower than the lower limit of the band and the rotor angle has reached the turn-on angle, the phase winding is excited to increase the current. When the phase current is larger than the upper limit, the phase winding is either freewheeled for soft chopping or excited in reverse polarity for hard chopping. Therefore, the phase current is confined within a band. Once the turn-off angle is reached, the winding is reversely excited via the diodes and the current is quenched quickly. The choice between soft chopping and hard chopping is dependent on the application. Soft chopping is employed when a lower switching frequency and smaller current ripple in DC-link are preferred.

At high speed, the phase current is not regulated. The winding is excited by the supply voltage during the on period, and is reversely excited during the off period.

2.4 Experimental verification

Simulation results of the proposed simulation model are compared with current waveforms measured experimentally. The experimental setup [76] utilises a dSpace 1102 controller board connected to an analogue hysteresis controller and a power drive module as shown schematically in Fig. 2.5. Fig. 2.6 shows the simulation and experiment waveforms under hard chopping hysteresis current control, in which the SRM operates in low speed and low current. The experimental phase current is measured with current probe.

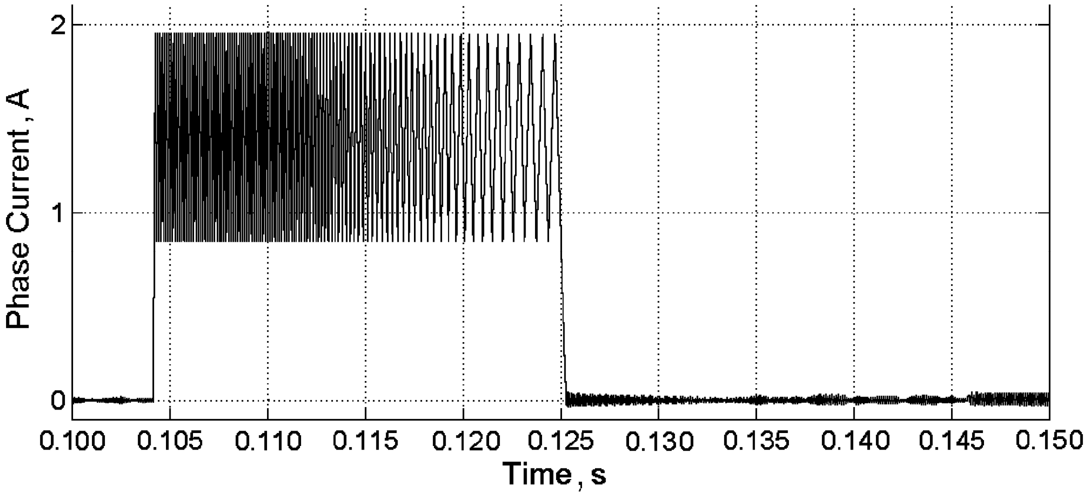

(a)

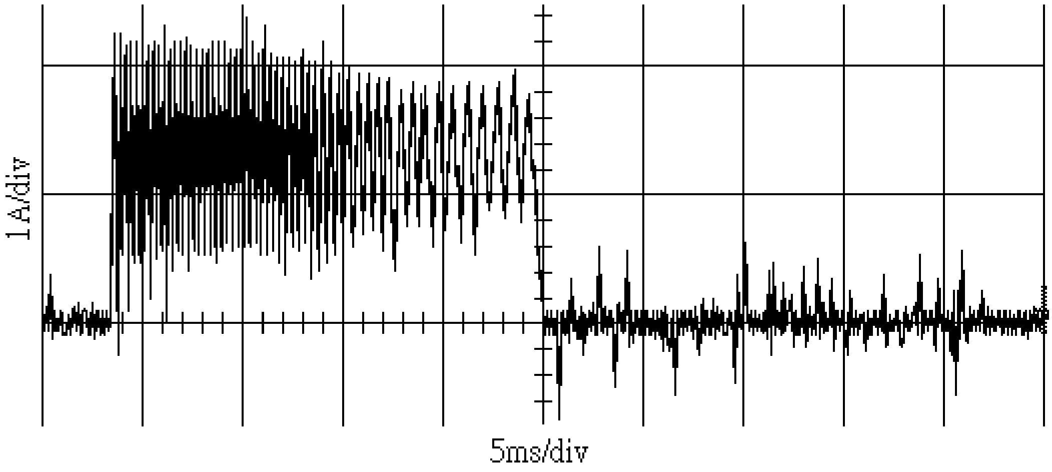

(b)

Fig. 2.6 Phase current waveforms (turn on at 0°, turn off at 15°, supply voltage = 122 VDC, current setpoint = 1.4 A, hysteresis band = 1.1 A, speed = 120 RPM). (a) simulated waveform; (b) measured waveform

The difference between Fig. 2.6(a) and Fig. 2.6(b) is because the controller of the simulation is assumed to have no delay while that of the experimental setup contains signal delay. The delay allows the phase current to go beyond the hysteresis band before changing the switching state, especially when the inductance is small and the current changes rapidly. As a result, the experimental result shows a larger hysteresis band. In addition, the current probe picks up the electromagnetic noise due to the switching of the power drive during experimentation, and results in spiky waveform. It should be noted that, although the simulation model considers the current fall time and tail current, their effects are not noticeable in Fig. 2.6(a). It is because the fall time and tail time, which are of the order of 100 ns, are small in the time scale.

As for high speed and large current situation [19, 76], the current waveforms are shown in Fig. 2.7. The simulated electrical torque waveform is plotted in Fig. 2.8. The torque waveform is affected by the mutual coupling among the windings. The peak torque output, when both phases 1 and 4 are conducting, is 8% lower than that produced by other phases. It is because of the mutual coupling in the motor which has the winding type of “NSNSSNSN”.

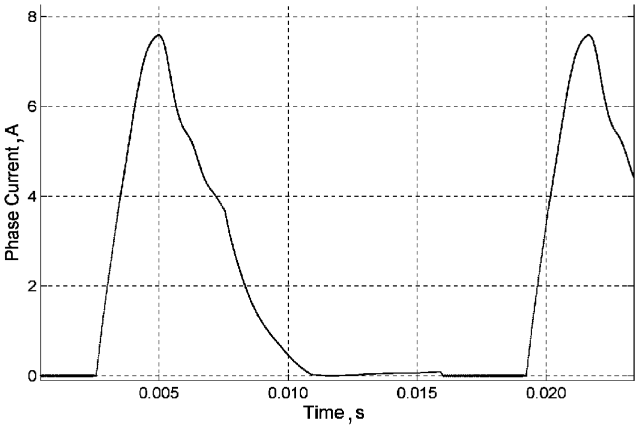

(a)

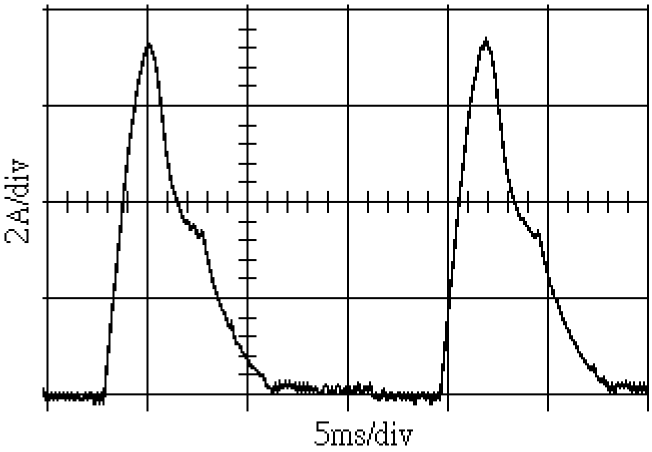

(b)

Fig. 2.7 Phase current waveforms (turn on at -3°, turn off at 15°, supply voltage = 33.4 VDC, speed = 600 RPM). (a) simulated waveform; (b) measured waveform

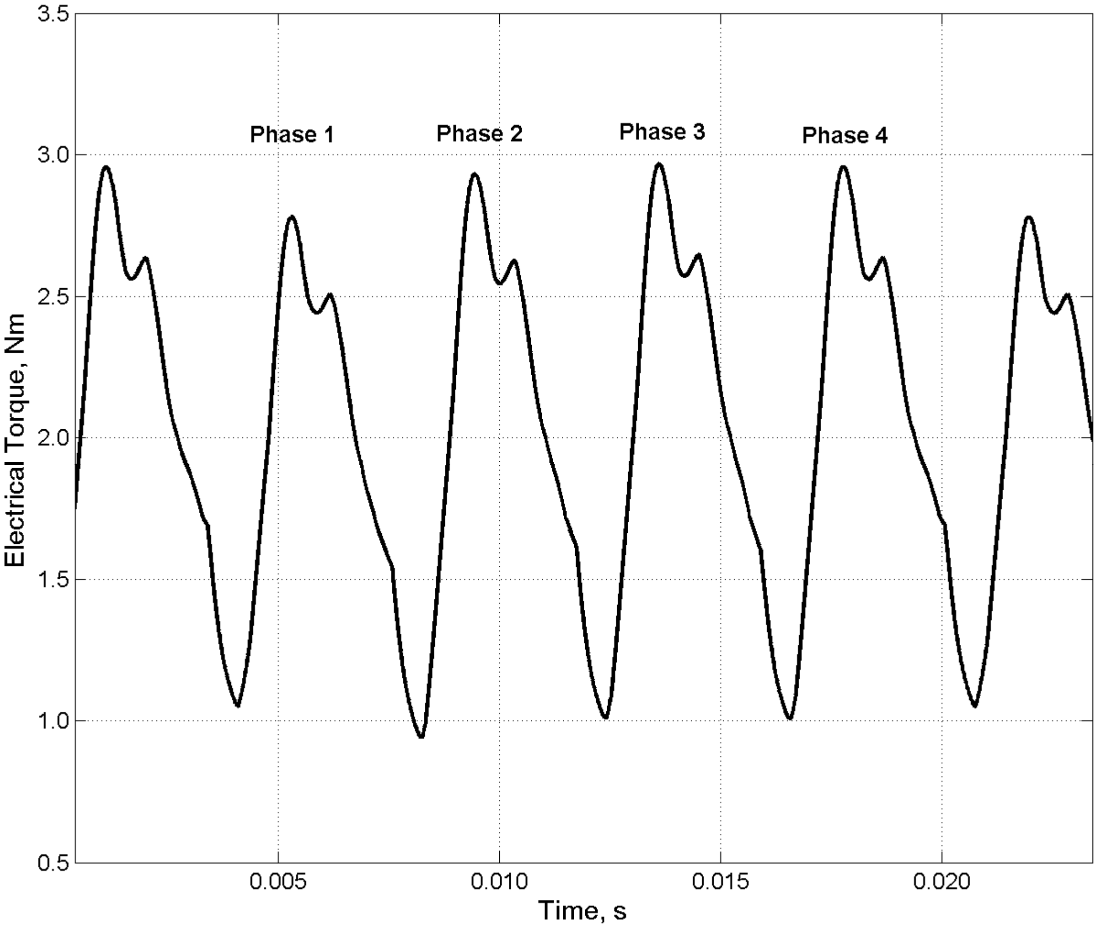

Fig. 2.8 Simulated electrical torque waveform (turn on at -3°, turn off at 15°, supply voltage = 33.4 VDC, speed = 600 RPM)

As consecutive windings of phase 1 and phase 4 are of the same magnetic polarity, current of phase 4 tends to reduce the flux linkage on phase 1 when both phases are conducting and vice versa. Hence, the mutual flux linkage tends to reduce the electrical torque during the overlapping excitation period of phases 1 and 4. As for the coupling between other adjacent winding pairs, the polarities of consecutive windings are opposite. Therefore, the flux linkages and torque outputs of neighbourhood windings are increased. In general, the influence of mutual coupling is dependent on the winding arrangement, turn-on and turn-off angles, and current waveform.

The experimental torque waveforms are not presented in this section, because the bandwidth of the torque transducer system, which is 200 Hz, is insufficient to reconstruct the detailed waveforms the torque ripples. In addition, the misalignment of the mechanical couplings may introduce low-frequency torque ripple and distort the results.

Although the measurement of mutually induced voltages of non-active phases can reveal the effect of mutual flux linkage, they are not measured during the experiment because the induced voltage is generally very small and contains a lot of noise, due to, for example, leakage current and stray capacitance in the associated power electronic devices.

The electrical torque output contains a rich amount of ripples because of the absence of current regulation during high-speed operation. As the phase current is not controlled and the on-off angles are not optimised, the instantaneous torque rises and falls with the current in the active phase. It can be seen that the troughs of the instantaneous torque are appearing during the phase commutation periods, while the peaks are the results of the current peaks.

2.5 Summary

This chapter presents an SRM system simulation model that combines both circuit-oriented and signal-oriented approaches. The essential components of the SRM drive system, including controller, power drive, SRM and load, are included in the model. The source data of the model are obtained from experiments. Good comparison of measured and simulated results validates the accuracy of the simulation model under different operating conditions.

In the proposed simulation algorithm, it is found that the mutual coupling between phases is having a significant impact upon the production of torque in SRM. However, the mutual coupling is dependent on the conduction angle, winding arrangements, and current waveforms. Hence the designer must consider the mutual coupling among the windings in the early conceptual stage if an optimal controller of SRM is to be designed.

In summary, the proposed simulation model is useful for the computer-aided design of SRM power drive and control algorithms. As the connections of the power drive model are the same as the physical wirings, there is no need to manually translate the power drive circuits into signal flows for the simulation. Therefore, the testing of new circuit topology and evaluation of component rating becomes convenient.

3 Online Torque Estimator of Switched Reluctance Motor

3.1 Introduction

Online torque estimator is essential for instantaneous torque control, torque ripple reduction and motion control of SRM. Because of the magnetic nonlinearities among torque, phase current and position, torque estimation of SRM is difficult. As depicted in Chapter 1, most instantaneous torque estimation algorithms require extensive pre-measurement or computational time, which are not desirable for real-time applications. Thus, the development of an instantaneous torque estimator, which requires only limited pre-measured data and mathematical manipulation, is necessary and challenging for researchers.

This chapter proposes an online torque estimator for SRM operating under hysteresis current control using conventional asymmetrical half-bridge topology. The estimator only requires the pre-measurement of a limited amount of data including the inductance profile at low current, saturating phase current, real-time on/off status of the power electronic switches, DC-link voltage, phase currents and rotor position. Results obtained from the estimator agree well with those obtained experimentally.

3.2 Proposed torque estimator algorithm

Fig. 3.1 illustrates the structure of the torque estimator. It estimates the flux linkage of each phase based on the status of power electronic switches, DC-link voltage and phase current. Subsequently, the flux linkage and the corresponding phase currents are utilised to calculate the co-energy. The computed co-energy, together with the respective measured phase current and rotor position, are stored in a look-up table. The output torque of the SRM is estimated based on the differences between new values and those obtained from the previous switching cycle at the same current, of both co-energies and rotor positions. With this approach, very small amount of data are processed and hence the torque can be estimated quickly on-line.

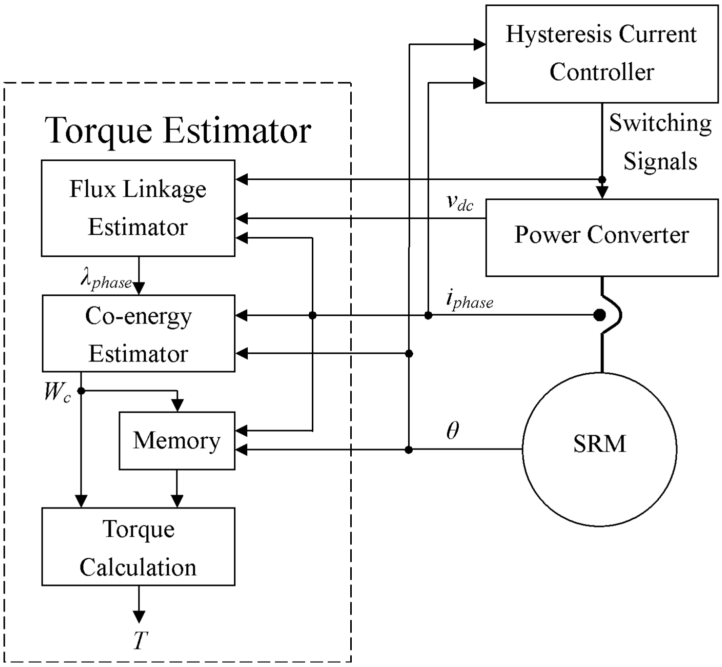

Fig. 3.1 Structure of the torque estimator and SRM drive

3.2.1 Estimation of flux linkage

The estimated flux linkage of each phase λ_{phase} is calculated as:

$$\lambda_{phase} = \int \left(v_{phase} - i_{phase} R \right) dt \tag{3.1}$$

$$v_{phase} = \begin{cases} v_{dc} - 2V_T & \text{for magnetising} \\ -V_T - V_D & \text{for freewheeling} \\ -v_{dc} - 2V_D & \text{for demagnetising} \end{cases} \tag{3.2}$$

where, v_{phase} is the phase voltage which is dependent on the on/off states of the switches, i_{phase} is the phase current, R is the winding resistance, v_{dc} is the DC-link voltage, V_T is the on-state voltage drop of the IGBT, and V_D is the forward voltage drop of the diode. The effects of switching transients of the IGBTs and power diodes, which are mainly the current rise time, tail current and reverse recovery, are neglected, as they last for about 100 ns, while the sampling frequency of the controller is less than 10 kHz. The flux linkage is reset to zero when the phase current is fully quenched in order to eliminate the accumulation of measurement errors and to avoid drifting due to numerical errors. It should be noted that the winding resistance which changes with temperature can be accurately estimated online [41, 77, 78]. However, for simplicity, winding resistance estimator is not implemented in this chapter.

3.2.2 Estimation of co-energy

The co-energy W_c of each phase is estimated based on the integral of the flux linkage:

$$W_c = \int_0^{i_{phase}} \lambda \, di \tag{3.3}$$

When the phase current is smaller than the saturating current i_s, the flux linkage-current relationship is assumed linear and the co-energy is calculated as:

$$W_c = \frac{1}{2} \lambda_{phase} i_{phase} \tag{3.4}$$

For phase current which is higher than the saturating current, the flux-linkage current curve is divided into two portions as illustrated in Fig. 3.2.

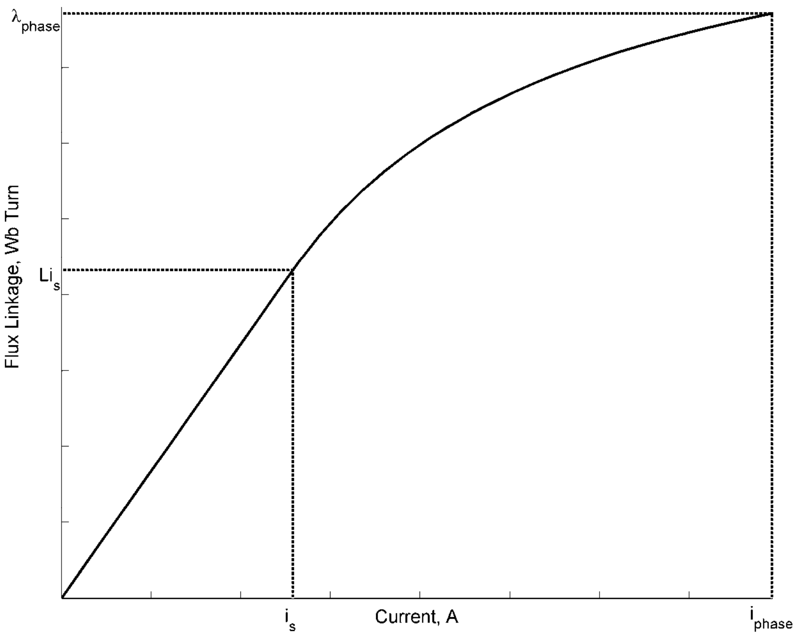

Fig. 3.2 Modelled flux-linkage current characteristics, showing key points

The part of the current that is lower than the onset of saturation is assumed linear and is described using the pre-measured low-current inductance profile *L* as follows:

$$\lambda = Li \text{ for } i \leq i_s \tag{3.5}$$

As for the portion of current that is higher than the saturating current, a Fröhlich-like equation (3.6) is used to describe the flux linkage-current curve.

$$\lambda = Li_s + a\frac{i - i_s}{b + i - i_s} \text{ for } i_s < i \leq i_{phase} \tag{3.6}$$

where *a* and *b* are coefficients to be determined online. The first order derivative of (3.6) is:

$$\frac{\partial \lambda}{\partial i} = \frac{ab}{\left(b + i - i_s\right)^2} \tag{3.7}$$

To ensure the continuity of the slope, the derivative (3.7) is set to the premeasured inductance at the saturating current:

$$\left.\frac{\partial \lambda}{\partial i}\right|_{i=i_s} = \left.\frac{ab}{\left(b + i - i_s\right)^2}\right|_{i=i_s} = L \tag{3.8}$$

After solving the equation,

$$b = \frac{a}{L} \tag{3.9}$$

The measured phase current, estimated flux linkage and (3.9) are substituted into (3.6),

$$\lambda_{phase} = Li_s + \frac{aL\left(i_{phase} - i_s\right)}{a + L\left(i_{phase} - i_s\right)} \tag{3.10}$$

a is then expressed as:

$$a = \frac{L\left(\lambda_{phase} - Li_s\right)\left(i_{phase} - i_s\right)}{L\left(i_{phase} - i_s\right) - \left(\lambda_{phase} - Li_s\right)} \tag{3.11}$$

Hence, the coefficients of the Fröhlich-like equation are determined from the inductance, flux linkage, phase current and saturating current, according to (3.9) and (3.11).

The co-energy is obtained by evaluating the integral of (3.3), with the flux linkage as described by (3.5) and (3.6) as:

$$W_c = \left(a + Li_s\right)\left(i_{phase} - i_s\right) - ab\ln\left(\frac{b + i_{phase} - i_s}{b}\right) + \frac{1}{2}Li_s^2 \tag{3.12}$$

For online estimation of the co-energy, only (3.9), (3.11) and (3.12) are evaluated.

3.2.3 Calculation of electrical torque output

The co-energy for computing the instantaneous electrical torque of each phase of the SRM is

$$T = \left.\frac{\partial W_c}{\partial \theta}\right|_{\text{i=constant}} \tag{3.13}$$

For the torque estimator being proposed, (3.13) is converted to a finite difference form as given below:

$$T = \frac{W_c\left(\theta_{now}, i_{phase}\right) - W_c\left(\theta_{previous}, i_{phase}\right)}{\theta_{now} - \theta_{previous}} \tag{3.14}$$

where; θ_{now} is the current rotor position; $\theta_{previous}$ is the rotor position in the previous switching cycle, at which the current is equal to the phase current at the time under consideration.

The instantaneous co-energy $W_c(\theta_{now}, i_{phase})$ can be calculated according to (3.12), and the co-energy in the previous switching cycle $W_c(\theta_{previous}, i_{phase})$ can be obtained from an interpolation of the co-energy of the previous cycle in the look-up table. Because a very small amount of mathematical processing is required, the computation effort is small and hence the instantaneous torque of the SRM can be computed on-line, while the SRM is operating.

3.3 Simulation results

The torque estimator as shown in Fig. 3.1 is simulated in time-domain with MATLAB/Simulink, which is described in Chapter 2. The simulation model simulates the detailed behaviours of power electronic switching and hysteresis current control. The parameters of the power drive are as shown in Table 3.1. All the simulated runtime data from the hysteresis current controller, such as switching states, phase currents and rotor position, are fed to the torque estimator as shown in Fig. 3.1.

Table 3.1 Parameters of power drive

DC-link voltage	100 VDC
IGBT part number	IRG4PC50UD
IGBT forward voltage V_T	1.65 V
Power diode part number	MUR1650CT
Power diode forward voltage V_D	0.7 V

Both the hysteresis current controller and the torque estimator have a sampling rate of 4 kHz. In the experiment, the SRM runs at 200 RPM. With the unaligned position corresponding to 0°, the turn on and off angles are 5° and 20°, respectively. The hysteresis current controller operates with soft chopping, with a control set point of 4 A and a hysteresis band of 0.5 A. The settings of the current controller can be found in Table 3.2. The current waveform of the simulation is given in Fig. 3.3.

Table 3.2 Settings of the hysteresis current controller

Sampling frequency of controller	4 kHz
Conduction angle	5°–20°
Upper hysteresis band	4.25 A
Lower hysteresis band	3.75 A

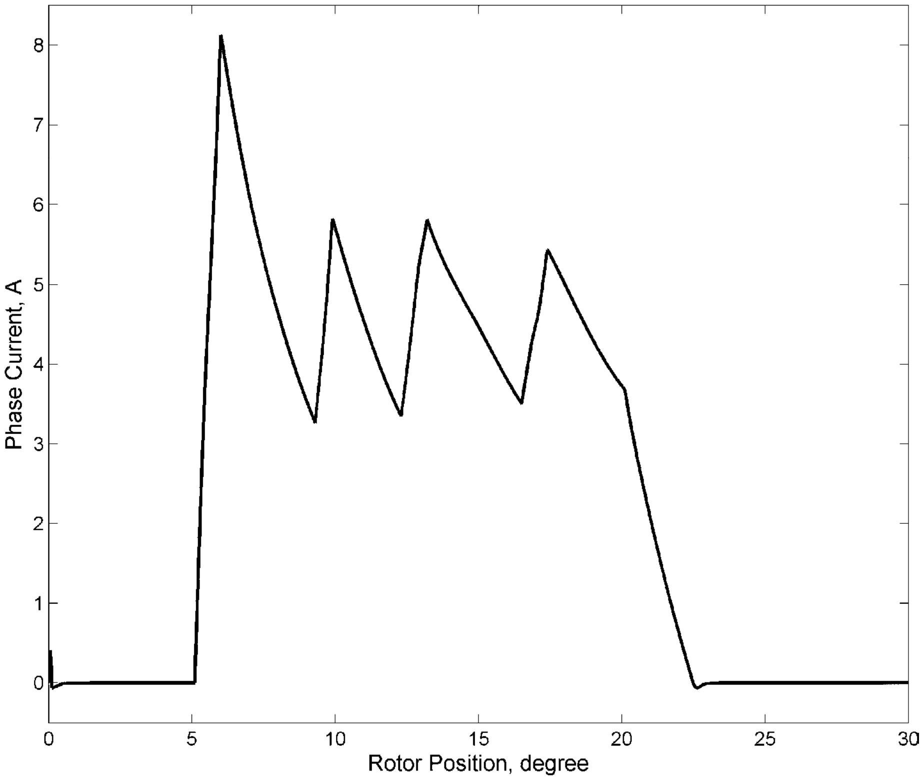

Fig. 3.3 Current waveform of phase 1 of the simulation model

The simulation result of the flux linkage estimator as obtained from (3.1) and (3.2), in contrast to the flux linkage obtained from the simulation model, is shown in

Fig. 3.4. It can be seen that the flux estimator can correctly estimate the flux linkage of the SRM while the phase is energised.

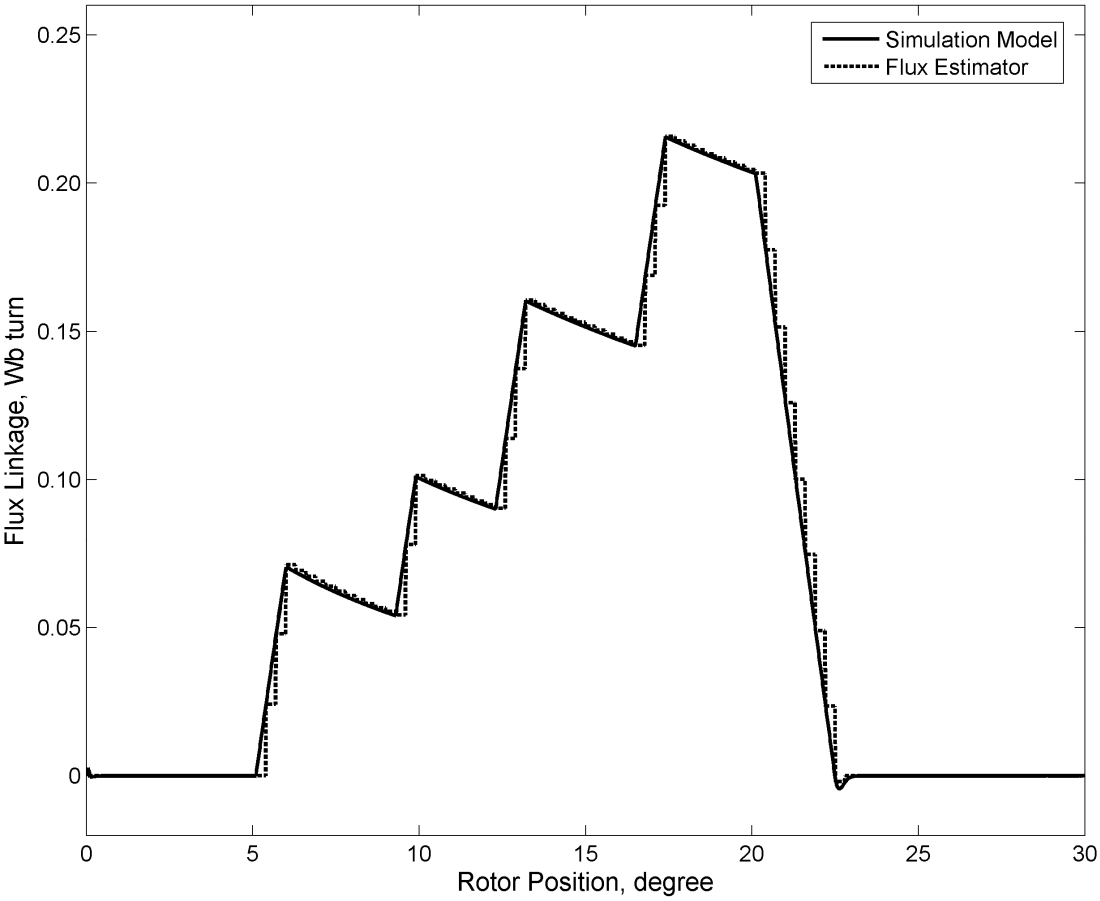

Fig. 3.4 Comparison of flux linkages of phase 1 from the simulation model and from the flux linkage estimator

The co-energy estimation derived from the co-energy estimator, and that calculated from the cubic spline interpolation using the full magnetic data are compared in Fig. 3.5. It can be seen that the estimator output is close to the results obtained from the cubic spline model.

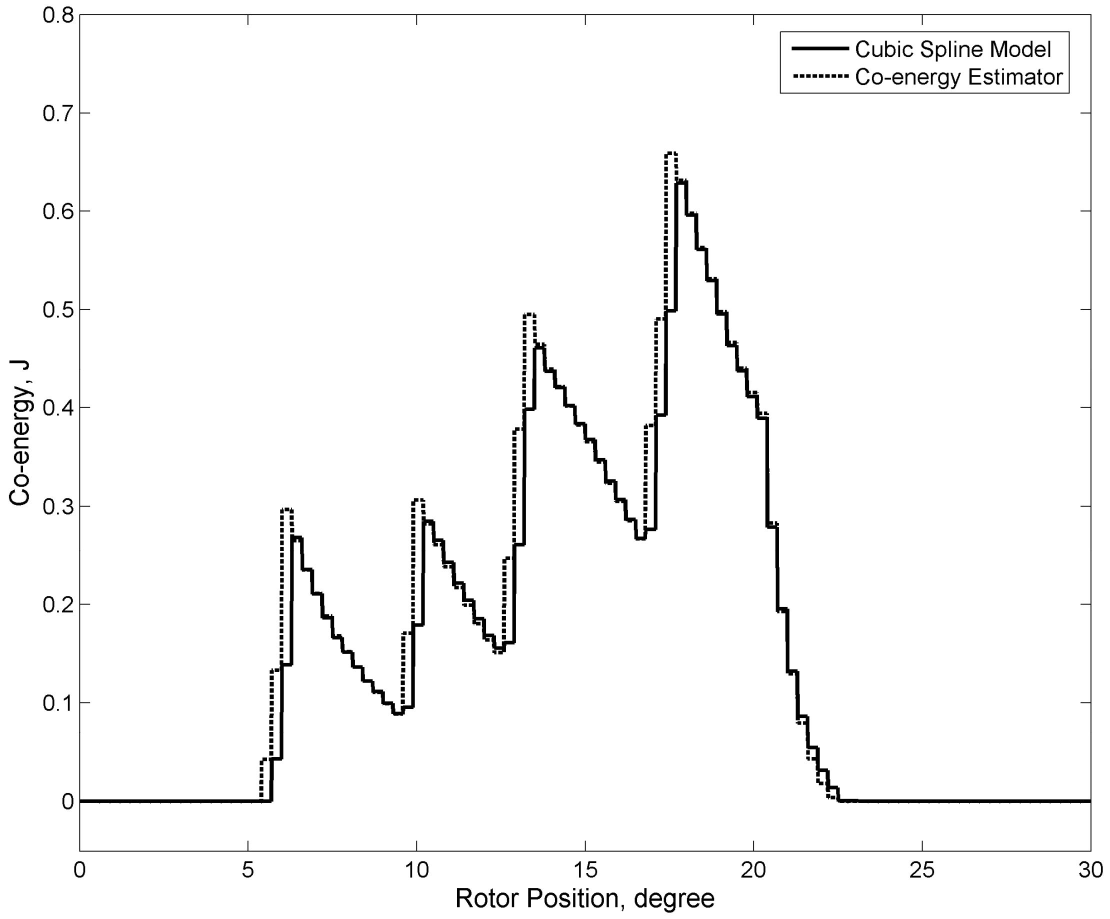

Fig. 3.5 Co-energies of phase 1 calculated by the cubic spline model and from the co-energy estimator

The torque estimator can estimate the electrical torque of the SRM, and the results from the estimator are similar to that deduced from cubic spline model as shown in Fig. 3.6. It should be noted that the torque estimator cannot estimate the torque during the first switching cycle (5° to 10°), because there are no prior data on the co-energy, current and rotor position, which are required in the calculation of (3.14).

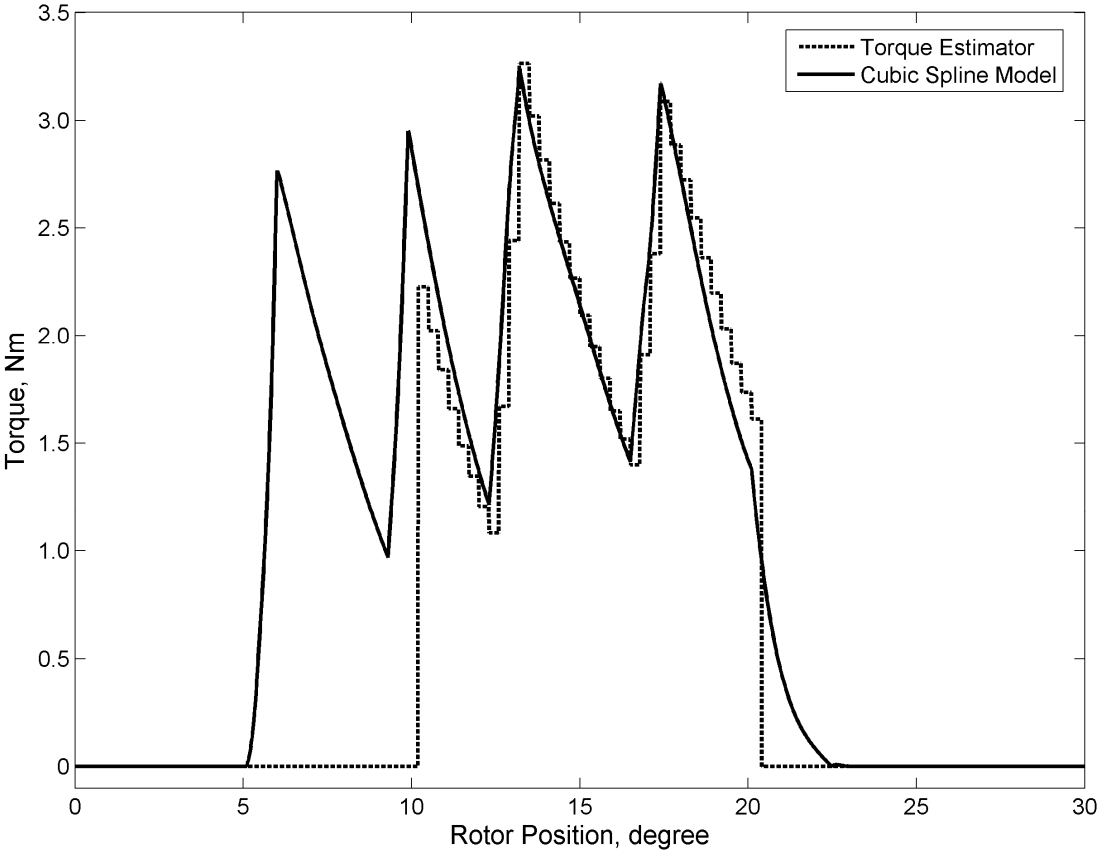

Fig. 3.6 Torque predicted by the cubic spline model and torque estimator output of phase 1

To investigate the effects of the variation of the saturation point due to change in temperature, the simulated torque estimations with the saturation point varied plus and minus 5% are plotted in Fig. 3.7. In fact, for the ferromagnetic material used in SRM, the variation of the saturation point over the operating temperature is less than 1% [79]. The figure shows that the drift of saturation point has negligible effect on the estimated torque

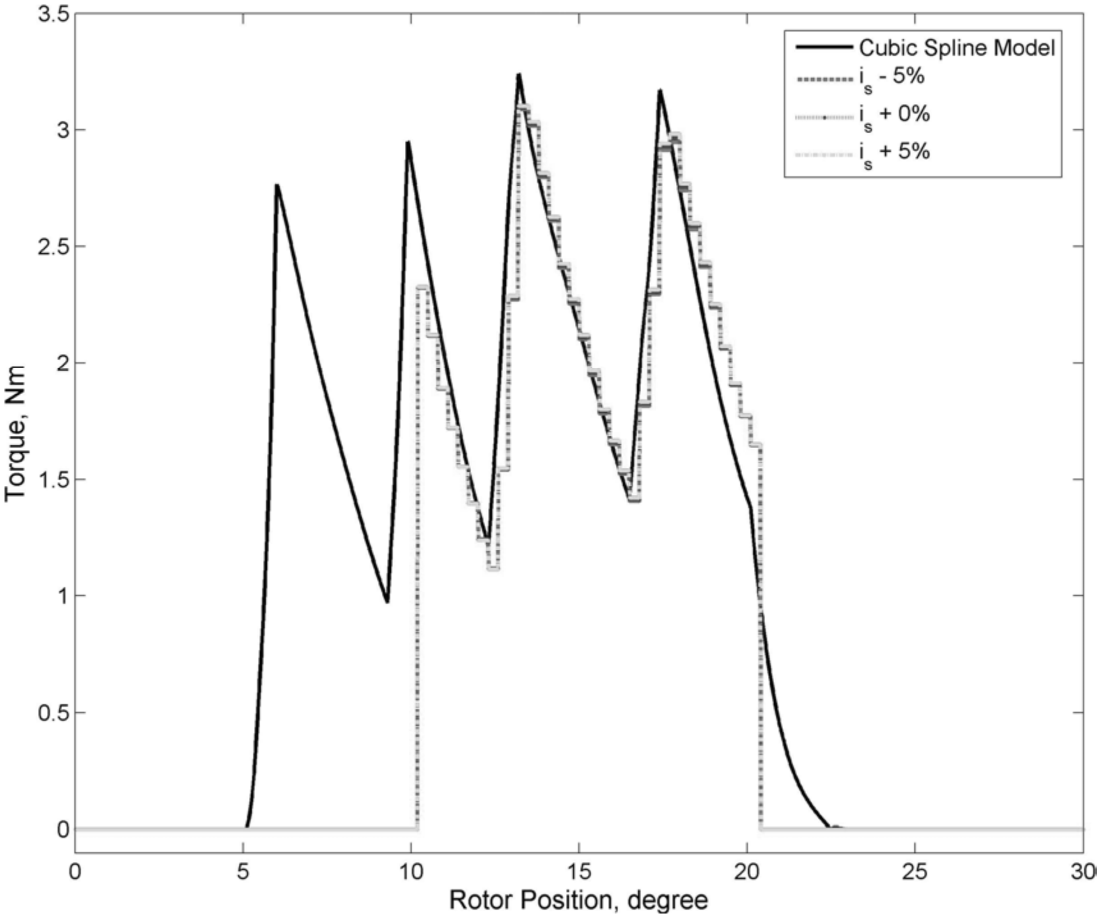

Fig. 3.7 Effects of variation of saturation point on torque estimation

Similarly, the effects of the variation of low-current inductances due to measurement error and variation of temperature are also depicted in Fig. 3.8. The inductances are varied plus and minus 5% from the nominal values. The effects of the changes of the pre-measured inductances are very small.

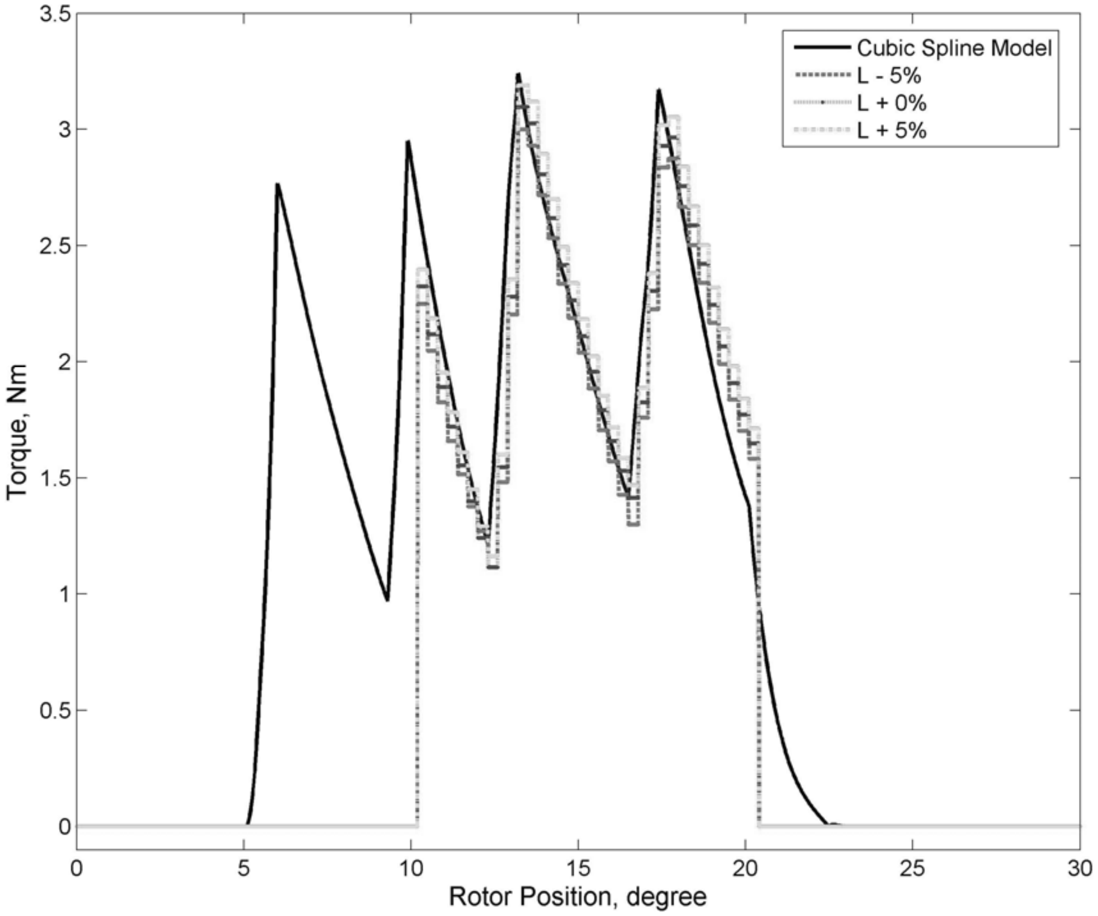

Fig. 3.8 Effects of the variation of low-current inductances on torque estimation

3.4 Experimental verification

The torque estimator and the hysteresis current controller are implemented with a dSpace 1104 R&D Controller Board running at a sampling frequency of 4 kHz. The associated sensors, signal amplifiers, and power converter are constructed with discrete electronic components. The power converter is connected to a 100 VDC supply. The motor data are the same as those used in the simulation. A dynamometer, which is built using a DC generator with a load resistance connected across the armature winding, acts as a mechanical load.

The measured current waveform, and estimated flux linkage and torque from the estimators for the SRM operating at 200 RPM are shown in Fig. 3.9 to Fig. 3.11 respectively. It can be seen that the experimental current and flux waveforms are similar to the simulated ones. As for the torque waveform, the experimental and simulated torque outputs are alike, in terms of frequency and magnitude. Both of them show that the torque ripples are significant. However, the torque estimator can still correctly estimate the torque ripple, which arises from the hysteresis current control and wide hysteresis band setting, even the SRM operates in the saturating region.

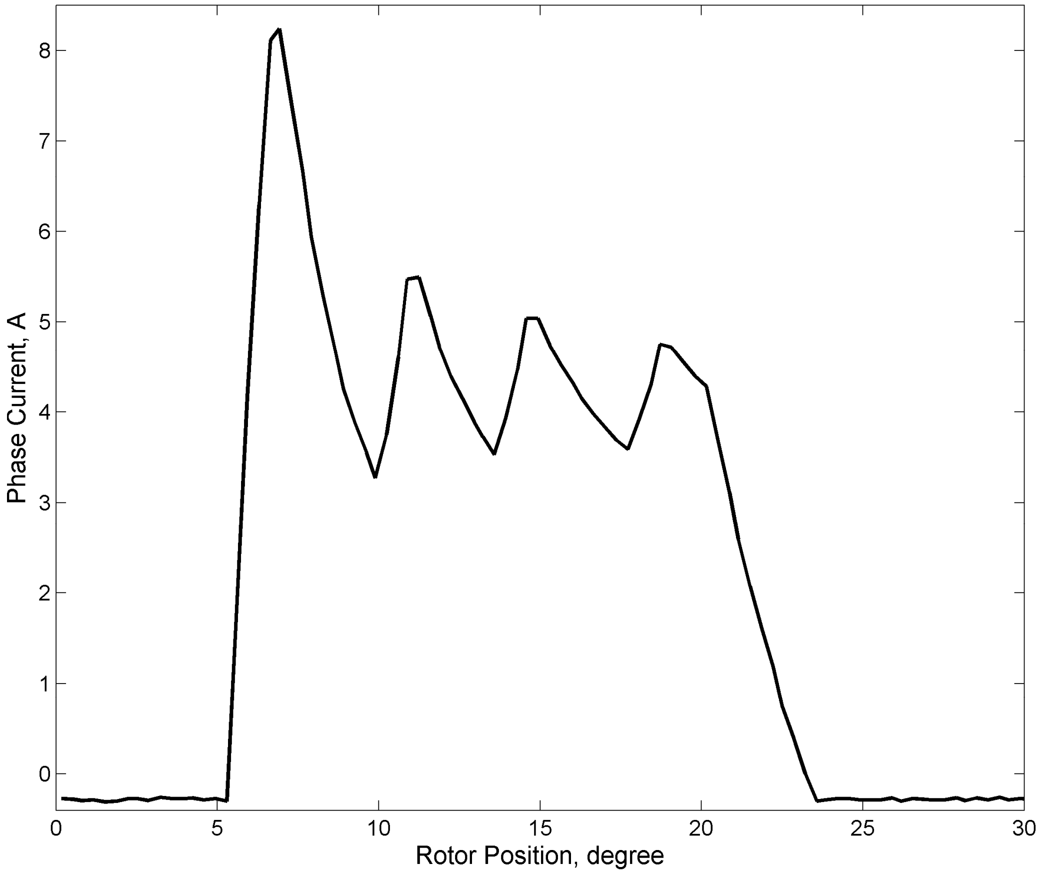

Fig. 3.9 Measured current waveform of phase 1 of the SRM operating

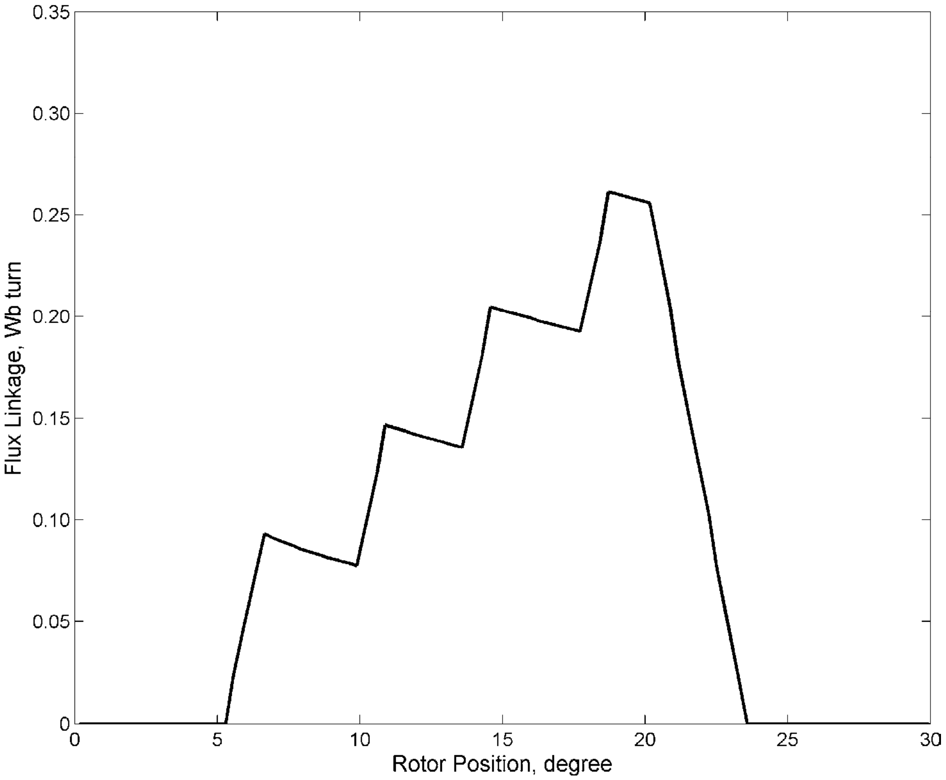

Fig. 3.10 Estimated phase 1 flux linkage from the proposed flux linkage estimator

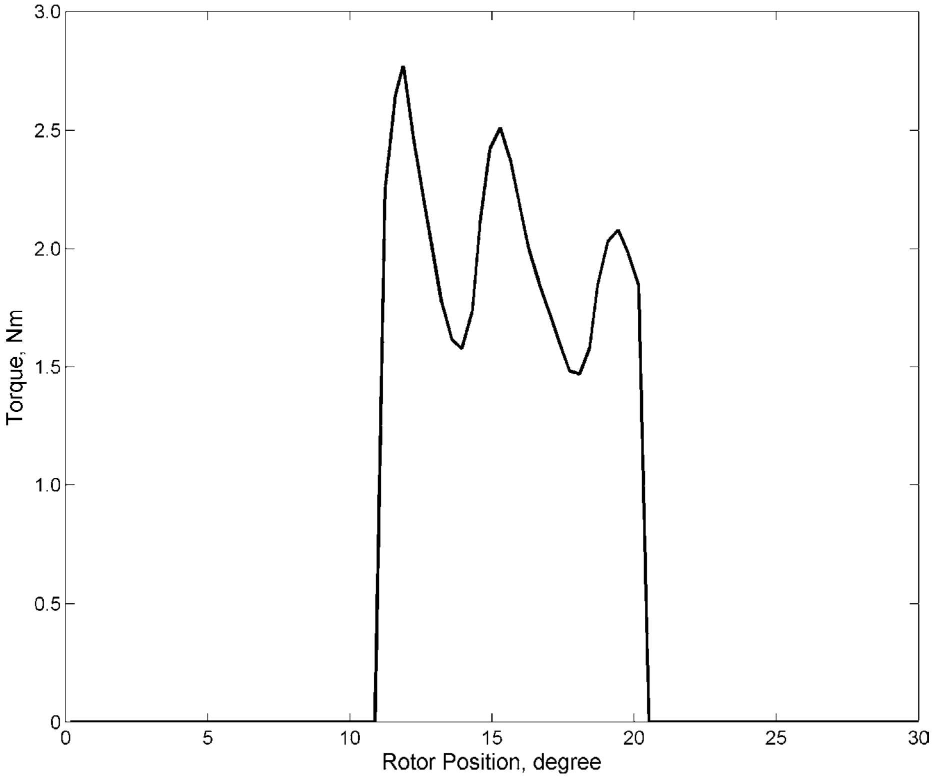

Fig. 3.11 Estimated torque of phase 1 from the proposed torque estimator

As the dynamometer being used in this investigation can only give an average torque reading, only the measured average torques are compared with the average torques computed using the torque estimator. It is found that the measured average torque using the dynamometer is 2.01 Nm, which is close to the average output of 2.07 Nm predicted by the torque estimator when the phase winding is energised. Torque transducer is not used because the bandwidth of commercially available transducers is lower than the frequency range of the shaft torque. In addition, the mechanical couplers between the dynamometer, transducer, and SRM, which are linked by rubber discs, filter out the high frequency components.

3.5 Summary

An online instantaneous torque estimator is proposed. The required offline data are the pre-measured inductance profile at low current and the saturating current. Other data are estimated at real time based on the terminal quantities. Co-energy of each phase is calculated online and stored in memory. Based on the principle of co-energy difference, the torque is estimated. The proposed algorithm requires small computational burden. Hence, it is suitable for real time applications. The torque estimator algorithm is verified using computer simulation. The electromagnetic torque outputs obtained from the estimator matches well with that of the cubic spline model. It is also implemented in a prototyping environment. Even though limited amounts of data are obtained due to hardware limitation, the measured results appear to agree with the simulation. The proposed estimator can correctly estimate the average torque of SRM, which is measured with a dynamometer, even in the absence of torque transducer. For the estimation of torque ripple, the magnitude and frequency of the torque ripple obtained with the prototype are similar to those obtained with cubic spline model. Hence, the torque estimator is effective in assessment of average torque and torque ripple.

The proposed torque estimator is expected to be of use by engineers for applications in instantaneous or average torque control for SRM under low speed operation in future development. It can also be applied to replace the expensive torque transducers for online torque ripple and average torque assessment, load monitoring, and metering.

4 Instantaneous Torque Control Based on Co-energy Control

4.1 Introduction

Control of the instantaneous torque of SRM is essential to torque ripple reduction and motion control. As discussed in Chapter 1, the nonlinearities of SRM are giving rise to difficulties in instantaneous torque control, when compared with the more established decoupled control of induction and DC machine. Most instantaneous torque control algorithms require extensive pre-measured data and result in difficult design of the feedback controller.

This chapter presents a method to control the instantaneous torque by controlling the co-energy of the machine. Under this scheme, the co-energy reference of each phase is computed from the inductance profile at low current. The co-energy is estimated using on-line motor terminal voltage, current and the low current inductance profile. It is then regulated to track the reference co-energy with a constant frequency PWM terminal voltage. The effect of magnetic saturation is considered by the co-energy estimator. The advantage of the proposed scheme is that only a small amount of machine data is pre-measured and stored.

In this chapter, the proposed feedback control system is analysed, and it can be seen that the parameters of the regulator are independent of the phase inductance. It means the regulator parameters are also independent of the rotor position and magnetic characteristics. Thus, the design of the control becomes simple. Computer simulation and experimental results are reported to validate the functionality of the control strategy.

4.2 Principles of torque control

With magnetic saturation taken into account, the torque output of each phase is described as:

$$T = \left.\frac{\partial W_c}{\partial \theta}\right|_{i_{phase} = \text{constant}} \tag{4.1}$$

As stated in [49], if the co-energy is controlled to vary linearly with the rotor position, the instantaneous torque output is constant regardless of magnetic saturation. Hence, from (4.1):

$$W_c = \left.\int_{\theta_0}^{\theta} T d\theta\right|_{i_{phase} = const} \tag{4.2}$$

where θ_0 is a constant for the initial value $W_c = 0$.

For constant torque output,

$$W_c = T(\theta - \theta_0) \tag{4.3}$$

Therefore, at each rotor position, the co-energy is directly proportional to the torque output. When the rotor position is close to the unaligned position, the constant current requirement of (4.2), however, cannot be realised because of the flux leakage at the motor poles. In other words, the relationship between co-energy and rotor position becomes nonlinear. To explain the nonlinearity mathematically, the co-energy of a non-saturated SRM is expressed as:

$$W_c = \frac{1}{2} i_{phase}^2 L(\theta) \tag{4.4}$$

The total derivative of co-energy is:

$$\begin{aligned} dW_c &= \frac{\partial W_c}{\partial \theta} d\theta + \frac{\partial W_c}{\partial i_{phase}} di_{phase} \\ &= T\ d\theta + L(\theta) i_{phase}\ di_{phase} \end{aligned} \tag{4.5}$$

Divide both sides of the equation with differential change of rotor position $d\theta$:

$$\frac{dW_c}{d\theta} = T + L(\theta) i_{phase} \frac{di_{phase}}{d\theta} \tag{4.6}$$

For constant torque output, the relationship between co-energy and rotor position is linear only if $di_{phase}/d\theta$ is zero, which explains the constant current requirement as stated in (4). In contrast, when the rotor position is close to the unaligned position, $di_{phase}/d\theta$ is non-zero for constant torque output. Hence, the co-energy and rotor position have a non-linear relationship.

To solve the problem of non-linearity between co-energy and rotor position, the co-energy profile is normalised with respect to the torque output. The magnetic characteristic at low current is measured for each rotor position first. Then, (1.2) and (1.4) are used to evaluate the co-energy and torque. A normalised co-energy profile can be obtained as

$$W_{c\,norm}(\theta)=\left.\frac{W_c(\theta,i_{phase})}{T(\theta,i_{phase})}\right|_{i_{phase}=\text{low current}} \tag{4.7}$$

The normalised co-energy profile of a 2.2 kW 270 VDC 8/6 SRM, with 0 degree set as the unaligned position, is illustrated in Fig. 4.1 as an example. The data are obtained with phase current of 1 A.

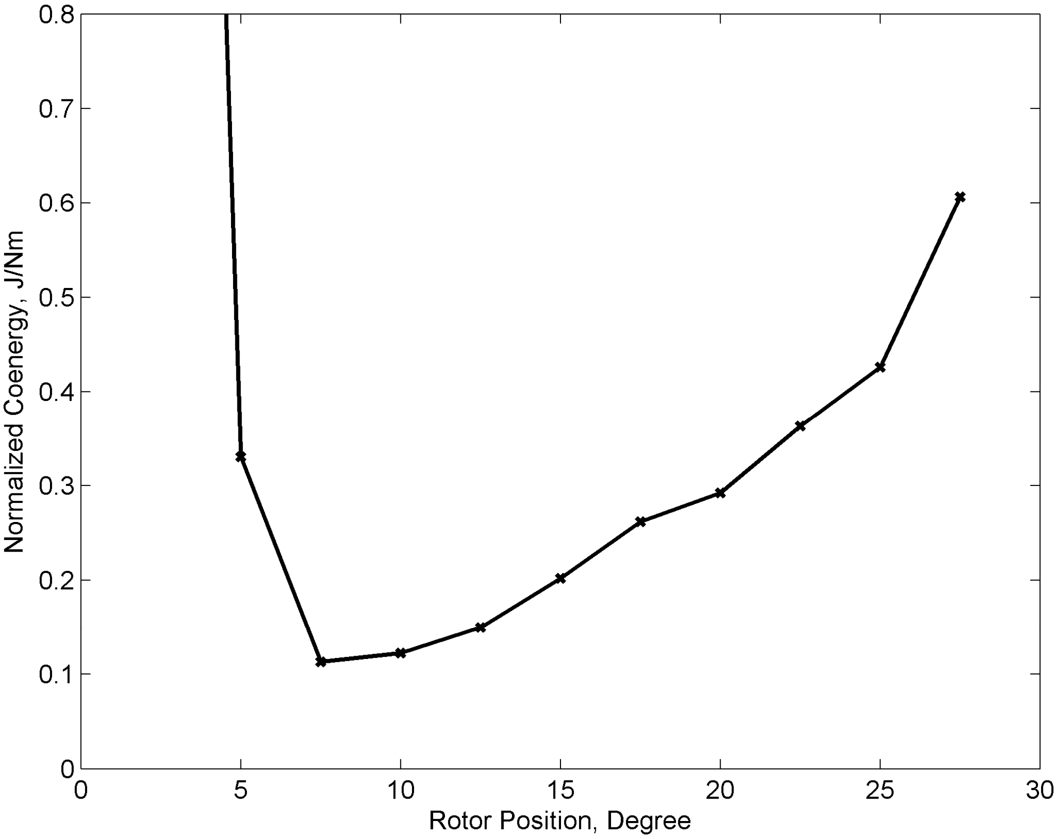

Fig. 4.1 Normalised co-energy profile of an SRM

The required co-energy of each phase to output the required torque at each rotor position can be calculated:

$$W_c^* = W_{c\,norm}(\theta)T^* \tag{4.8}$$

where T^* is the torque command of the phase.

Fig. 4.2 shows the relationship between the co-energy and torque of the SRM, of which the magnetic data are measured experimentally. The operating region with a maximum torque output of 8.5 Nm using a commutation scheme, which will be described in Section 4.3.3, is enclosed in dotted lines for reference.

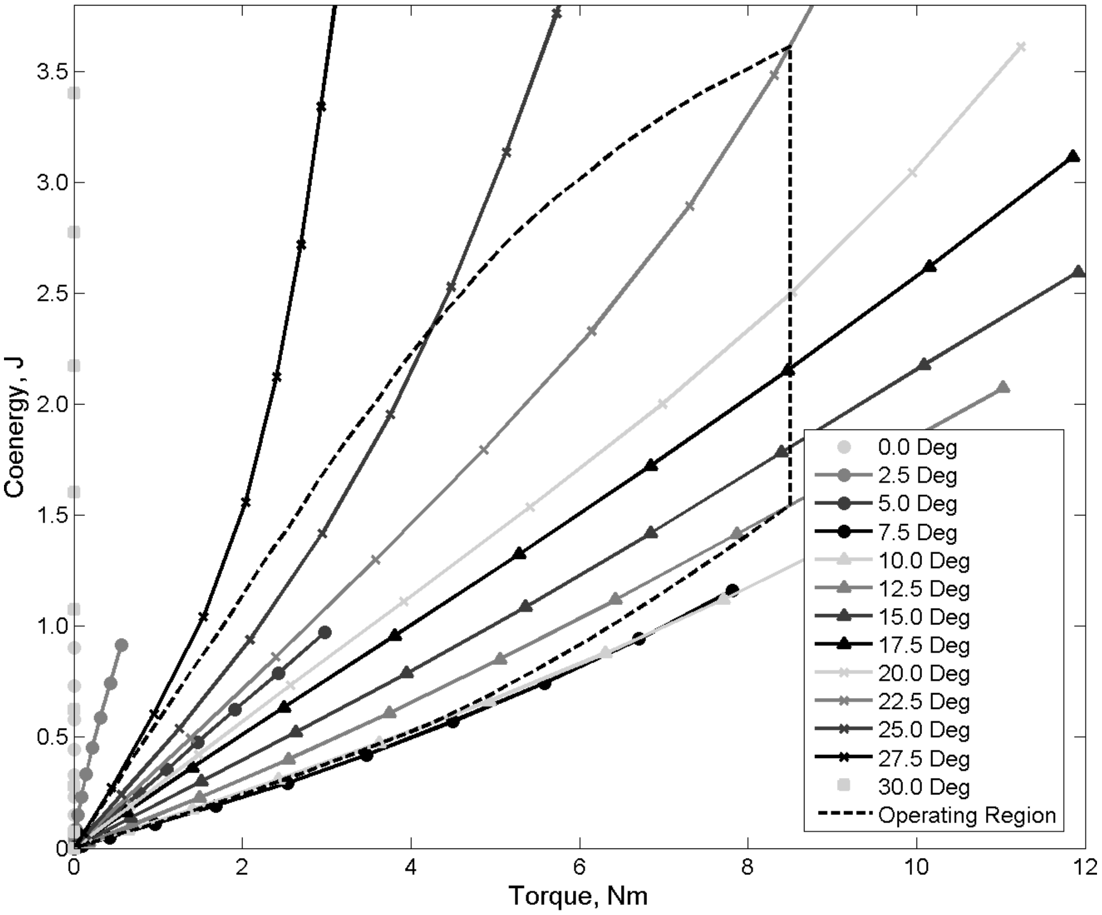

Fig. 4.2 Relationship between co-energy and torque at various rotor positions

It is worth noting that even though the co-energy profile is obtained at low current, the linear extrapolation of it into the saturating region with (4.8) is acceptable. At each rotor position, the co-energy and torque have essentially a linear relationship that extends from unsaturated to saturating regions, especially within the operating region. Consequently, it can be assumed that, provided the co-energy can be estimated online with the magnetic nonlinearity between co-energy and current taken into account, the torque can be controlled by regulating the co-energy to follow the product of the normalised profile and the torque command.

4.3 Implementation

Fig. 4.3 depicts the structure of the proposed instantaneous torque controller. The torque references T^* and rotor position are used to calculate the co-energy commands W_c^* of each phase. The co-energy regulator then controls the required motor terminal voltages v_{phase} based on the estimated co-energies from the co-energy estimator and co-energy commands to ensure the co-energy of the SRM follows the co-energy commands. The PWM modulator outputs the PWM switching signals to the SRM power converter, which is a power electronic stage consisting of asymmetrical half-bridges. The terminal voltage signals, phase currents and rotor position are used to estimate the co-energies for co-energy control.

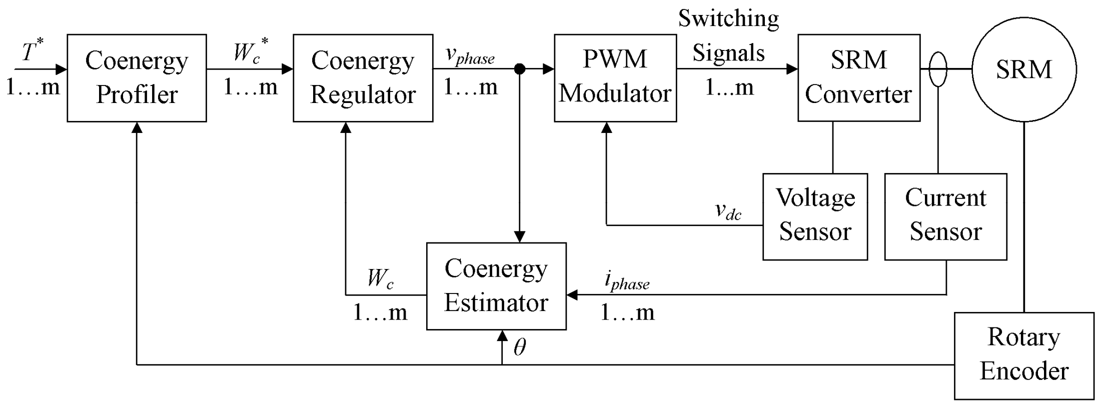

Fig. 4.3 Structure of the instantaneous torque controller for the SRM

4.3.1 Co-energy estimation

The estimation of co-energy is based on the co-energy estimator derived in Chapter 3. With the motor terminal quantities and a few premeasured magnetic data, the co-energy of each phase can be estimated.

4.3.2 Co-energy regulator

To design the co-energy regulator, the dynamics between the output voltage and co-energy have to be determined. The equation describing the electrical dynamics is:

$$v_{phase} = l\frac{di_{phase}}{dt} + i_{phase}R + e \tag{4.9}$$

where *e* is a back-EMF term. Co-energy is defined as:

$$W_c(\theta, i_{ph}) = \int_0^{i_{phase}} \lambda(\theta, i)\,di \tag{4.10}$$

For a small increment of co-energy ΔW_c and with due consideration of magnetic saturation, (4.10) becomes,

$$\Delta W_c = Li_{phase}\,\Delta i_{phase} + \tfrac{1}{2}\,l\,\Delta i_{phase}^2 \tag{4.11}$$

Dropping the high order term for small signal system design,

$$\Delta W_c = Li_{phase}\Delta i_{phase} \tag{4.12}$$

Treating the back EMF term as disturbance and expressing (4.9) and (4.12) in the s-domain, one obtains:

$$\frac{\Delta i_{phase}(s)}{\Delta v_{phase}(s)} = \frac{1/l}{s + R/l} \tag{4.13}$$

$$\frac{\Delta W_c(s)}{\Delta i_{phase}(s)} = Li_{phase} \tag{4.14}$$

The control system with G_c as the controller is illustrated in Fig. 4.4.

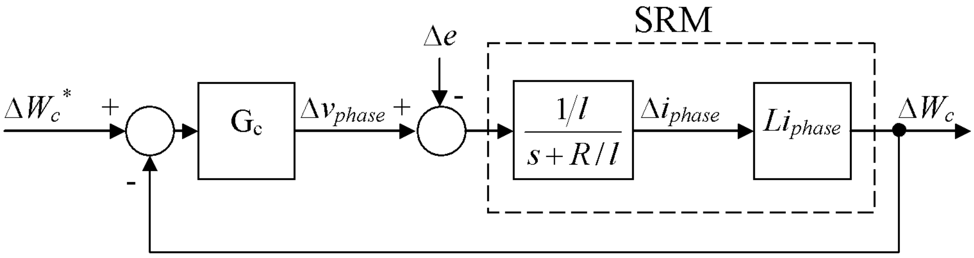

Fig. 4.4 Signal flow of the co-energy control system

G_c is a proportional integral (PI) controller of the form:

$$G_c = K_p \left(\frac{s + 1/T_i}{s} \right) \tag{4.15}$$

where K_p and T_i are the proportional and integrator constants, respectively. The time delays of the current sensor, signal conditioning circuit and power drive are neglected in designing the controller, as they are small, relative to the switching frequency and the output bandwidth, which is discussed later in this section. For higher output bandwidth, however, they have to be considered. The open-loop transfer function is

$$H(s) = K_p\, k\, i_{phase} \frac{s + {}^{1}\!/_{T_i}}{s\left(s + {}^{R}\!/_{l}\right)} \tag{4.16}$$

where k is the ratio of the bulk inductance to incremental inductance. The closed-loop transfer function becomes:

$$\begin{aligned}
\frac{\Delta W_c(s)}{\Delta W_c^*(s)} &= \frac{H(s)}{1 + H(s)} \\
&= K_p\, k\, i_{phase} \frac{s + {}^{1}\!/_{T_i}}{s\left(s + {}^{R}\!/_{l}\right) + K_p\, k\, i_{phase}\left(s + {}^{1}\!/_{T_i}\right)} \\
&= \frac{K_p\, k\, i_{phase}\left(s + {}^{1}\!/_{T_i}\right)}{s^2 + s\left({}^{R}\!/_{l} + K_p\, k\, i_{phase}\right) + {}^{K_p\, k\, i_{phase}}\!/_{T_i}}
\end{aligned} \tag{4.17}$$

For over-damped closed-loop response, the poles of the transfer function have to be real.

$$\left({}^{R}\!/_{l} + K_p\, k\, i_{phase}\right)^2 - {}^{4K_p\, k\, i_{phase}}\!/_{T_i} \geq 0 \tag{4.18}$$

If $K_p k i_{phase}$ is considerably larger than R/l, (4.18) becomes:

$$\begin{aligned}
\left(K_p\, k\, i_{phase}\right)^2 &\geq {}^{4K_p\, k\, i_{phase}}\!/_{T_i} \\
K_p\, k\, i_{phase} &\geq {}^{4}\!/_{T_i}
\end{aligned} \tag{4.19}$$

For critically-damped closed-loop response, the product of the proportional gain and phase current should meet the following condition:

$$K_p\, k\, i_{phase} = 4/T_i \tag{4.20}$$

In fact, the closed-loop response of the system is essentially independent of inductance if the product of the proportional constant K_p and phase current i_{phase} is large. In order to eliminate the effect of phase current on the system response, the proportional constant is scheduled to be inversely proportional to the phase current.

It is recommended [80] that the sampling frequency F_s of the digital controller is set to 10 to 50 times of the closed loop bandwidth. Using a factor of 10 in this application, one has

$$\text{Bandwidth} = K_p\, k\, i_{phase} = \frac{2\pi F_s}{10} \tag{4.21}$$

The scheduled proportional constant $K_p i_{phase}$ should be set to a small value such that the system remains stable. However, if the constant is too small, the dynamic response becomes slow. Considering the range of ratio k is between 1 and 2.5 [81] in general, and leaving some safety margin for the controller to give a satisfactory response, the scheduled proportional constant is set as:

$$K_p\, i_{phase} = \frac{2\pi F_s}{30} \approx \frac{F_s}{5} \tag{4.22}$$

The integral time constant is then set as,

$$T_i = 4/K_p i_{phase} \tag{4.23}$$

The change of inductance with rotor position, which affects the value of *k*, may introduce non-linearities to the transfer function to the system. Because the rotor speed is relatively low, the non-linearities are considered as a disturbance to the system. To analyse the effects of the back EMF stated in (4.9) and Fig. 4.4, and non-linearities, the closed-loop transfer function from the disturbance to the co-energy output is derived:

$$\begin{aligned}\frac{\Delta W_c(s)}{\Delta E(s)} &= \frac{-\dfrac{k\,i_{phase}}{s+R/l}}{1+\dfrac{k\,i_{phase}}{s+R/l}\left(K_p\dfrac{s+1/T_i}{s}\right)} \\ &= \frac{-k\,i_{phase}\,s}{s^2+\left(K_p\,k\,i_{phase}+R/l\right)s+K_p\,k\,i_{phase}/T_i} \\ &\approx \frac{-k\,i_{phase}\,s}{s^2+K_p\,k\,i_{phase}s+K_p\,k\,i_{phase}/T_i}\end{aligned} \tag{4.24}$$

Equation (4.24) shows that the poles are the same as those of (4.17) and the system is stable, has a high bandwidth with small rise time, as designed. In addition, as the denominator of (4.24) is denominated by K_pki_{phase} and the nominator is governed by ki_{phase}, the influence of the disturbance is significantly attenuated by the proportional constant of the regulator. Hence, the co-energy regulator requires no feed-forward compensation.

It should be noted that the controller is converted to z-domain for implementation in digital controller, although it is designed in s-domain. S-domain is used throughout the design process because it is more intuitive for system identification and dynamic response. In fact, the system parameters and information of the process plant are obtained in s-domain. Though designing in z-domain allows higher output bandwidth, it may introduce noise amplification and voltage saturation of the power drive, which are undesirable for controller design.

4.3.3 Commutation

The conduction angles of each phase are equal and have the same constant value. During commutation, the torque command is decomposed into two references for the incoming and outgoing phases. The outgoing torque reference decreases linearly as the rotor angle increases, while the incoming torque reference increases linearly at the same time. Hence, the total torque output will remain largely constant to result in a smooth output torque.

4.4 Results

4.4.1 Simulation

The proposed scheme is simulated in MATLAB/Simulink environment. The SRM has 4 phases, 8/6 poles, rated at 2.2 kW with a maximum input voltage of 270 VDC. The sampling rate and PWM frequency of the simulated controller are 10 kHz. A DC voltage of 180 V is used for the power stage. The motor runs at 240 RPM. The torque reference is 3 Nm and each phase conducts from 7.5° to 27.5°, where 0° corresponds to the unaligned position.

Simulation waveforms of co-energy and co-energy references, with consideration of PWM switching, are displayed in Fig. 4.5. It can be seen that the co-energy can stably track the co-energy command.

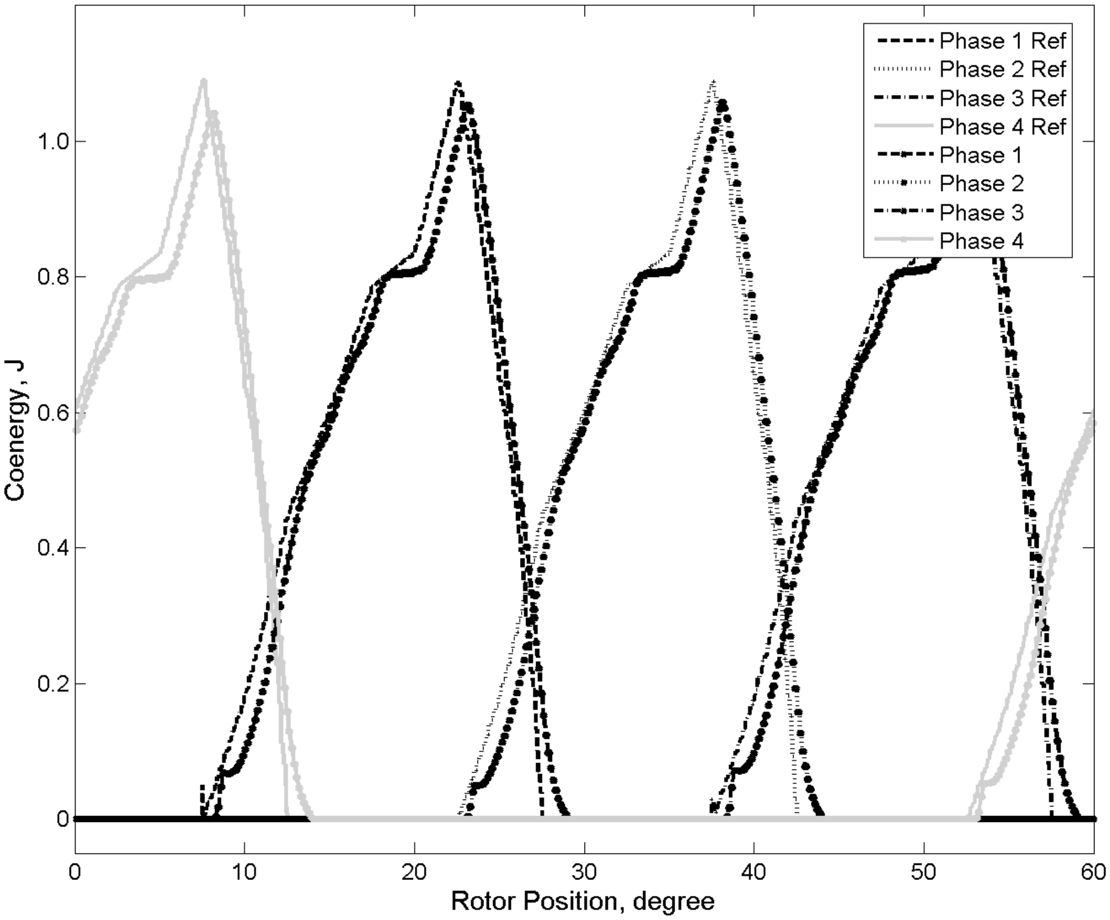

Fig. 4.5 Simulated co-energy references and co-energy waveforms

The torque command and output of each phase are compared in Fig. 4.6. It can be seen that the torque output of each phase follows the command. The slight drops of the torque around 10° and 20° are because of the coarse resolution of the co-energy profile. As the co-energy profile is spaced at 2.5°, linear interpolation is required for rotor positions between the data points, which may not match the required co-energy exactly. Also, the use of numerical differentiation in (4.7) to obtain the torque for the computation of the normalised co-energy profile may introduce errors.

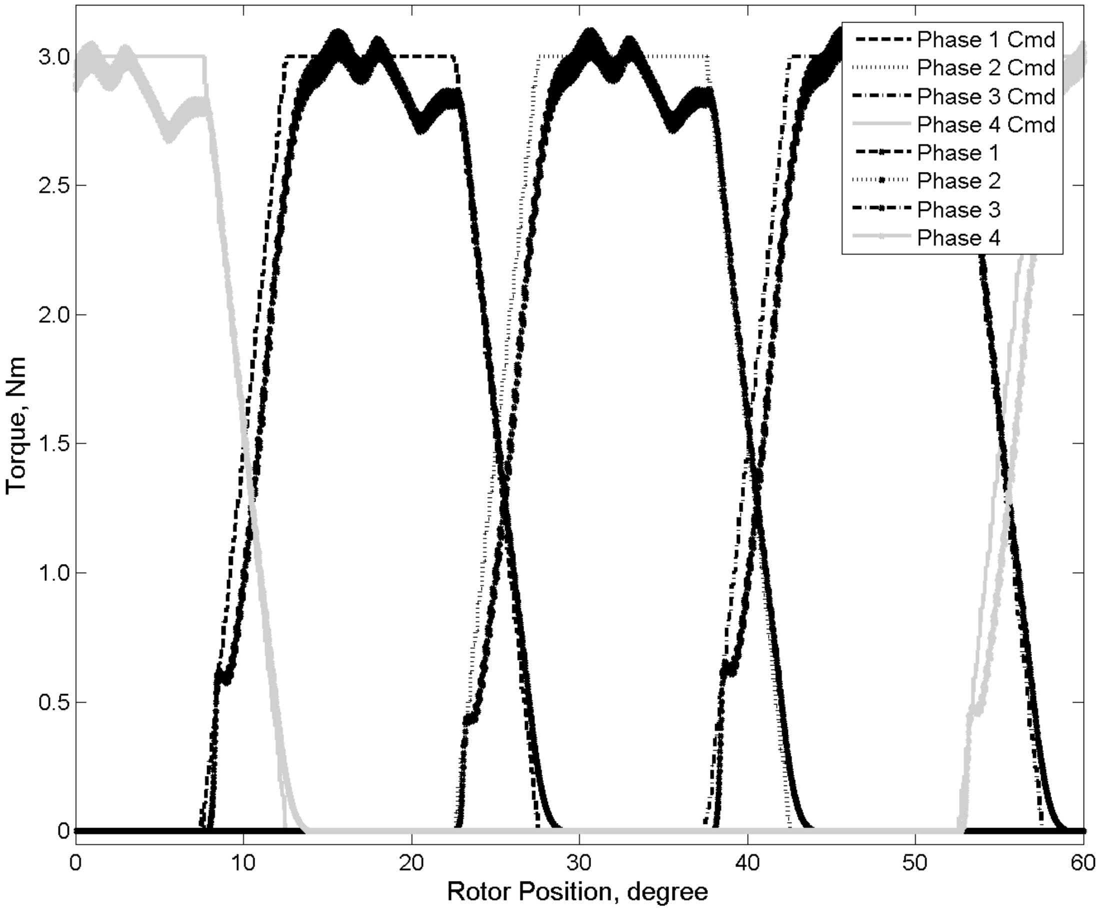

Fig. 4.6 Simulated torque commands and torque outputs

Simulation waveform of the phase currents and output torque are shown in Fig. 4.7. For comparison, the simulated waveforms under standard constant current control at 4.5 A are given in Fig. 4.8. It should be noted that the high frequency torque ripple due to PWM switching does not appear clearly in Fig. 4.7 because there are around 420 switching cycles for a rotor movement of 60 mechanical degrees as shown in the figure. The torque ripples would appear clearly if the time scale of Fig. 4.7 could be expanded to show only a couple of milliseconds.

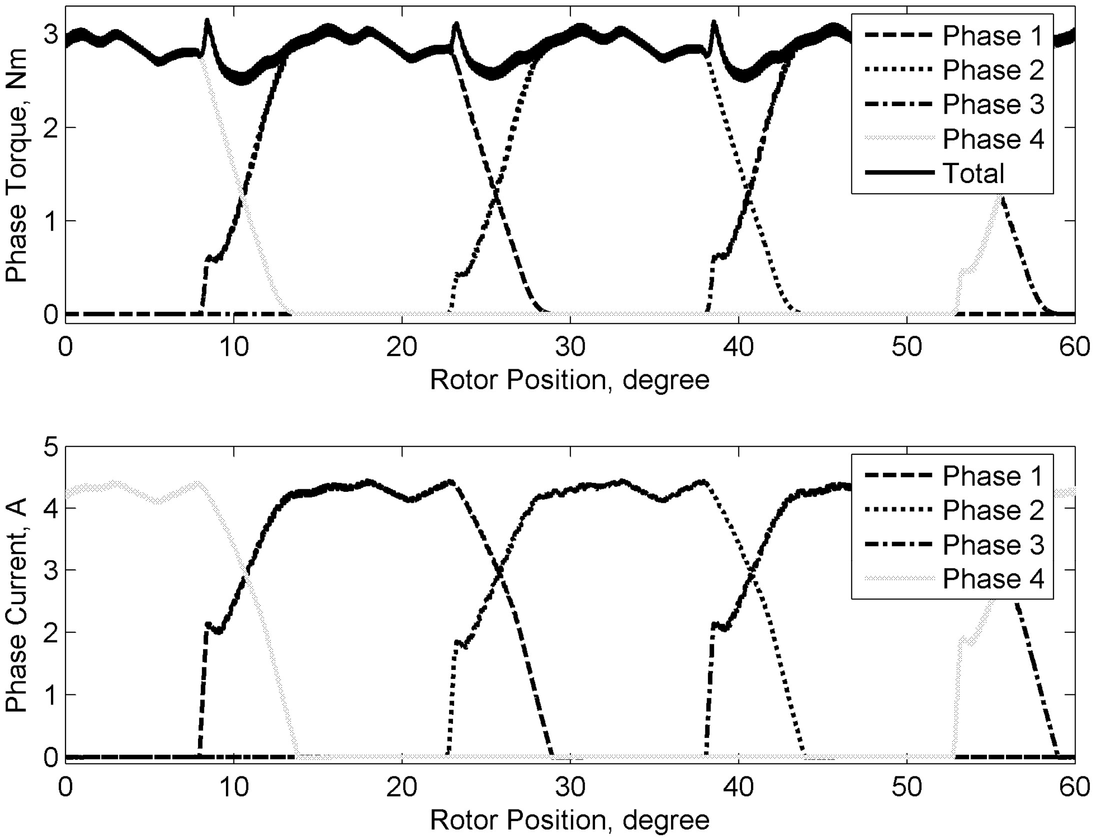

Fig. 4.7 Simulated torque and current waveforms under co-energy control

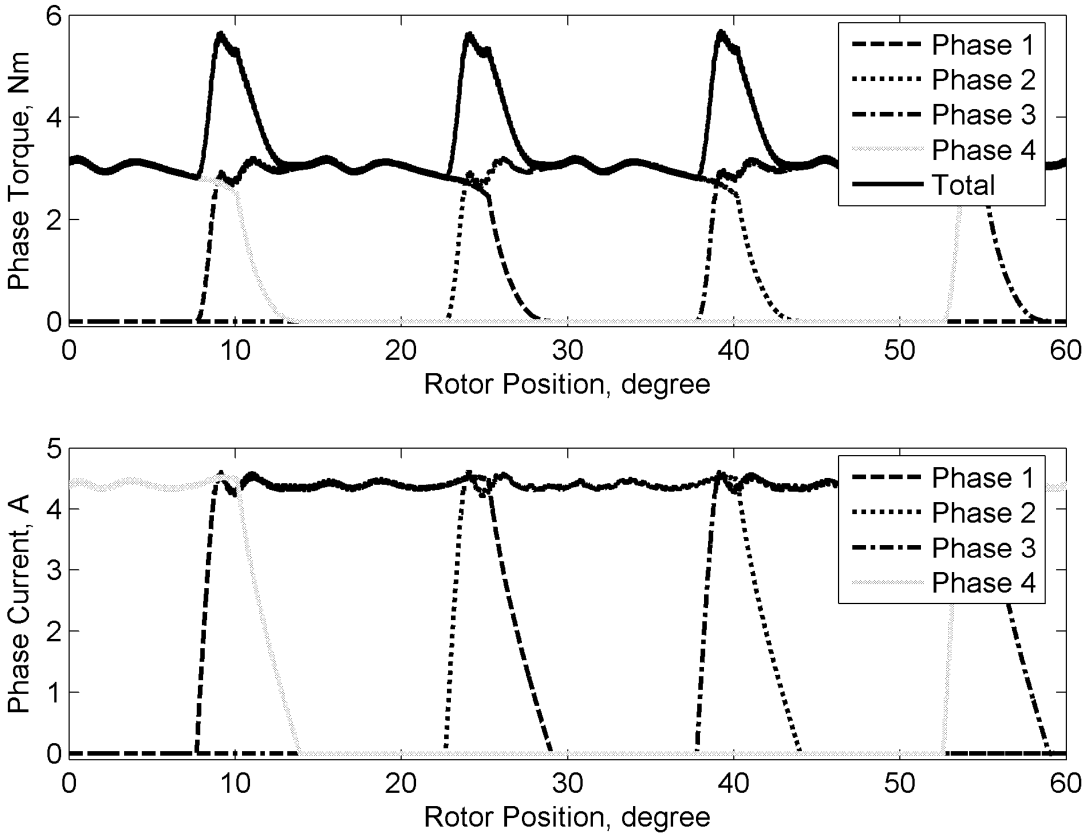

Fig. 4.8 Simulated torque and current waveforms under standard constant current control

The simulation results show that the electromagnetic torque output of the scheme can follow the torque command with the proposed control scheme, despite the slight torque ripple due to the resolution and derivation errors of the co-energy profile, and the PWM switching of the converter. In addition, it outputs less torque ripple when compared with that produced with standard current control, especially during commutation. Comparing to DITC [43], [64], which performs direct torque control and should output low torque ripples, the co-energy control scheme outputs similar torque ripple of 15%, but requires less pre-measured magnetic data.

4.4.2 Experiment

An experiment is conducted with an environment similar to that of the simulation. A dSpace 1104 prototyping controller board is used as the digital controller. Customised power drive and sensors board are utilised in the experiment. The details of the circuits and wiring are given in Appendix 8.2. A separately excited DC generator, with the armature connected to variable resistors, is used as the load machine. Between the SRM and the load machine, a torque transducer is coupled for dynamic torque measurement. The transducer is Burster 8651-5020, of which the signal bandwidth is 200 Hz, and its moment of inertia is negligible.

Fig. 4.9 shows the experimental shaft torque and current waveforms of the proposed control scheme. The simulation results are also presented on the same graph for the sake of comparison. The current waveforms obtained from the experiment and simulation are similar, while the average torques are also comparable. It should be noted that a portion of the high frequency torque ripples is filtered by the moment of inertia of the SRM, mechanical coupling, and the bandwidth limit of the torque transducer. The low frequency torque ripples of 24 Hz are the result of the mechanical coupling between the load machine, torque transducer and SRM. As each pair of the mechanical couplers is linked by six pins and a rubber disc, the machines oscillate at 6 times of the mechanical frequency, which is 4 Hz for a motor speed of 240 RPM. The ripples of the proposed controller with a period shorter than the electrical period, albeit small, are the result of the coarse resolution and imperfectness of the co-energy profile, as discussed in the last section.

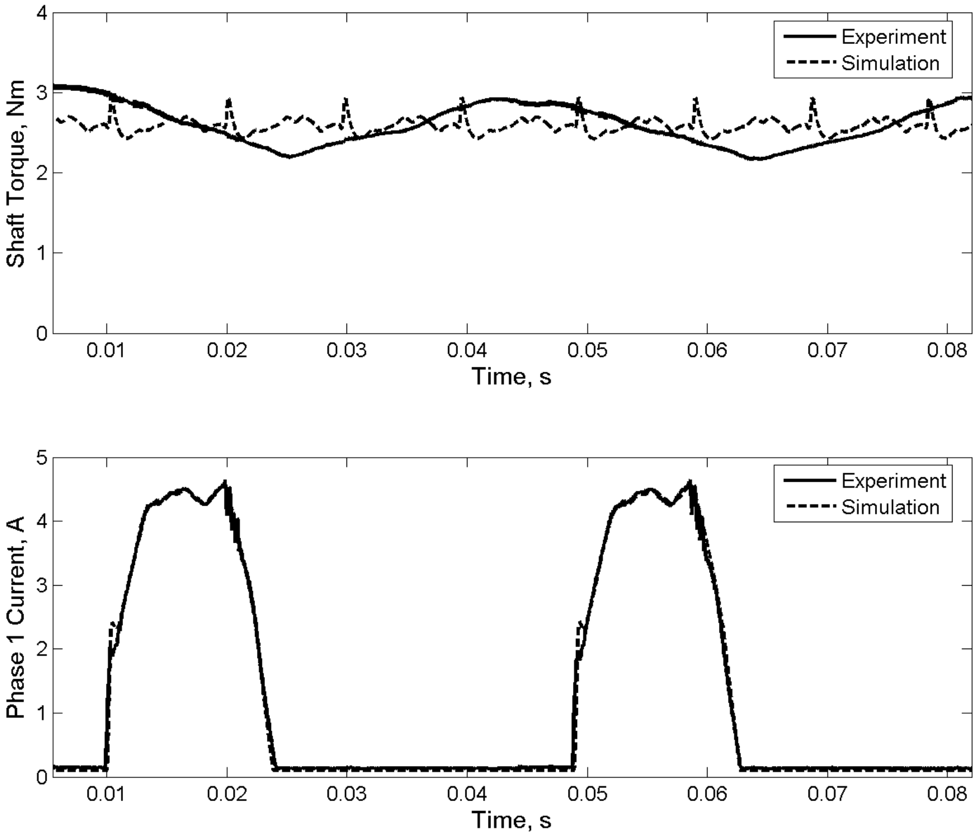

Fig. 4.9 Measured shaft torque and phase 1 current under co-energy control

Fig. 4.10 depicts those obtained using standard constant current control to illustration the differences between the proposed and traditional control algorithms. The experimental waveforms show that with the use of the proposed co-energy control scheme, the SRM outputs relatively less high frequency shaft torque ripples when compared to those produced using standard current control. Comparing to the estimated torque of DITC [64] again, the magnitudes of the torque ripples are similar. In fact, the performances of the proposed controller are comparable to those using torque directly as feedback signal.

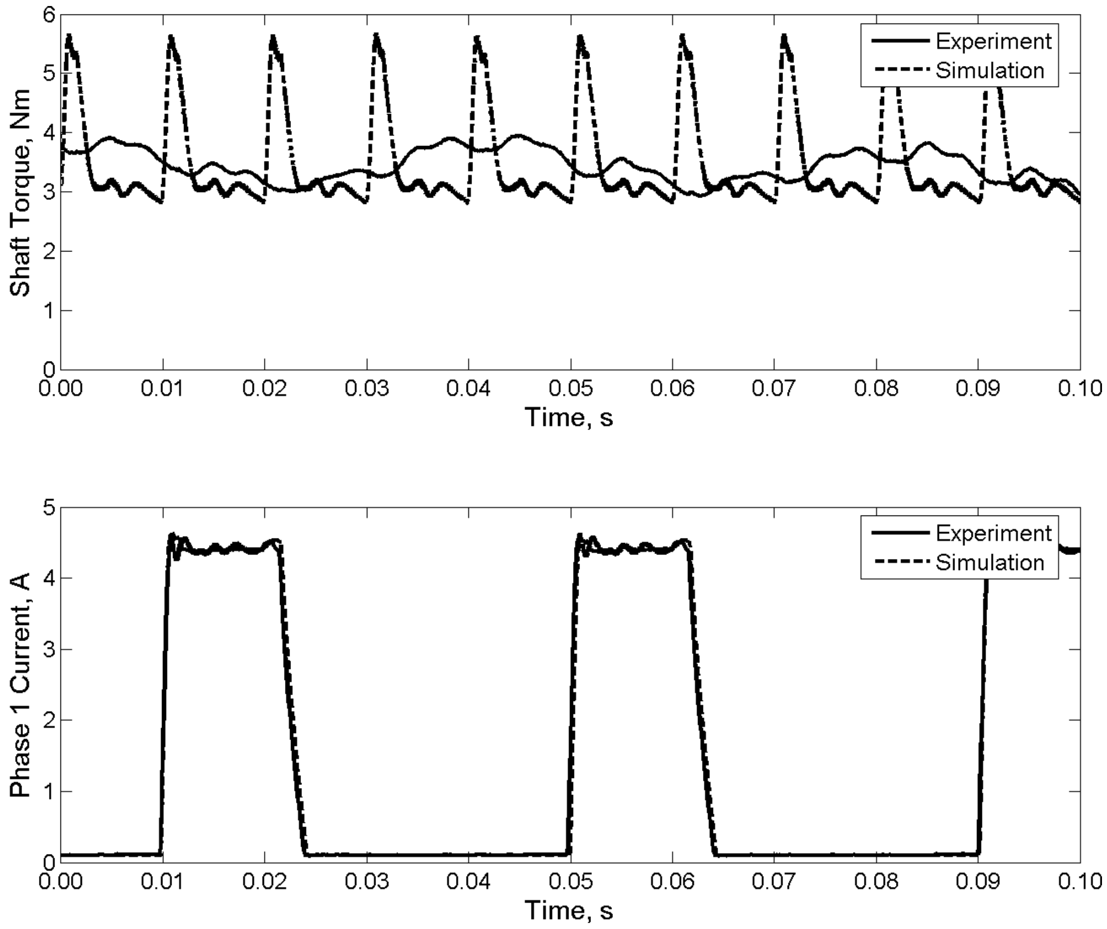

Fig. 4.10 Measured shaft torque and phase 1 current under standard constant current control

4.5 Summary

This chapter presents a scheme to independently control the instantaneous torque of each active phase of an SRM online, via co-energy control. Relationship between torque output and co-energy is derived. The co-energy of each phase is regulated to follow a co-energy profile, which is obtained from the magnetic characteristics at low current. Because the co-energy profile is a one-dimensional table, the scheme only requires small memory space for pre-measured data. Stability analysis shows that the parameters for stable operation of the control system are independent of motor parameters. Hence, the design of the proposed controller becomes simple. During commutation, the electrical torque output is shared among the active phases through torque profiling. Computer simulation and experiment results confirm that the scheme outputs a smooth torque that follows the torque command.

5 Four-quadrant Torque Control

5.1 Introduction

Four-quadrant operation of SRM is preferred to one-quadrant operation for many highly dynamic applications in, for example, electric vehicles (EV) and robots. In contrast with simple control that stops the SRM by freewheeling, regenerative braking has the beauty of recycling the kinetic energy stored in the rotating mass back to the source to improve the overall system efficiency. In addition, the braking force that appears during regeneration reduces the braking time and hence increases the dynamic performance of the drive. The improvements are particularly significant when frequent start/stop operations are required.

Torque control for four-quadrant operation of SRM has been reported in only a few literatures. Instantaneous torque control based on torque feedback, and average torque control using current control, are introduced in [43] and [55] respectively. All these algorithms require different control schemes for motoring and regenerating operation, thereby resulting in complex controllers.

Extending from Chapter 4, this chapter presents an instantaneous torque control scheme for four-quadrant operation at low speed based on co-energy which is estimated from the machine terminal quantities and the low-current machine inductances. Even though the SRM normally operates with deep saturation, only the inductance data obtained at low current are sufficient for the bulk of the practical operating range. The SRM is then controlled to follow a co-energy profile in accordance to a torque sharing function for constant electromagnetic torque output.

The scheme has the advantage of requiring minimal pre-measured data, when compared with current-profiling schemes. The co-energy controller is designed based on the concept of internal model control. The direction of torque production is controlled by altering the excitation sequence of the phases. The controller is intrinsically capable to operate in both motoring and regenerating modes. Operating limits of the control scheme are analysed and reported in this paper. Both computer simulation and experimental verification confirm that the scheme is feasible in practical situations.

5.2 Instantaneous torque control

5.2.1 Torque sharing function

The torque command is resolved into two phase-torque commands for the active phases, according to a torque sharing function during commutation. It ensures a smooth transition of torque contribution. Within the active region of the phase, the phase torque command is expressed as:

$$T^{*} = \left|T_{cmd}\right| \mathrm{TSF}\left(\theta_{ph}\right) \tag{5.1}$$

where T_{cmd} is the torque command of the machine, TSF(θ_{ph}) is the torque sharing function, and θ_{ph} is the relative rotor position of the phase:

$$\mathrm{TSF}(\theta_{ph}) = \begin{cases} 0 & \theta_{ph} < \theta_{c1} \\ \mathrm{f}_{\mathrm{rise}}\left(\theta_{ph}\right) & \theta_{c1} \le \theta_{ph} < \theta_{c2} - \theta_{phase} \\ 1 & \theta_{c2} - \theta_{phase} \le \theta_{ph} < \theta_{c1} + \theta_{phase} \\ \mathrm{f}_{\mathrm{fall}}\left(\theta_{ph}\right) & \theta_{c1} + \theta_{phase} \le \theta_{ph} < \theta_{c2} \\ 0 & \theta_{c2} \le \theta_{ph} \end{cases} \tag{5.2}$$

where; θ_{phase} is the phase shift between the phases; $\mathrm{f}_{\mathrm{rise}}(\theta_{ph})$ and $\mathrm{f}_{\mathrm{fall}}(\theta_{ph})$ denote the rising and falling portions of the function, respectively. Between θ_{c1} and θ_{c2}, the phase is energised. $\mathrm{f}_{\mathrm{fall}}(\theta_{ph})$ is defined by the following quadratic equation:

$$\mathrm{f}_{\mathrm{fall}}\left(\theta_{ph}\right)=k_1\theta_{ph}^2+k_2\theta_{ph}+k_3 \tag{5.3}$$

where k_1, k_2, and k_3 are coefficients to be determined. As θ_{c2} is close to the aligned position θ_a, at where the inductance is the maximum, the rate of change of torque at θ_{c2} is set to zero. Also, the function is continuous at the boundaries. The constraints of the functions are:

$$\begin{cases}\mathrm{f}'_{\mathrm{fall}}\left(\theta_{c2}\right)=0\\ \mathrm{f}_{\mathrm{fall}}\left(\theta_{c1}+\theta_{phase}\right)=1\\ \mathrm{f}_{\mathrm{fall}}\left(\theta_{c2}\right)=0\end{cases} \tag{5.4}$$

Hence, the coefficients are calculated as:

$$\begin{cases}k_1=1\Big/\left(\theta_{c2}-\theta_{c1}-\theta_{phase}\right)^2\\ k_2=-2k_1\theta_{c2}\\ k_3=k_1\theta_{c2}^2\end{cases} \tag{5.5}$$

For simplicity, equation (5.3) can be rewritten as:

$$\mathrm{f}_{\mathrm{fall}}\left(\theta_{ph}\right)=\frac{\left(\theta_{ph}-\theta_{c2}\right)^2}{\left(\theta_{c2}-\theta_{c1}-\theta_{phase}\right)^2} \tag{5.6}$$

For the rising portion, the function is complementary to the falling one:

$$\mathrm{f}_{\mathrm{rise}}\left(\theta_{ph}\right) = 1 - \mathrm{f}_{\mathrm{fall}}\left(\theta_{ph} + \theta_{phase}\right) \tag{5.7}$$

The shape of the torque sharing function is depicted in Fig. 5.1.

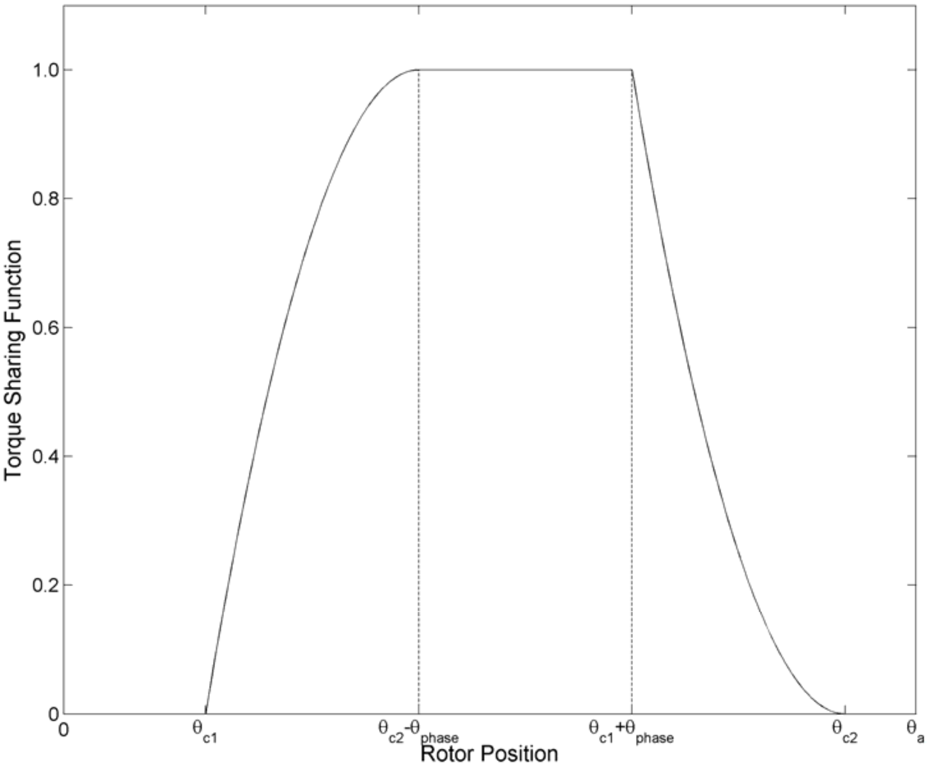

Fig. 5.1 Torque sharing function

From Fig. 5.1, it can be seen that, during commutation, the phase that is close to the unaligned position shares more torque than the one close to the aligned position. It is because the inductance of the unaligned phase is lower that of the aligned phase, thereby permitting a higher rate of change of current, and hence a higher rate of change of torque.

5.2.2 Excitation sequence for four-quadrant operation

The normalised co-energy profile $W_{c\ norm}$ of the SRM is obtained using the procedure described in Chapter 4. The required co-energy W_c^* of each phase to output the desired phase torque T^* is calculated as:

$$W_c^* = W_{c\,\mathrm{norm}}(\theta_{ph})T^* \tag{5.8}$$

When the direction of the torque output reverses, the conduction angles have to change from positions having a positive inductance slope to those with a negative slope, as shown in Chapter 1. In general, the inductance profile of SRM is symmetrical with respect to the aligned position. Hence, the change of conduction angles can be taken to be mirroring the relative rotor positions with respect to the aligned position of the phase. Consequently, the phase shift between the phases is reversed. The calculations of the relative rotor positions are:

$$\theta_1 = \begin{cases} \theta & \text{for } k_{dir} > 0 \\ 2\theta_a - \theta & \text{for } k_{dir} < 0 \end{cases} \tag{5.9}$$

$$\theta_{ph} = \theta_1 - (ph-1)k_{dir}\,\theta_{phase} \text{ for } ph > 1 \tag{5.10}$$

where; θ is the absolute mechanical rotor position, and it is set to zero for the unaligned position of phase 1; k_{dir} is the direction of the torque command, where 1 is for positive and -1 is for negative.

5.3 Four-quadrant instantaneous torque controller

The structure of the proposed four-quadrant torque controller is depicted in Fig. 5.2.

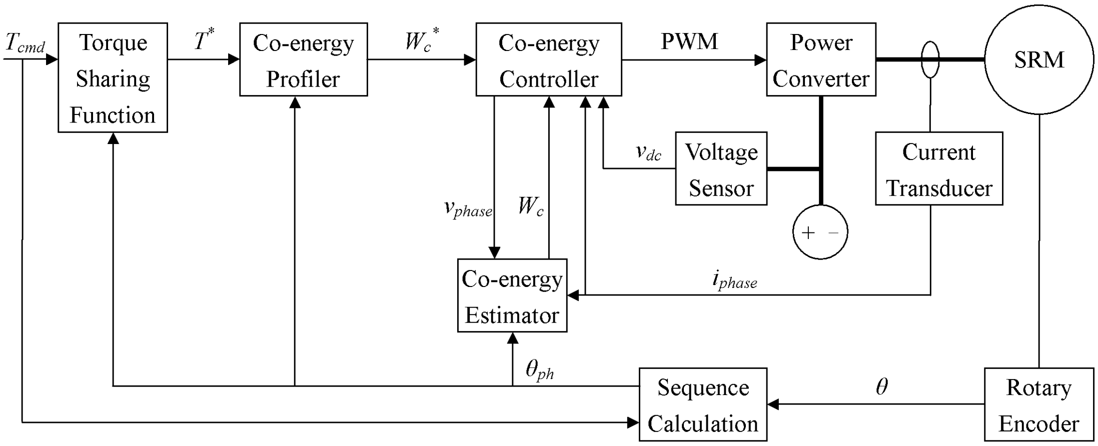

Fig. 5.2 Structure of the four-quadrant torque controller

The Torque Sharing Function derives the phase torque commands T^* from the torque command T_{cmd} according to the relative rotor position θ_{ph}. The phase torque commands are then translated into co-energy commands W_c^* using the co-energy profiler. The co-energy W_c is estimated by a co-energy estimator which is described in Chapter 3 in details. The co-energy controller controls the co-energy to track the command, and then outputs constant-frequency pulse-width-modulated (PWM) signals to the power converter. The power converter then amplifies the signals via power electronics to drive the SRM windings. The Sequence Calculation unit calculates the relative rotor positions of each phase according to the rotor position and torque command.

5.3.1 Co-energy controller

The co-energy controller is designed based on the concept of internal model control (IMC). IMC is a model-based control algorithm. It is often utilised to design controllers for plants with approximated mathematical models [82]. The general structure of IMC is depicted in Fig. 5.3.

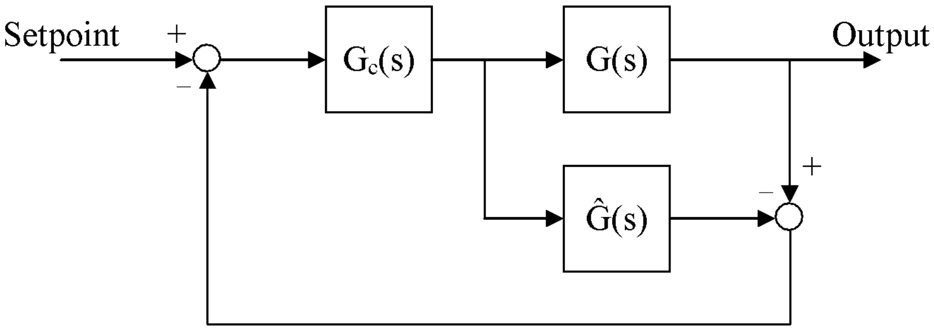

Fig. 5.3 General structure of IMC

The output of the controller $G_c(s)$ is fed to the plant $G(s)$ and an internal process model $\hat{G}(s)$. Disturbance and deviation of the model from the plant are fed back to the controller for regulation adjustment. If the model perfectly matches the plant, the transfer function between the output and set-point becomes a sequential combination of the controller and the plant. On the surface, it is natural to design the controller as the inverse of the plant, such that the output can follow the set-point instantaneously. However, such design results in over-reaction of the controller and the system becomes sensitive to model error. A plant model is factorised into the form:

$$\hat{G}(s) = \hat{G}_s(s)\,\hat{G}_u(s) \tag{5.11}$$

where; $\hat{G}_s(s)$ is the invertible portion; $\hat{G}_u(s)$ is the non-invertible portion, which is unstable or unrealisable after inverting. A practical design of the controller is:

$$G_c(s) = \hat{G}_s^{-1}(s)\,F(s) \tag{5.12}$$

where $F(s)$ is a low pass filter of the form:

$$F(s) = 1\big/(\varepsilon\, s + 1)^r \tag{5.13}$$

where ε is a filter time constant and r is the relative order of $\hat{G}_s(s)$.

For the application of IMC into SRM, the transfer function of the plant should be deduced first. As derived from Chapter 4, the transfer function from the motor terminal voltage to co-energy of the SRM is:

$$G(s) = \frac{\Delta W_c}{\Delta v_{phase}} = \frac{k\, i_{phase}}{R/l + s} \tag{5.14}$$

The internal model of the plant is:

$$\hat{G}(s) = \frac{k\, i_{phase}}{R_m/l_m + s} \tag{5.15}$$

where R_m and l_m are model phase resistance and inductance, respectively. The controller is:

$$G_c(s) = \frac{R_m/l_m + s}{k\, i_{phase}(\varepsilon\, s + 1)} \tag{5.16}$$

For stable controller design, the model inductance is chosen as the aligned inductance at low current. The bandwidth of the closed loop system is inversely proportional to the filter time constant. As suggested in [80], the sampling frequency F_s of the digital controller should be 10 to 50 times of the closed loop bandwidth. Using a factor of 10, the filter time constant is deduced as:

$$10/\varepsilon = 2\pi\, F_s \tag{5.17}$$

To improve the dynamic performance of the system, the disturbance is partially fed forward to the controller output. It is approximated by the product of the phase current, derivative of the inductance with respect to the rotor position, and the speed. The phase current is available from the sensors. The derivative of the inductance is derived from the low-current inductance profile, and the speed is calculated from the rotor position.

As the computational burden to implement IMC shown in Fig. 5.3 is too demanding for online application, an alternative IMC structure with the feeding-forward of the back EMF, as depicted in Fig. 5.4, is used.

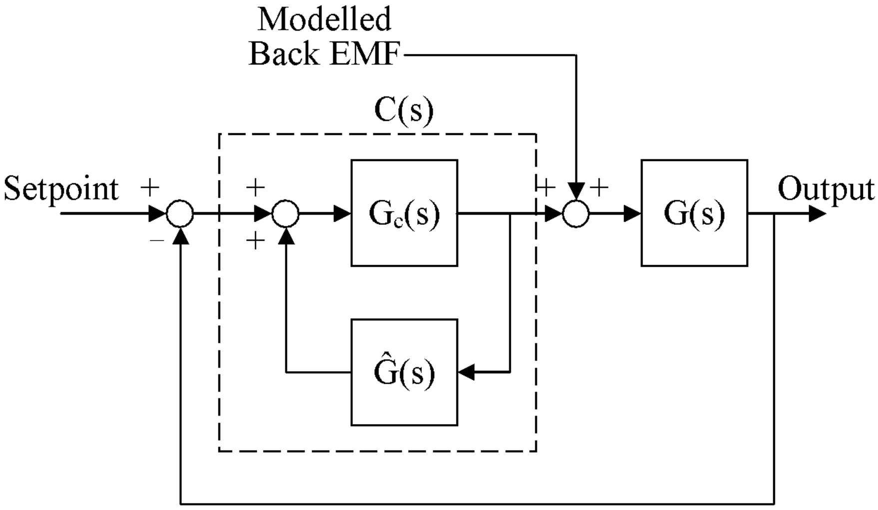

Fig. 5.4 Alternative IMC structure

The new controller *C(s)* is calculated as:

$$C(s) = \frac{G_c(s)}{1 - G_c(s)\,\hat{G}(s)} \tag{5.18}$$

Together with equations (5.15) and (5.16), one obtains:

$$C(s) = \frac{1}{i_{phase}\, k\, \varepsilon}\left(1 + \frac{R_m}{l_m s}\right) \tag{5.19}$$

k is generally between 1 and 2.5 [81]. For controller design, it should be fixed to avoid increasing the online computational burden. If the value of k is large, the dynamic response is slow but the system is stable. Likewise, the system becomes unstable if k is too small. With some safety margin, the controller is designed with k being set to a fixed value of 3. Consequently, the controller is equivalent to a traditional proportional-integral (PI) controller, with the proportional term being varied according to the phase current.

The power drive consists of conventional asymmetrical half-bridges. It outputs PWM voltages to the machine windings, according to the PWM signals from the co-energy controller. The lower IGBT operates in accordance to the polarity of the voltage command, while the upper IGBT is switched at constant frequency to control the magnitude of the average voltage output. When the voltage command is negative, the lower IGBT is switched off. Otherwise, it turns on. The duty cycle of the upper IGBT is:

$$\text{Duty Cycle} = \begin{cases} 0 & \text{when } v_{phase} \le -v_{dc} \\ 1 + v_{phase}/v_{dc} & \text{when } -v_{dc} < v_{phase} < 0 \\ v_{phase}/v_{dc} & \text{when } 0 \le v_{phase} < v_{dc} \\ 1 & \text{when } v_{dc} \le v_{phase} \end{cases} \tag{5.20}$$

where v_{dc} is the DC-link voltage. In fact, the power drive can output bi-polar voltages with the magnitude limited to the DC-link voltage. The switching scheme intrinsically allows both motoring and generating operations. When the voltage is positive, energy is fed into the winding via the IGBTs. When negative voltage is applied to the winding, the current flows through the power diodes and hence the energy stored in the winding is transferred back to the DC-link.

5.3.2 Operation limits

The torque-speed limits of the proposed scheme can be evaluated based on the available power drive voltage V_{dc}, the normalised co-energy profiles, and the inductance profiles. Assume the rotor at θ_{c2} is rotating towards $\theta_{c1}+\theta_{phase}$, at a speed ω, at the beginning:

$$\theta_{ph} = -\omega t + \theta_{c2} \tag{5.21}$$

Substituting into equations (5.1), (5.2), and (5.6), one obtains:

$$T^{*}(t) = T_{cmd}\,\frac{(\omega t)^2}{\left(\theta_{c2} - \theta_{c1} - \theta_{phase}\right)^2} \tag{5.22}$$

The maximum available flux-linkage, with full power drive voltage applied, is:

$$\lambda = V_{dc} t \tag{5.23}$$

Considering the case without saturation for simplicity of calculation,

$$W_c = \frac{1}{2}\frac{\lambda^2}{L} \tag{5.24}$$

The maximum available co-energy is:

$$W_{c\,max} = \frac{1}{2}\frac{V_{dc}^2}{L}t^2 \tag{5.25}$$

The required co-energy should be smaller than the maximum available co-energy:

$$W_c^* < W_{c\,max} \tag{5.26}$$

From (5.8),

$$T^*\,W_{c\,norm} < W_{c\,max} \tag{5.27}$$

Put in (5.22) and (5.25),

$$T_{cmd}\,\frac{(\omega t)^2}{\left(\theta_{c2}-\theta_{c1}-\theta_{phase}\right)^2}W_{c\,norm} < \frac{1}{2}\frac{V_{dc}^2}{L}t^2 \tag{5.28}$$

$$T_{cmd} < \frac{V_{dc}^2\left(\theta_{c2}-\theta_{c1}-\theta_{phase}\right)^2}{2\,W_{c\,norm}\,L\,\omega^2} \tag{5.29}$$

For a conservative evaluation of equation (5.29), the normalised co-energy and inductance should be the values at θ_{c2}, which is close to the aligned position and hence the computed errors are estimated on the high side.

As for the evaluation of the torque limit near the unaligned position, the rotor is assumed to be at θ_{c1} at the beginning and rotate towards θ_{c2}-θ_{phase}:

$$\theta_{ph} = \omega\,t + \theta_{c1} \tag{5.30}$$

Substituting equations (5.2), (5.6), (5.7), and (5.30) into (5.1):

$$T^*(t) = T_{cmd}\left(1 - \frac{\left(\omega t + \theta_{c1} + \theta_{phase} - \theta_{c2}\right)^2}{\left(\theta_{c2} - \theta_{c1} - \theta_{phase}\right)^2}\right) \tag{5.31}$$

The rate of increase of the required co-energy is:

$$\frac{dW_c^*}{dt} = W_{c\,norm}\frac{dT^*}{dt} = 2W_{c\,norm}T_{cmd}\left(\frac{\omega}{\left(\theta_{c2} - \theta_{c1} - \theta_{phase}\right)} - \frac{\omega^2 t}{\left(\theta_{c2} - \theta_{c1} - \theta_{phase}\right)^2}\right) \tag{5.32}$$

Comparing equation (5.32) with the rate of increase of the maximum available co-energy:

$$\frac{dW_{c\,max}}{dt} = \frac{V_{dc}^2}{L}t \tag{5.33}$$

The maximum available co-energy cannot follow the required co-energy at the beginning. If slight insufficiency of torque output is tolerated for a very short period of time, which results in a torque dip of less than 2%, the available co-energy can fulfil the requirement afterwards. For example, when

$$t = 0.05\frac{\left(\theta_{c2} - \theta_{c1} - \theta_{phase}\right)}{\omega} \tag{5.34}$$

The co-energy requirement, as derived from (5.25), (5.27) and (5.31), becomes:

$$T_{cmd}\left(1 - (0.05 - 1)^2\right)W_{c\,norm} < \frac{1}{2}\frac{V_{dc}^2}{L}\left(0.05\frac{\left(\theta_{c2} - \theta_{c1} - \theta_{phase}\right)}{\omega}\right)^2 \tag{5.35}$$

$$T_{cmd} < \frac{V_{dc}^2}{2L\,W_{c\,norm}}\frac{\left(\theta_{c2} - \theta_{c1} - \theta_{phase}\right)^2}{\omega^2}\frac{0.05^2}{1 - (0.05 - 1)^2} \tag{5.36}$$

The operation limit of the scheme is the smallest one of the values computed from equations (5.29), (5.36) and the torque constraints imposed by the current limit of the machine windings. In general, for very low speeds, the limit is constant because of the current limit. For higher speeds, the limit has an inverse square relationship with the rotor speed.

As an example, the operation limits of a 2.2 kW 270 VDC 8/6 SRM, with a power drive voltage of 180 V and controlled under the proposed scheme, are displayed in Fig. 5.5. In general, the operation limits are lower than the ratings specified by the manufacturers. It is because the ratings are usually obtained with two phases simultaneously conducting so as to output a higher torque at the expense of excessive torque ripple. However, the proposed scheme is aiming to produce outputs with low torque ripples.

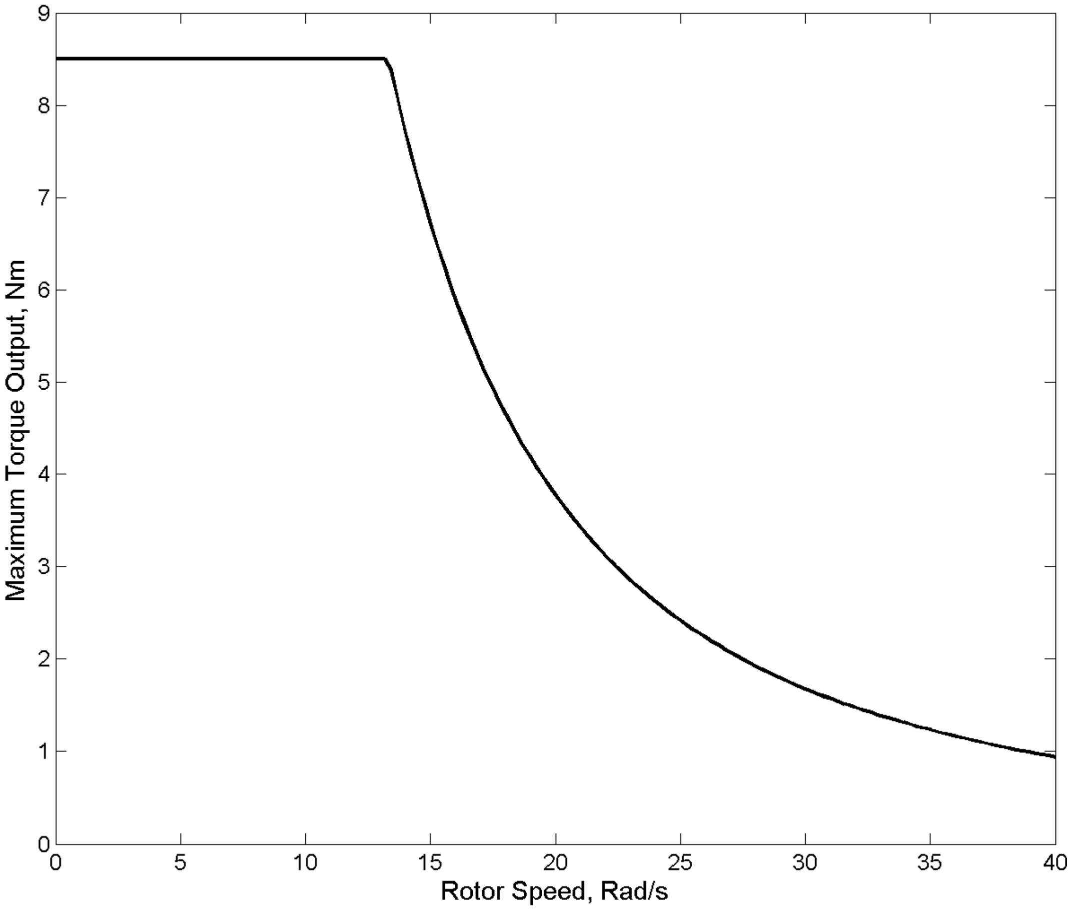

Fig. 5.5 Operation limit of a 2.2 kW 8/6 SRM

5.4 Results

5.4.1 Simulation

The proposed torque control algorithm is simulated in Matlab/ SimPowerSystems environment. Non-linear machine data of a 2.2 kW 4-phase 8/6 SRM is used. Both the sampling frequency of the controller and the switching frequency of the power electronic switches are 10 kHz. A DC-linkage voltage of 180 V is used in the simulation of the power converter. The conduction angles are between 7.5° to 27.5°.

Fig. 5.6 shows the simulation waveforms of the co-energy and co-energy command when the machine is commanded to output 4 Nm in the motoring mode at 230 RPM, which is close to the operation limit. It shows that the co-energy can closely track the command.

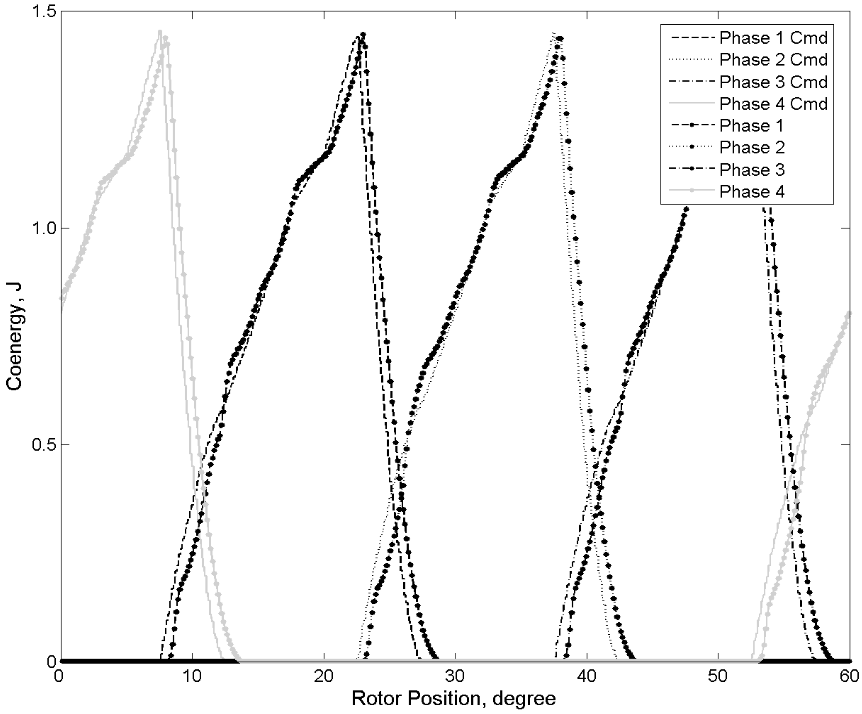

Fig. 5.6 Simulated co-energy command and co-energy waveforms

The torque and current waveforms under co-energy control are shown in Fig. 5.7. It can be seen that even if the phase current goes into the saturating region which starts at 4 A, the controller can control the machine to produce outputs in accordance to the torque command.

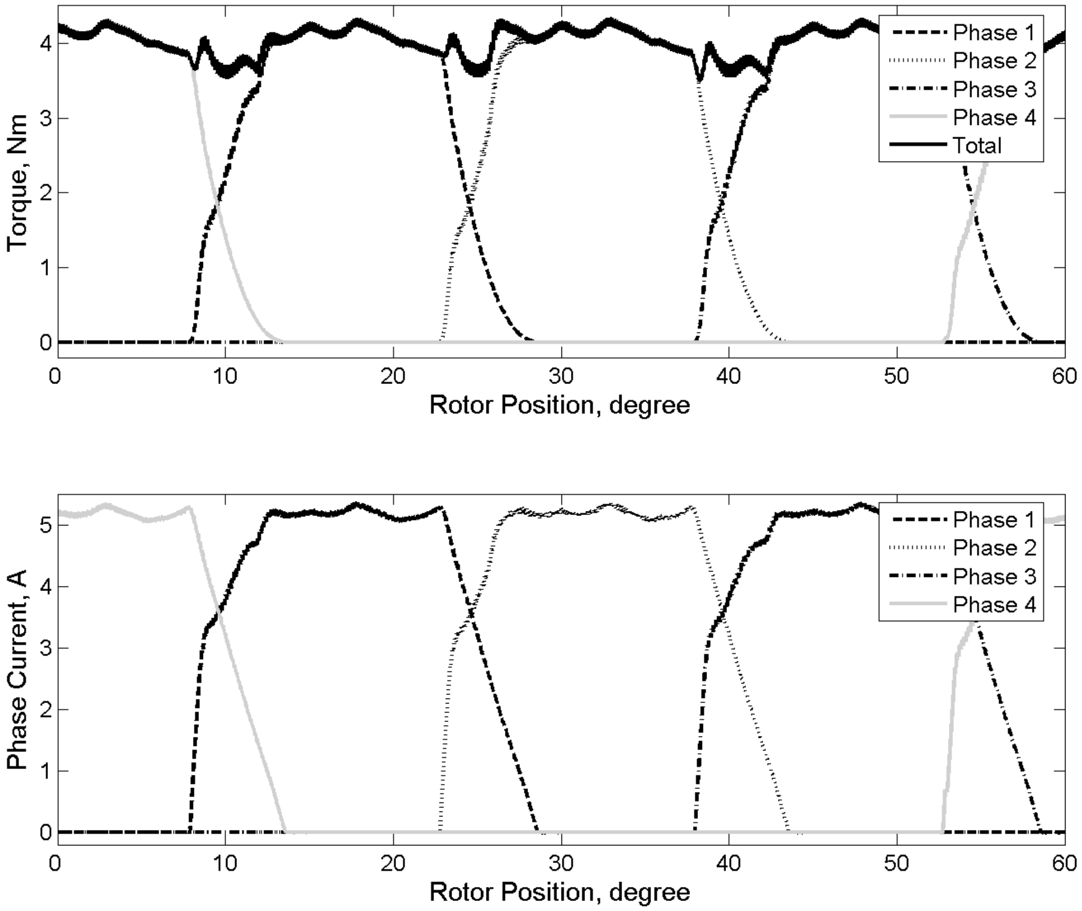

Fig. 5.7 Torque and current waveforms in motoring under co-energy control

For comparison, the torque and current waveforms of the SRM under traditional constant current control is displayed in Fig. 5.8. The current command is set to 5 A, which is close to the peak phase current using co-energy control. It shows that the proposed co-energy control scheme significantly reduces the torque ripple.

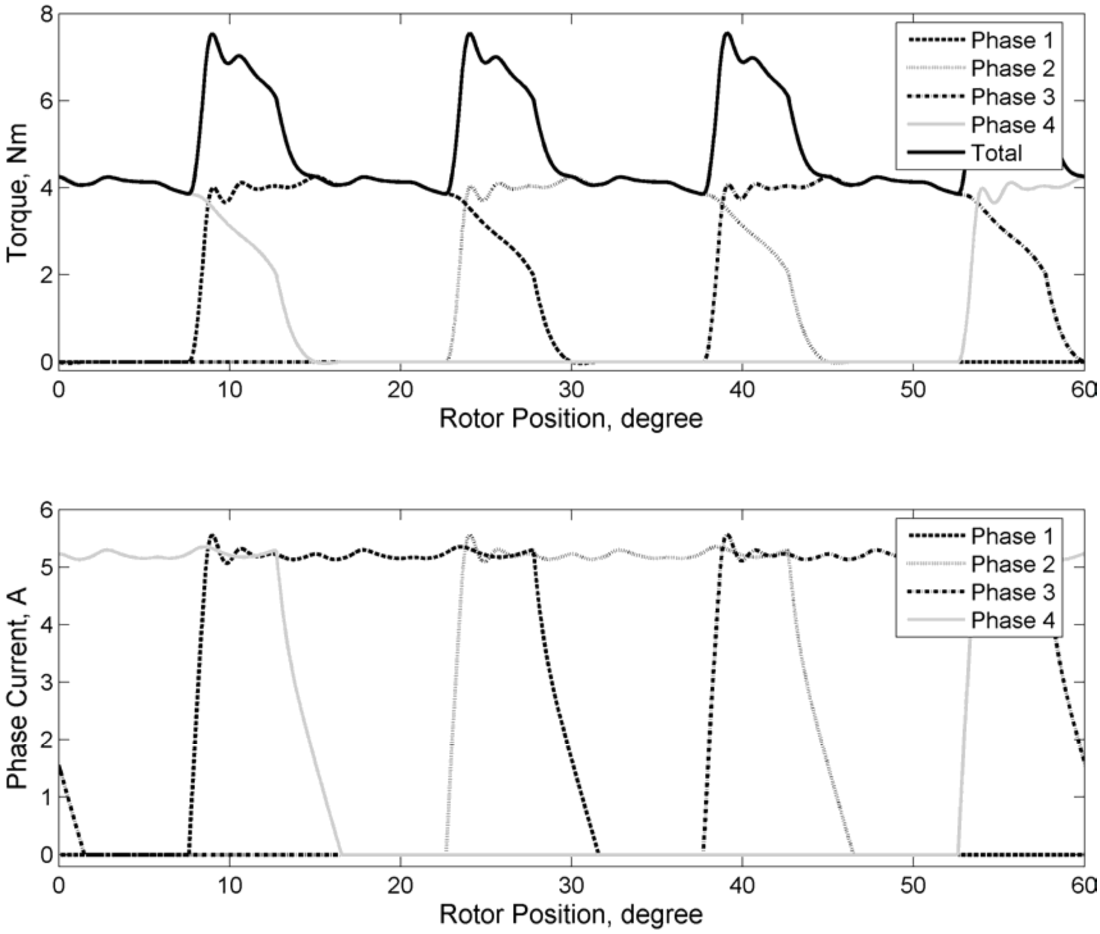

Fig. 5.8 Torque and current waveforms in motoring under constant current control

As for the generating mode, Fig. 5.9 illustrates the torque and current waveforms of the SRM at 4 Nm, 230 RPM. The torque output contains relatively less high frequency harmonics.

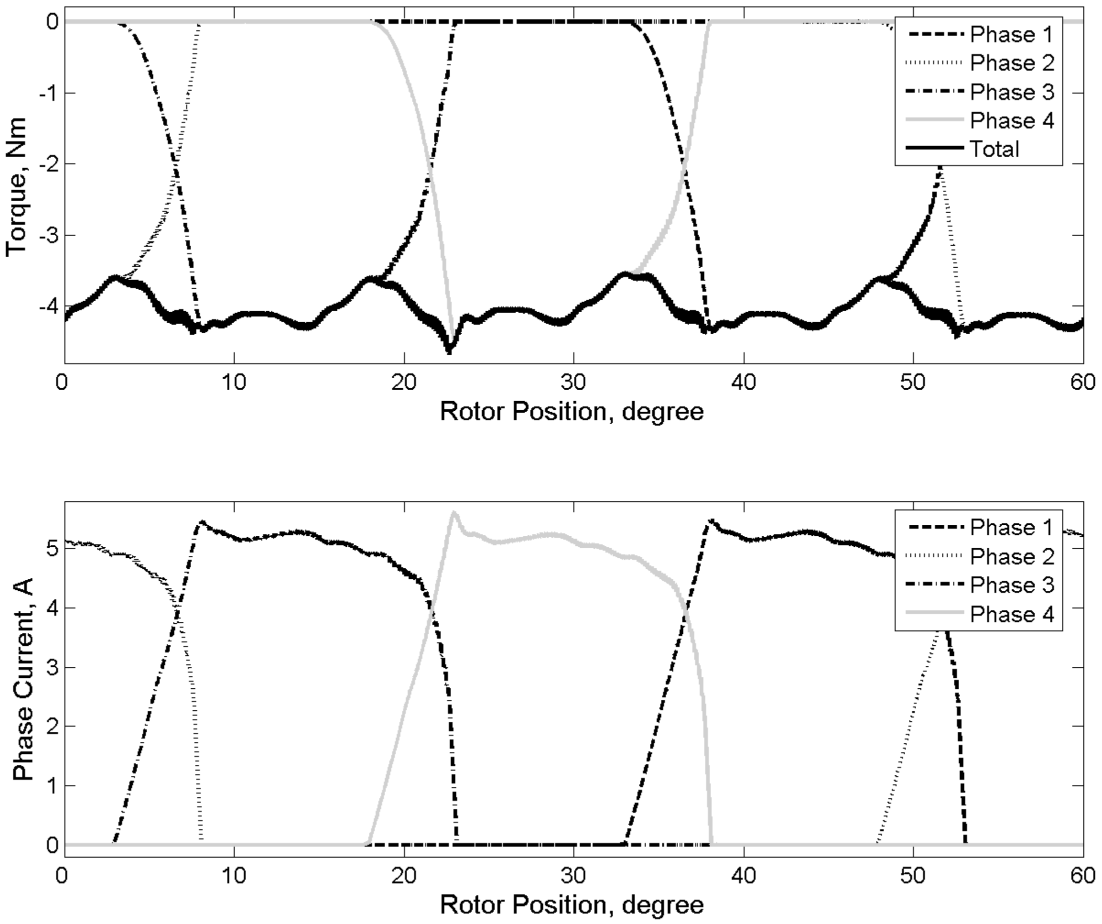

Fig. 5.9 Torque and current waveforms in generating under co-energy control

5.4.2 Experiment

The proposed scheme is verified experimentally as described below. The digital controller is realised with a dSpace 1104 R&D Controller Board. A sensor board is used to sense and process the voltage and current signals. A power converter outputs PWM voltages to the SRM windings. A motor-generator set supplies the DC-link voltage of the power drive. A separately excited DC machine acts as a load machine/prime mover. Between the DC machine and SRM, a torque transducer, Burster 8651-5020, is used for dynamic torque measurement.

The experimental torque and phase current waveforms of the SRM under co-energy control for an output of 4 Nm at 230 RPM are given in Fig. 5.10. The simulation waveforms for the same condition are also plotted on the same figure for comparison. The currents waveforms are similar and the average torques are alike. Because the rotor inertia of the SRM filters out a portion of the torque ripple output, the torque output of the experimental setup is smoother than that predicted by simulation.

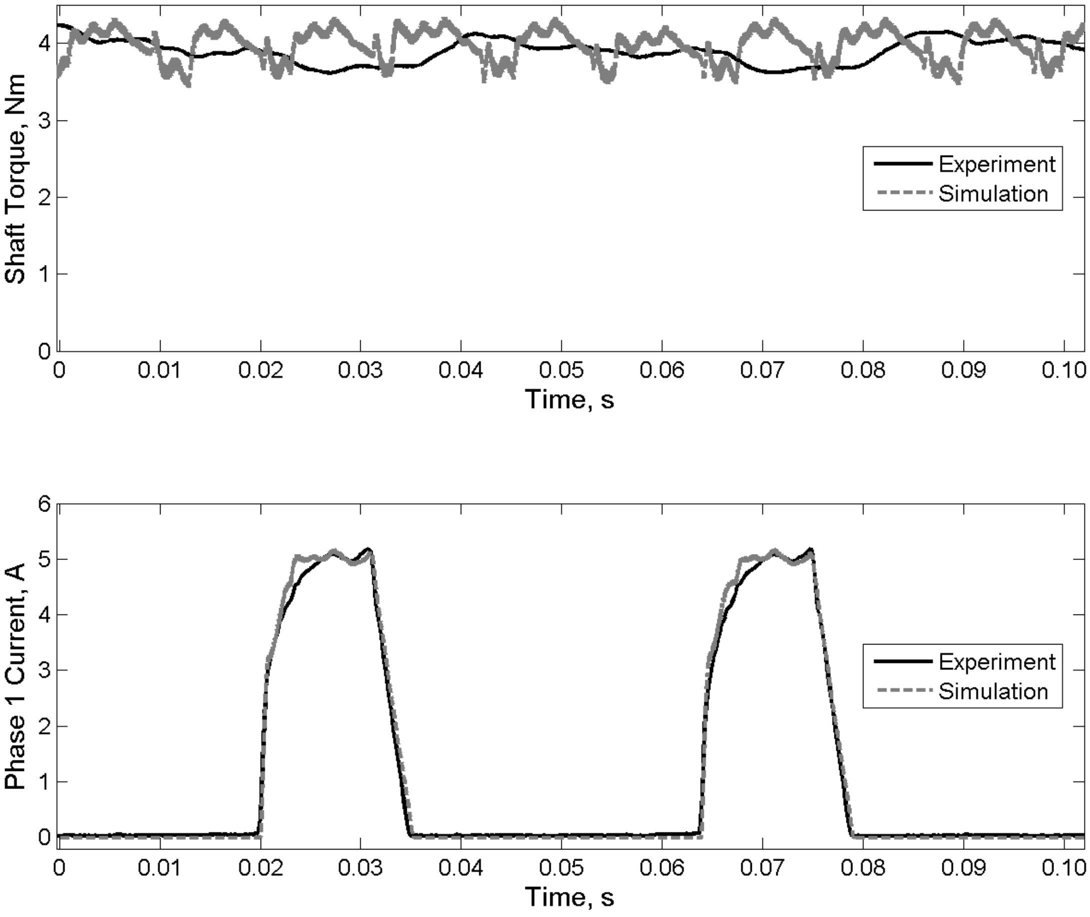

Fig. 5.10 Shaft torque and phase 1 current under co-energy control in motoring

To compare the control schemes, Fig. 5.11 displays the experimental waveforms of constant current control, which show high frequency torque ripples, especially during phase commutation. The co-energy control scheme, as depicted in Fig. 5.10, outputs a relatively smooth shaft torque.

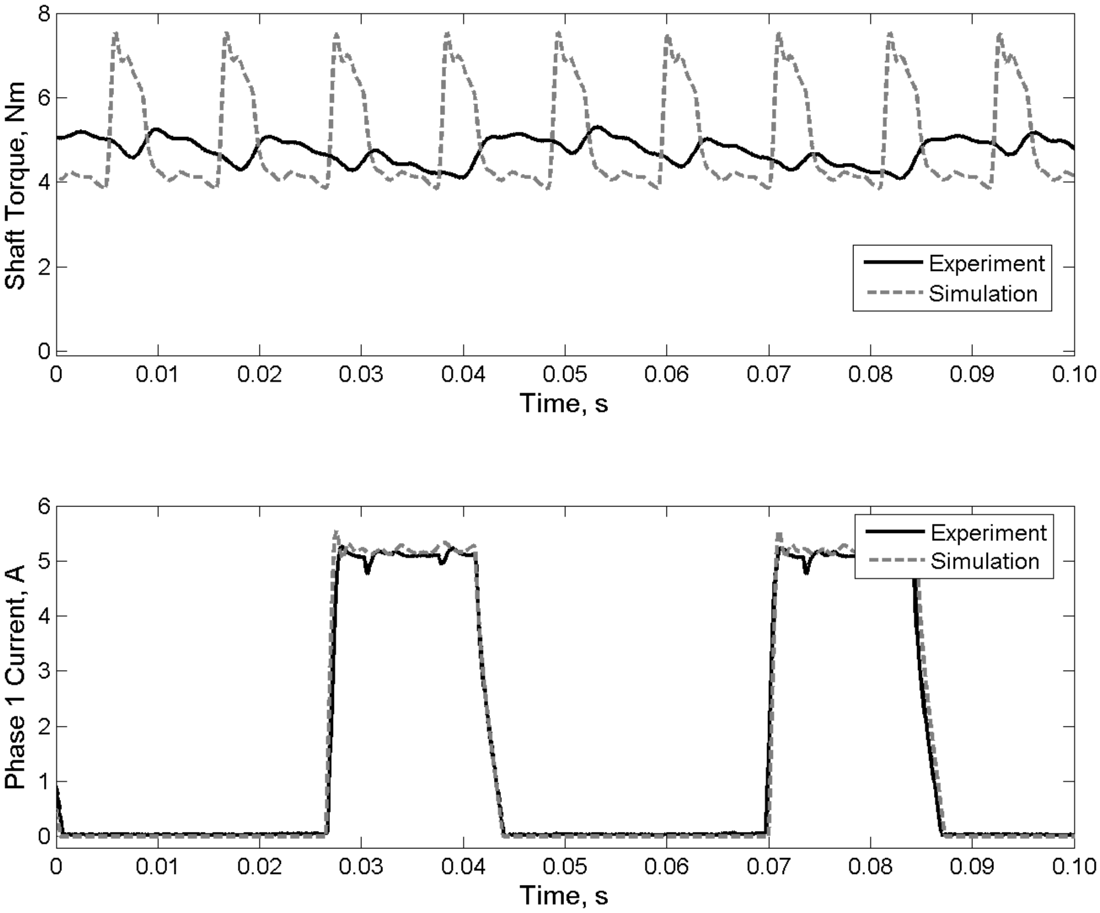

Fig. 5.11 Shaft torque and phase 1 current under constant current control in motoring

As for co-energy control in the generating mode of operation, Fig. 5.12 depicts the waveforms. The simulation waveforms are also draw on the figure for comparison. The torque output is as smooth as that of the motoring mode. It should be noted that the waveforms for constant current control in the generating mode is similar to those in motoring mode and are not repeated here.

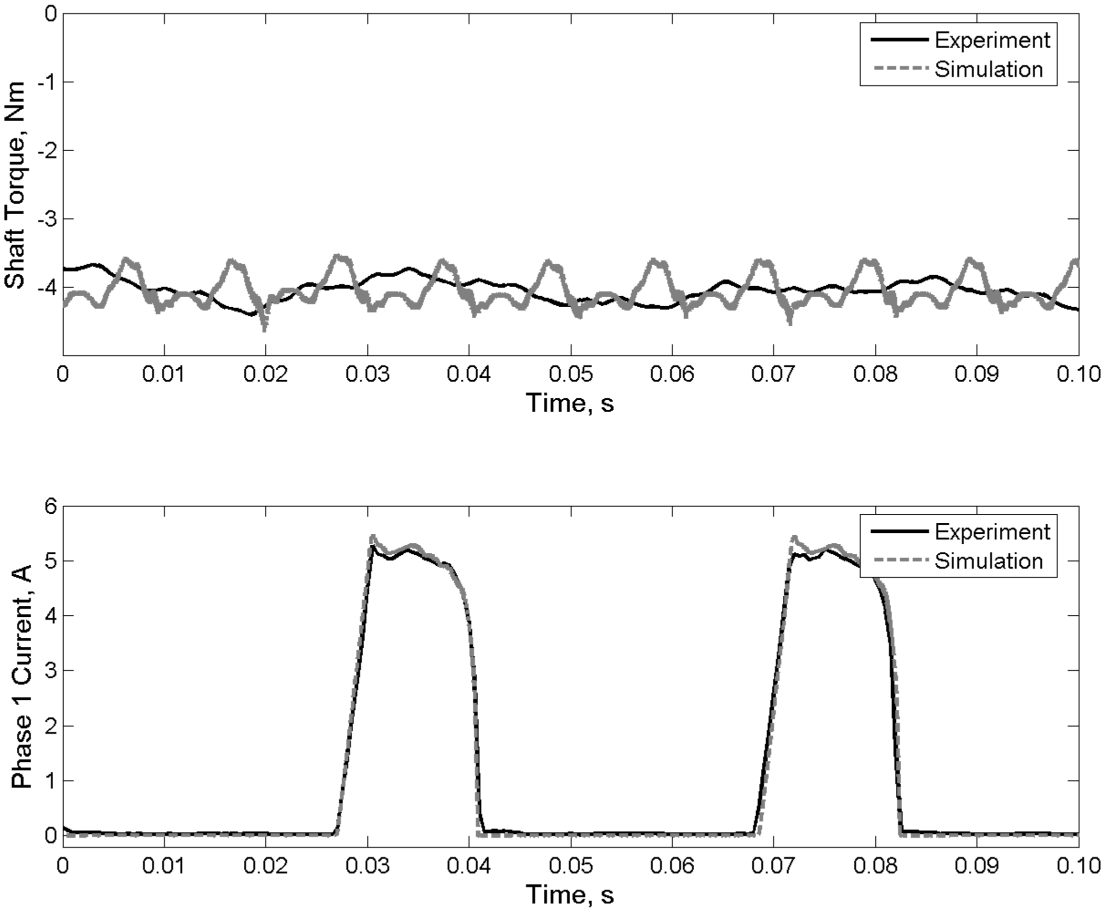

Fig. 5.12 Shaft torque and phase 1 current under co-energy control in generating

The data of the torque ripples are further processed with discrete Fourier transform in the analysis in frequency domain. The RMS values of the frequency components, expressed as the percentage of the average torque outputs, are listed in Table 5.1. As the fundamental of torque ripple of an 8/6 SRM running at 230 RPM is 92 Hz, only the 92 Hz component and its multiples are shown. The proposed algorithm reduces the fundamental torque ripple by 60%, in both motoring and generating modes of operation. For higher harmonic components, the improvements are more significant. The second harmonic is attenuated by over 80%, while the third harmonic is reduced by 70%. In fact, the overall torque ripple is cut by 70% for motoring and 64% for generating.

Table 5.1 Frequency components of output torques

Frequency component (Hz)	92	184	276
Constant current (% of 0 Hz component)	3.60	2.08	1.49
Co-energy control in motoring mode (% of 0 Hz component)	1.28	0.20	0.20
Co-energy control in generating mode (% of 0 Hz component)	1.47	0.38	0.45

It demonstrates that the proposed torque control scheme is effective to control the torque and reduce torque ripple in both motoring and generating modes of operation, in contrast to the traditional constant current control method.

5.5 Summary

This chapter develops a four-quadrant instantaneous torque control scheme for SRM. With the use of the inductance profile obtained at low current and the machine terminal quantities, the co-energy of each phase is estimated online. The normalised co-energy profile for unity phase torque is also calculated based on the inductance profile. A torque sharing function is then developed to coordinate the torque contribution of the active phases so as to deliver a constant output torque. The co-energy controller is designed with the concept of internal mode control. The implementation of the controller is a simple PI controller with a variable gain scheduled according to the current. The operation limits of the scheme are also examined. Computer simulation and experiment results are used to validate the operation of the scheme under both motoring and generating modes. It has been found that the proposed co-energy control has significant improvement in torque ripple.

The proposed methodology is suitable for applications requiring four-quadrant performance, such as in EV, traction, and robotics. The realisation of the scheme can be accomplished with standard motion control DSP, as no complex control algorithm and sensors are required.

6 Rotor Position Control using 2-Degree of Freedom Controller

6.1 Introduction

Control of rotor position of SRM is essential for the development of position servo drive. As depicted in Chapter 1, although SRM possesses qualities required for servo drive, most researchers concentrates on speed control and only few position control algorithms are reported.

In this chapter, an algorithm to control the rotor position of SRM is introduced, as a further extension of Chapter 5. By means of co-energy control, the electromagnetic torque of each phase is controlled. The co-energy command is derived from the magnetic characteristics at low-current, as the relationship between co-energy and torque is linear, extending from unsaturated to saturated regions. A co-energy estimator, derived from the magnetic data at low current, and the aligned position, is used for online co-energy feedback. Moreover, the effects of magnetic saturation are also taken into account in the co-energy estimation. In fact, the co-energy control and estimation only require a one-dimensional look-up table, instead of two-dimensional tables commonly used by researchers. On top of the torque control, a position loop is implemented. The co-energy and position controllers are designed based on a two-degree of freedom internal model control, which can effectively and timely reject disturbances. Thus, no feedforward control is required. The tuning problems for the controllers are reduced into the selection of the desired response time constants.

6.2 Principle of operation

As suggested in Chapter 5, to control the torque output of each phase, the co-energy is regulated in accordance to the product of the phase torque command T^* and co-energy profile:

$$W_c^* = W_{c\,norm}\left(\theta_{ph}\right)T^* \tag{6.37}$$

For a smooth commutation, a torque sharing function (TSF) TSF(θ_{ph}) is applied to translate the torque command T_{cmd} into the torque command of the phases:

$$T^* = \left|T_{cmd}\right| f\left(\theta_{ph}\right) \tag{6.38}$$

$$f\left(\theta_{ph}\right) = \begin{cases} \dfrac{2\left(\theta_{ph}-\theta_1\right)^2}{\left(\theta_2-\theta_{phase}-\theta_1\right)^2} & \theta_1 \le \theta_{ph} < \dfrac{\theta_1+\theta_2-\theta_{phase}}{2} \\ 1-\dfrac{2\left(\theta_{ph}-\theta_2+\theta_{phase}\right)^2}{\left(\theta_2-\theta_{phase}-\theta_1\right)^2} & \dfrac{\theta_1+\theta_2-\theta_{phase}}{2} \le \theta_{ph} < \theta_2-\theta_{phase} \\ 1 & \theta_2-\theta_{phase} \le \theta_{ph} < \theta_1+\theta_{phase} \\ 1-\dfrac{2\left(\theta_{ph}-\theta_1-\theta_{phase}\right)^2}{\left(\theta_2-\theta_{phase}-\theta_1\right)^2} & \theta_1+\theta_{phase} \le \theta_{ph} < \dfrac{\theta_1+\theta_2+\theta_{phase}}{2} \\ \dfrac{2\left(\theta_{ph}-\theta_2\right)^2}{\left(\theta_2-\theta_{phase}-\theta_1\right)^2} & \dfrac{\theta_1+\theta_2+\theta_{phase}}{2} \le \theta_{ph} < \theta_2 \end{cases} \tag{6.39}$$

where θ_{phase} is the phase shift among the phases. The phase is energised between θ_1 and θ_2. The simulated torque output of an 8/6 SRM for different torque commands at different rotor positions are depicted in Fig. 6.1.

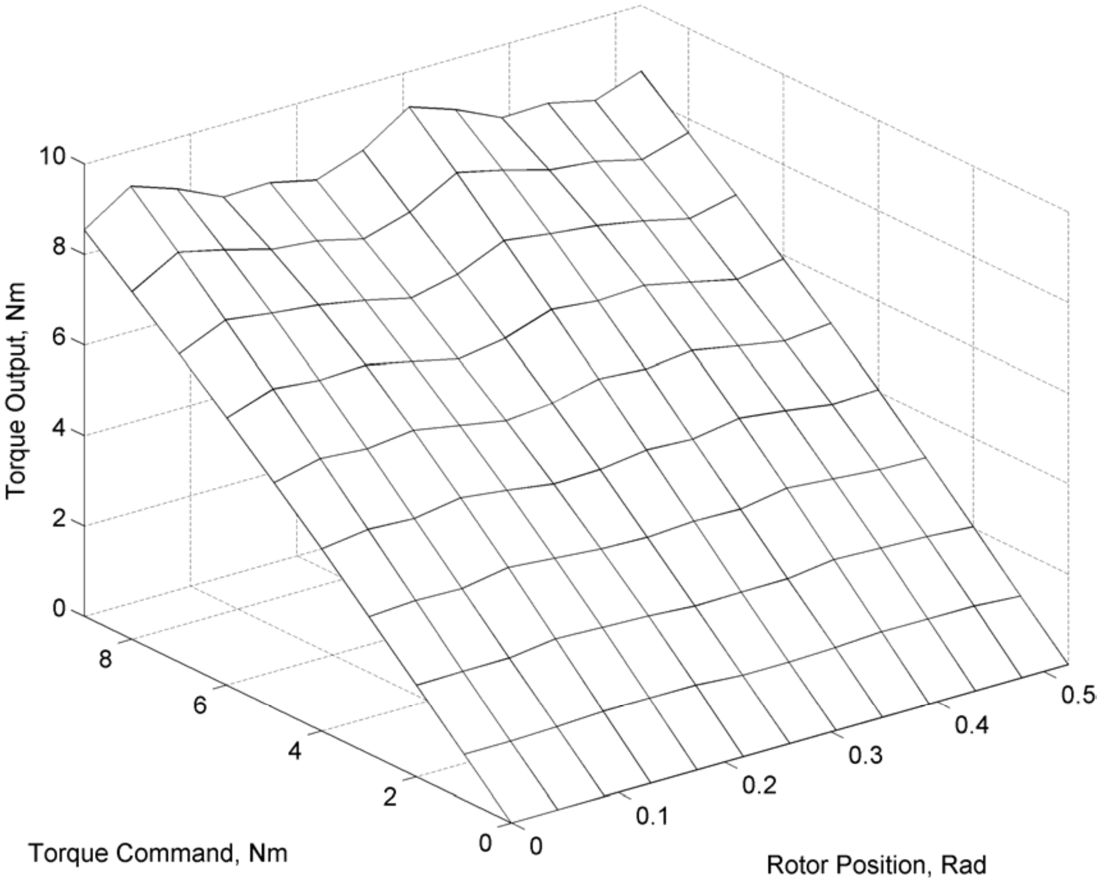

Fig. 6.1 Relationship between torque command, torque output and rotor position

It can be seen that the torque output essentially follows the torque command, even though there are small torque ripples at different rotor positions. The ripples, especially near 0.15 and 0.4 rad, are because of the coarse resolution of the co-energy profile and the use of numerical differentiation during calculation of the co-energy profile, as explained in Section 4.4.1. For negative torque command, the relative rotor position is mirrored along the unaligned position.

The mechanical dynamics of the system is expressed as:

$$T_e = J\frac{d^2\theta}{dt^2} + B\frac{d\theta}{dt} + T_{Load} \tag{6.40}$$

where; J is the moment of inertia; θ is the mechanical rotor position; B is the friction constant and T_{Load} is the load torque. Because the mechanical time constant is in general longer than the electrical time constant, and the torque output is close to the torque command under co-energy control. The electrical torque is, therefore, assumed to be equal to the torque command. Equation (6.40) becomes:

$$T_{cmd} = J\frac{d^2\theta}{dt^2} + B\frac{d\theta}{dt} + T_{Load} \tag{6.41}$$

6.3 Controller design

The structure of the position control system is shown in Fig. 6.2.

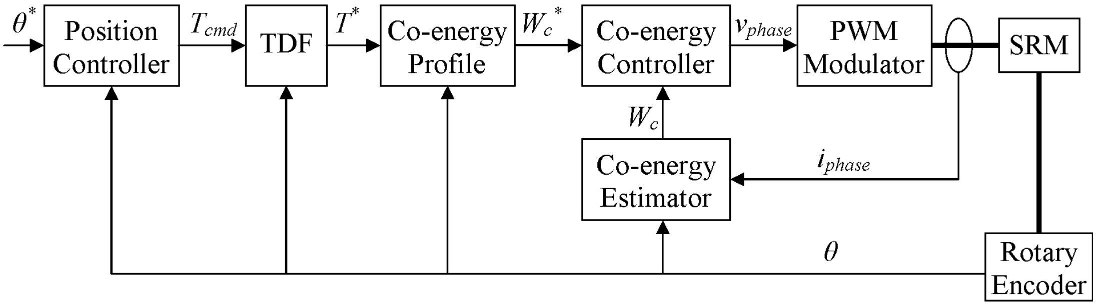

Fig. 6.2 Structure of the position control system

The position controller receives the position command and rotor positions from the rotary encoder, and outputs a torque command. The torque command is then resolved into the phase torque commands according to the torque distribution function. The phase torque commands are converted into co-energy commands in accordance to the co-energy profile. The co-energy controller regulates the co-energies, as estimated by the co-energy estimator with reference to the commands, and outputs the required phase voltages. The voltages fed to the SRM are modulated by constant-frequency PWM.

6.3.1 Co-energy estimator

The flux linkage of SRM is expressed by a second-order Fourier series [83]:

$$\lambda = \begin{bmatrix}\lambda_a & \lambda_u\end{bmatrix}\begin{bmatrix}0 & w & 1\\ 1 & 1-w & 0\end{bmatrix}\left(\begin{bmatrix}1 & 1 & 1\\ 1 & \cos\left(\frac{\pi}{2}\right) & \cos(\pi)\\ 1 & \cos(\pi) & \cos(2\pi)\end{bmatrix}^{-1}\right)^{T}\begin{bmatrix}1\\ \cos(N_r\theta_{ph})\\ \cos(2N_r\theta_{ph})\end{bmatrix} \tag{6.42}$$

where; λ_a and λ_u are the aligned and unaligned flux linkages, respectively; w is a weighting factor; N_r is the number of rotor poles. Expanding the terms:

$$\lambda = \begin{bmatrix}\lambda_a & \lambda_u\end{bmatrix}\vec{C}\begin{bmatrix}1\\ \cos(N_r\theta_{ph})\\ \cos(2N_r\theta_{ph})\end{bmatrix} \tag{6.43}$$

where

$$\vec{C} = \begin{bmatrix}\frac{1+2w}{4} & -\frac{1}{2} & \frac{1-2w}{4}\\ \frac{1+2(1-w)}{4} & \frac{1}{2} & \frac{1-2(1-w)}{4}\end{bmatrix} \tag{6.44}$$

By experimentally measuring the flux linkages at low current at different rotor positions, a vector of flux linkages, their corresponding rotor positions, as well as their aligned and unaligned flux linkages, are obtained. Using a curve-fitting technique, the weighting factor for the SRM can be calculated off-line.

Regardless whether there is magnetic saturation or not, the flux linkage at the aligned position is modelled [84] as:

$$\lambda_a\left(i_{phase}\right)=d\left(ai_{phase}+b-\sqrt{b^2+ci_{phase}+i_{phase}^2}\right) \tag{6.45}$$

where *a*, *b*, *c*, and *d* are constants specific to the machine. Using laboratory measurement of flux linkages at the aligned position for different currents, the constants can be obtained with curve fitting. Substituting (6.45) into (1.2) and evaluating the integral, the co-energy at the aligned position, $W_{c\,a}$, is:

$$W_{c\,a}=d\left(\frac{ai_{phase}^2}{2}+bi_{phase}-\frac{k_1k_2}{2}-\left(\frac{b^2}{2}-\frac{c^2}{8}\right)\ln\left(k_1+k_2\right)+k_3\right) \tag{6.46}$$

where

$$\begin{aligned}
k_1&=i_{phase}+\frac{c}{2}\\
k_2&=\sqrt{b^2+ci_{phase}+i_{phase}^2}\\
k_3&=\frac{bc}{4}+\left(\frac{b^2}{2}-\frac{c^2}{8}\right)\ln\left(\frac{c}{2}+b\right)
\end{aligned} \tag{6.47}$$

The co-energy at the unaligned position does not require any consideration with respect to saturation because of the presence of relatively long airgaps along the flux path and the co-energy at the unaligned position, $W_{c\,u}$, can be found simply as:

$$W_{c\,u}=\frac{1}{2}L_u i_{phase}^2 \tag{6.48}$$

where L_u is the inductance at the unaligned position. The co-energy as derived from (6.43) becomes:

$$W_c = \begin{bmatrix} W_{ca} & W_{cu} \end{bmatrix} \vec{C} \begin{bmatrix} 1 \\ \cos(N_r \theta_{ph}) \\ \cos(2N_r \theta_{ph}) \end{bmatrix} \tag{6.49}$$

For on-line co-energy estimation, only equations (6.46), (6.48), and (6.49) are evaluated, and these are not computationally intensive.

6.3.2 Two-degree of freedom internal model control

The principles of two-degree of freedom internal model control (2DF IMC) are applied to design the controllers for co-energy and position regulations. 2DF IMC is a robust model-based control algorithm for processes which can be represented by approximated mathematical models [82]. Apart from the required response time constants, all parameters of the 2DF IMC are derived from the models. The general structure of 2DF IMC is shown in Fig. 6.3.

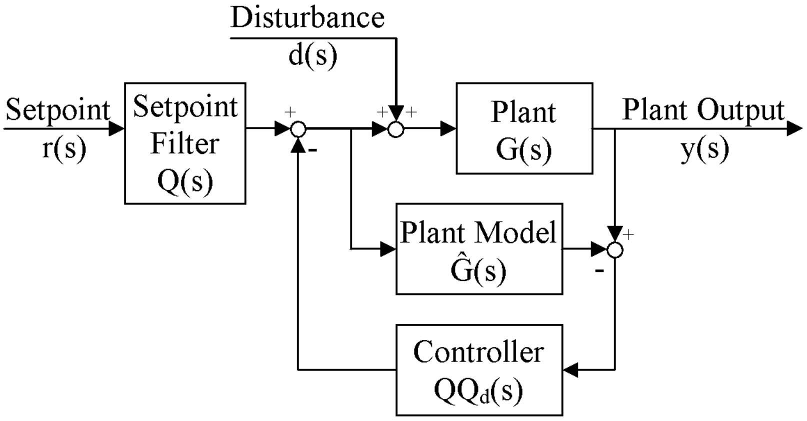

Fig. 6.3 General structure of 2DF IMC

The setpoint $r(s)$ is shaped by the setpoint filter $Q(s)$, and then fed to the process plant $G(s)$ and an internal plant model $\hat{G}(s)$. The difference between the plant and plant model outputs, because of model mismatch and the disturbance $d(s)$, is fed back via the controller $QQ_d(s)$.

Assume the plant model can be factorised into:

$$\hat{G}(s) = \hat{G}_s(s)\hat{G}_u(s) \tag{6.50}$$

where $\hat{G}_s(s)$ is the portion that is stable and realisable after inversion, $\hat{G}_u(s)$ is the unstable fraction. The setpoint filter is designed as:

$$Q(s) = \hat{G}_s^{-1}(s)F(s) \tag{6.51}$$

where $F(s)$ is a low-pass filter:

$$F(s) = \frac{1}{(\varepsilon s + 1)^r} \tag{6.52}$$

where ε is the setpoint filter time constant, r is the relative order of $\hat{G}_s(s)$ to ensure $Q(s)$ is stable. If the plant model is an exact match of the plant, the plant output converges to the setpoint, with a time constant equal to the filter time constant. For implementation with a digital controller, the closed-loop time constant is set to at least 30 times of the sampling period [80]:

$$\varepsilon \geq \frac{30}{2\pi F_s} \tag{6.53}$$

where F_s is the sampling frequency in Hz.

To analysis the stability of the system from the setpoint to plant output, the signal path is identified as the series combination of the setpoint filter and plant. As the setpoint filter is designed to cancel the poles and zeros of the plant and add a low-pass filter, the system is stable if all the poles of the plant are stable. Even if there is a model-mismatch, the stability is maintained by the matching of the numbers of poles and zeros. For the applications of 2DF IMC in this chapter, as the plants for co-energy and position control contain only stable poles, the control systems are stable.

As for the design of the controller $QQ_d(s)$, the objective is to reject the influence of the disturbance. The transfer function from the disturbance to plant output is:

$$\frac{y(s)}{d(s)} = \frac{\left(1-\hat{G}(s)QQ_d(s)\right)G(s)}{1+\left(G(s)-\hat{G}(s)\right)QQ_d(s)} \tag{6.54}$$

For simplicity, only a case without model-mismatch is considered:

$$\frac{y(s)}{d(s)} = \left(1-\hat{G}(s)\,QQ_d(s)\right)G(s) \tag{6.55}$$

The zeros of $(1-\hat{G}(s)QQ_d(s))$ should cancel the poles of $G(s)$ for fast disturbance rejection. Therefore, the controller $QQ_d(s)$ is designed as:

$$QQ_d(s) = \frac{\hat{G}_s^{-1}(s)}{\left(\varepsilon_r s+1\right)^{r+n}}\left(1+\sum_{i=1}^{n}\alpha_i s^i\right) \tag{6.56}$$

where ε_r is the controller filter time constant, n is the number of poles of the process plant. The values of α_i are chosen to meet the following conditions:

$$\left(1-\hat{G}(s)QQ_d(s)\right)\Big|_{s=p_i}=0 \tag{6.57}$$

where p_i is the i^{th} pole of the plant. For k^{th} order repeated poles or poles at the origin, the first to (k-1)th order derivatives of (6.57) are also set to zero:

$$\frac{d^n}{ds^n}\left(\hat{G}(s)QQ_d(s)\right)\Big|_{s=p_i}=0 \text{ for } n=1...(k\text{-}1) \tag{6.58}$$

In general, the choice of the time constant ε_r is dependent on the required settling time under step disturbance input. The sampling time requirement (6.53) is also applicable to ε_r.

For the stability analysis of the system against disturbance, the poles of the closed system (6.55) are identified. The poles of the plant are cancelled by the zeros of (1-$\hat{G}(s)QQ_d(s)$), while the poles of $\hat{G}(s)QQ_d(s)$ are -1/filter time constant. Hence, all the poles of (6.55) and the closed system are stable.

To reduce the computational burden for online application of 2DF IMC, a compact form of the controller as shown in Fig. 6.4 is used.

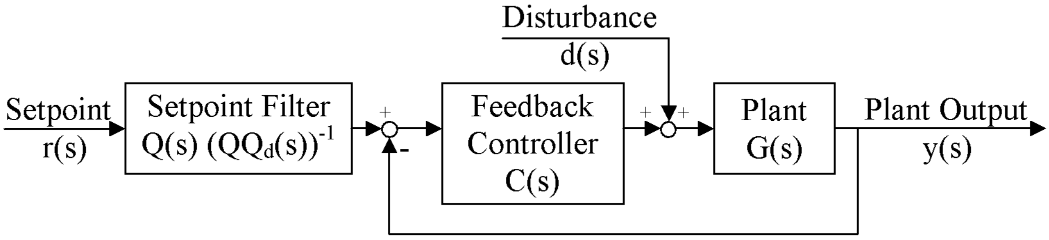

Fig. 6.4 Compact form of 2DF IMC

The feedback controller is:

$$C(s) = \frac{QQ_d(s)}{1 - QQ_d(s)\hat{G}(s)} \tag{6.59}$$

After expanding the terms, it becomes:

$$C(s) = \frac{\hat{G}_s^{-1}(s)\left(1 + \sum_{i=1}^{n} \alpha_i s^i\right)}{(\varepsilon_r s + 1)^{r+n} - \hat{G}_u(s)\left(1 + \sum_{i=1}^{n} \alpha_i s^i\right)} \tag{6.60}$$

6.3.2.1 Co-energy controller

The transfer function from phase voltage to co-energy, as derived in Chapter 4, is:

$$G(s) = \frac{\Delta W_c}{\Delta v_{phase}} = \frac{k\, i_{phase}}{R/l + s} \tag{6.61}$$

The internal plant model for co-energy control is:

$$\hat{G}_e(s) = \frac{k i_{phase}}{R/l_m + s} \tag{6.62}$$

The subscript *e* denotes the model for an electrical system. The modelled ratio *k* is considered constant at unity and the modelled inductance l_m is fixed at the unsaturated aligned inductance for internal modelling. The setpoint filter $Q_e(s)$ is set according to (6.51):

$$Q_e(s) = \frac{R/l_m + s}{i_{ph}(\varepsilon_e s + 1)} \tag{6.63}$$

From (6.56), (6.57) and (6.62), the controller becomes:

$$QQ_{d\,e}(s) = \frac{(R/l_m + s)(\alpha_e s + 1)}{i_{ph}(\varepsilon_{r\,e} s + 1)^2} \tag{6.64}$$

where α_e sets the zero of (1- $\hat{G}_e(s)QQ_{d\,e}(s)$) to $-R/l_m$:

$$\alpha_e = -\varepsilon_{r\,e}^2 \frac{R}{l_m} + 2\varepsilon_{r\,e} \tag{6.65}$$

In cases with rapid changes of torque command, and hence fast changes in co-energy commands, the output voltage is highly saturated and the controller becomes unstable. To prevent this, a rate limiter is applied to limit the rate of change of the co-energy command. For a rate of change of co-energy $W^*_{c\,rate}$, the co-energy command in s-domain is:

$$W_c^* = \frac{W^*_{c\,rate}}{s^2} \tag{6.66}$$

The rate of change of co-energy output under 2DF IMC is:

$$W_c s = \frac{W^*_{c\,rate}}{(\varepsilon_e s + 1)s} \tag{6.67}$$

In time domain,

$$\frac{dW_c}{dt} = W^*_{c\,rate}\left(1 - e^{-\frac{t}{\varepsilon_e}}\right) \tag{6.68}$$

Consequently, the maximum rate of change of co-energy output is $W^*_{c\,rate}$. With a step input voltage V_{dc}, the approximated rate of change of current output is:

$$\frac{di_{ph}}{dt} \approx \frac{V_{dc}}{L} \tag{6.69}$$

From Chapter 4, the small signal relationship between phase current and co-energy is

$$\Delta W_c = L i_{phase} \Delta i_{phase} \tag{6.70}$$

The derivative of (6.70) is:

$$\frac{dW_c}{dt} = L i_{phase} \frac{di_{phase}}{dt} \tag{6.71}$$

From (6.69) and (6.71), the permissible rate of change of co-energy is:

$$\frac{dW_c}{dt} = V_{dc} i_{phase} \tag{6.72}$$

Therefore, the rate limiter of the co-energy command is set to:

$$W^*_{c\,rate} = V_{dc} i_{phase} \tag{6.73}$$

It should be noted that the rate limiter is by-passed when the phase current is small, in order to allow the output of the rate limiter to start from zero. If the parameters of the internal model of the controller deviate from that of the process plant, the co-energy output is different from (6.67) and (6.68). The controller output is then saturated slightly, but the controller, in general, can tolerate slight saturations and remains stable.

6.3.2.2 Position controller

As derived from (6.41), with the load torque treated as disturbances, the transfer function of the mechanical system in s-domain is:

$$\frac{\theta(s)}{T_{cmd}(s)} = \frac{{}^{1}\!/_{J}}{s + {}^{B}\!/_{J}} \frac{1}{s} \tag{6.74}$$

The internal plant model $\hat{G}_m(s)$ is:

$$\hat{G}_m(s) = \frac{{}^{1}\!/_{J}}{s + {}^{B}\!/_{J}} \frac{1}{s} \tag{6.75}$$

Accordingly, the setpoint filter $Q_m(s)$ becomes:

$$Q_m(s) = \frac{J\left(s + {}^{B}\!/_{J}\right)s}{(\varepsilon_m s + 1)^2} \tag{6.76}$$

The controller is then set as:

$$QQ_{d\,m}(s) = \frac{J\left(s + {}^{B}\!/_{J}\right)s}{(\varepsilon_{r\,m} s + 1)^4}\left(\alpha_{2\,m} s^2 + \alpha_{1\,m} s + 1\right) \tag{6.77}$$

where $\alpha_{1\,m}$ and $\alpha_{2\,m}$ are designed to place the zeros of (1- $\hat{G}_m(s) QQ_{d\,m}(s)$) at 0 and $-B/J$:

$$\alpha_{1m} = 4\varepsilon_{r\,m} \tag{6.78}$$

$$\alpha_{2\,m} = \varepsilon_{r\,m}^4 \left(\frac{B}{J}\right)^2 - 4\varepsilon_{r\,m}^3 \frac{B}{J} + 6\varepsilon_{r\,m}^2 \tag{6.79}$$

As with the co-energy controller, a rate limiter on position command is required to avoid severe saturation. For the rate of change of position command θ^*_{rate}, the position output is:

$$\theta = \frac{\theta^*_{rate}}{(\varepsilon_m + 1)^2 s^2} \tag{6.80}$$

The required torque is:

$$T_{cmd}(s) = \frac{\theta^*_{rate} J \left(s + B/J\right)}{(\varepsilon_m + 1)^2 s} \tag{6.81}$$

In time domain, the torque is:

$$T_{cmd}(t) = \theta^*_{rate} \left(\frac{\left((J - \varepsilon_m B)t - B\varepsilon_m^2\right) e^{-\frac{t}{\varepsilon_m}}}{\varepsilon_m^2} + B \right) \tag{6.82}$$

The maximum torque T_{max} is found by solving (6.82) to give:

$$T_{\max} = \theta^*_{rate} \left(\frac{\left(\varepsilon_m J - B\varepsilon_m^2\right) e^{-\frac{J}{J - \varepsilon_m B}}}{\varepsilon_m^2} + B \right) \tag{6.83}$$

With the torque limit being constrained by the current rating of the machine, the maximum rate of change of the rate limiter can be set to θ^*_{rate} which is obtained from (6.83). In general, the smaller the time constant ε_m, the larger is the maximum rate of change of position command allowed. There is a trade-off between dynamics and the rate of change of command. For a step change in position command, the best response is achieved if the output of the rate limiter reaches the command when the torque output is at its maximum. It, however, requires *a priori* knowledge of the position command, which is generally not available. Instead, one should set the time constant in accordance to the desired dynamic response and check whether the maximum rate of change of command is satisfactory.

6.4 Results

6.4.1 Simulation

The proposed algorithm is simulated in Matlab/SimPowerSystems as proposed in Chapter 2. Non-linear magnetic data based on a 4-phase 8/6 SRM is used. For the rotor position feedback, a 1000 count/rev rotary encoder is assumed. The sampling frequencies of the co-energy and position loops are 10 kHz and 500 Hz, respectively. The setpoint and controller filter time constants for co-energy control are 500 μs and 1 ms respectively. For the position controller, both time constants are set to 100 ms. The detailed machine and controller parameters are given in Table 6.1 and Table 6.2.

Table 6.1 Machine parameters

Machine rated voltage	270 VDC
Machine rated power	2.2 kW
Machine rated speed	1500 RPM
Number of phase	4
Number of stator poles	8
Number of rotor poles	6
Inductance at aligned position	141.2 mH
Inductance at unaligned position	18.9 mH
Winding resistance	1.2 Ω
Power drive voltage	150 VDC
Rotor inertia with load machine	0.07 kgm^2
Friction coefficient with load machine	0.012 Nms/rad
Static friction with load machine	0.2 Nm

Table 6.2 Controller parameters

(a) Co-energy controller

Sampling frequency	10 kHz
Setpoint filter time constant ε_e	500 μs
Controller filter time constant $\varepsilon_{r\,e}$	1 ms

(b) Position controller

Sampling frequency	500 Hz
Setpoint filter time constant ε_m	100 ms
Controller filter time constant $\varepsilon_{r\,m}$	100 ms

The torque and position with a step change of position command from 0° to 100° are shown in Fig. 6.5. It can be seen that the rotor position can track the command, with a converging time constant of about 110 ms, which is close to the specified value 100 ms.

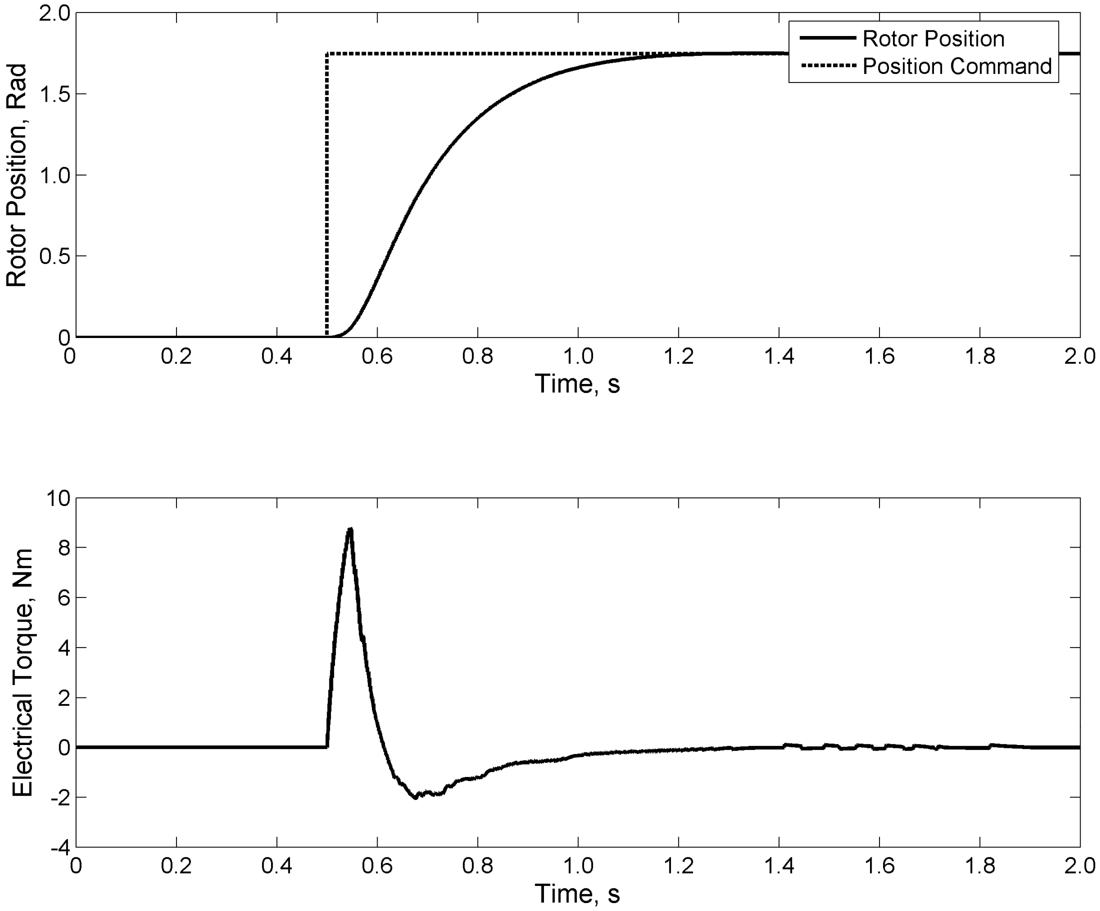

Fig. 6.5 Rotor position and torque output for a step position command

Even though the peak torque extents to the saturating region of the SRM after the step change of the position command, and the phase inductance varies non-linearly with the rotor position, the controllers are capable to control the rotor position as designed.

To simulate the disturbance response, a load torque of 1.6 Nm is applied at the time 0.5 s while the position command is kept unchanged at 0°. The responses are shown in Fig. 6.6. It can be seen that the controller can reject the effect of the disturbance within a short period of time.

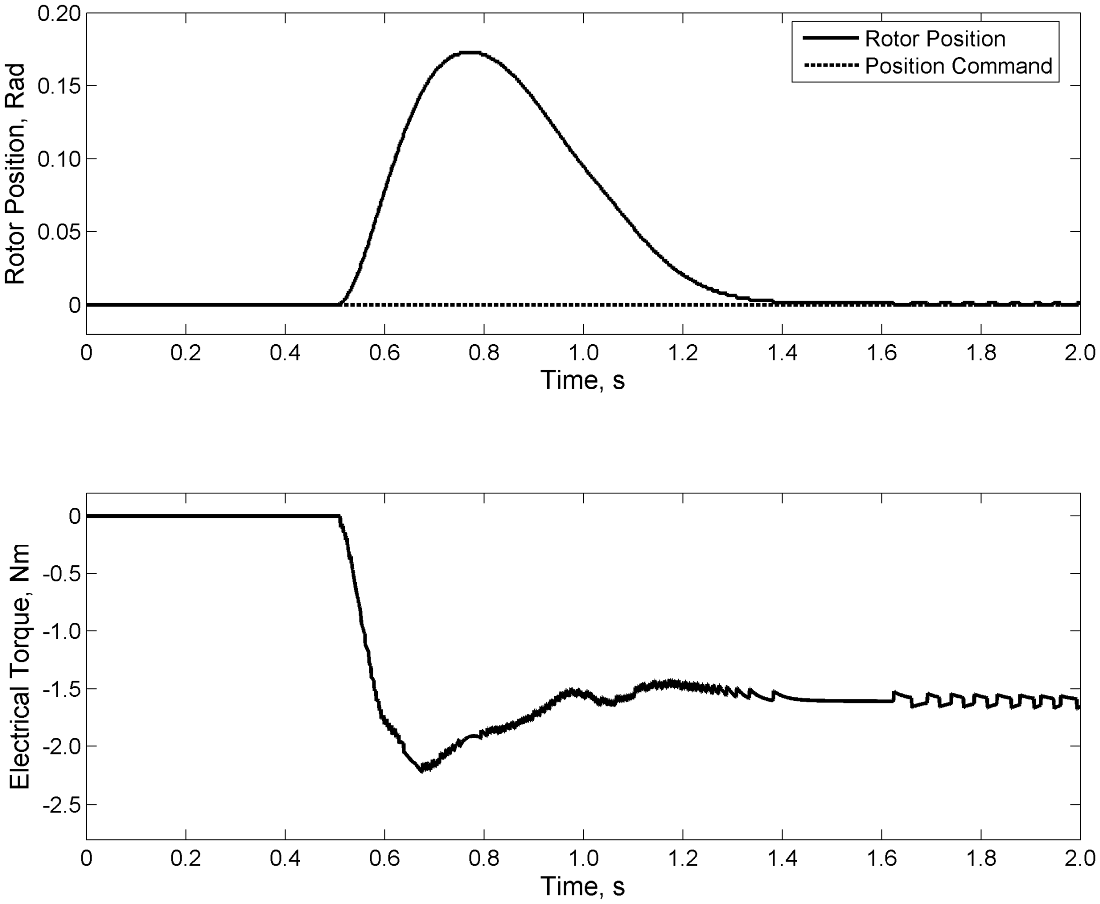

Fig. 6.6 Rotor position and torque output when a load torque is applied at 0.5 s

To demonstrate the robustness of the controller against model mismatch, the position step responses, with the modelled moment of inertia setting of the controller adjusted mathematically to 50% and 150% of the machine value, respectively, are simulated and shown in Fig. 6.7. Although there is a slight overshoot and the settling time increases as the modelled moment of inertia deviates from the original value, the system can stably converge to the command values. It is because, with the use of IMC, the numbers of poles and zeros are matched as mentioned in Section 6.3.2.

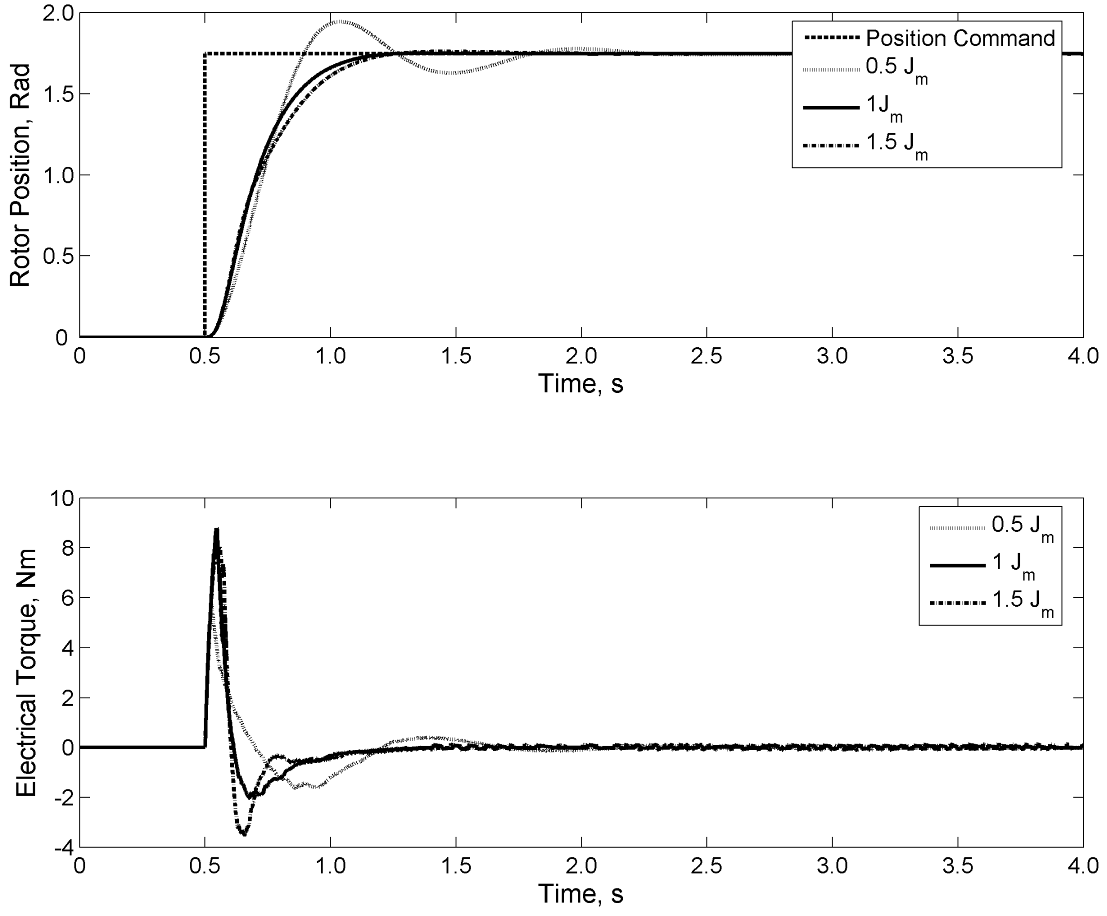

Fig. 6.7 Rotor positions and torque outputs with different modelled inertia J_m

6.4.2 Experiment

An experimental setup is used to validate the algorithm in an environment which is broadly similar to those stipulated for the simulation study. A dSpace 1104 R&D board implements the digital controller. The software code is generated by Real-Time Workshop under Matlab/Simulink and downloaded to the R&D board for real-time operation. The power drive consists of four independent asymmetric half-bridges constructed with IGBTs and power diodes. A DC-machine is coupled to the SRM as the load machine.

Fig. 6.8 shows the waveforms with a step change in position command from about 100° to 200°. It can be seen that the rotor position can stably follow the position command. It should be noted that the speed signal, which is not used by the controllers, contains quantisation noise due to the discrete nature of the rotary encoder.

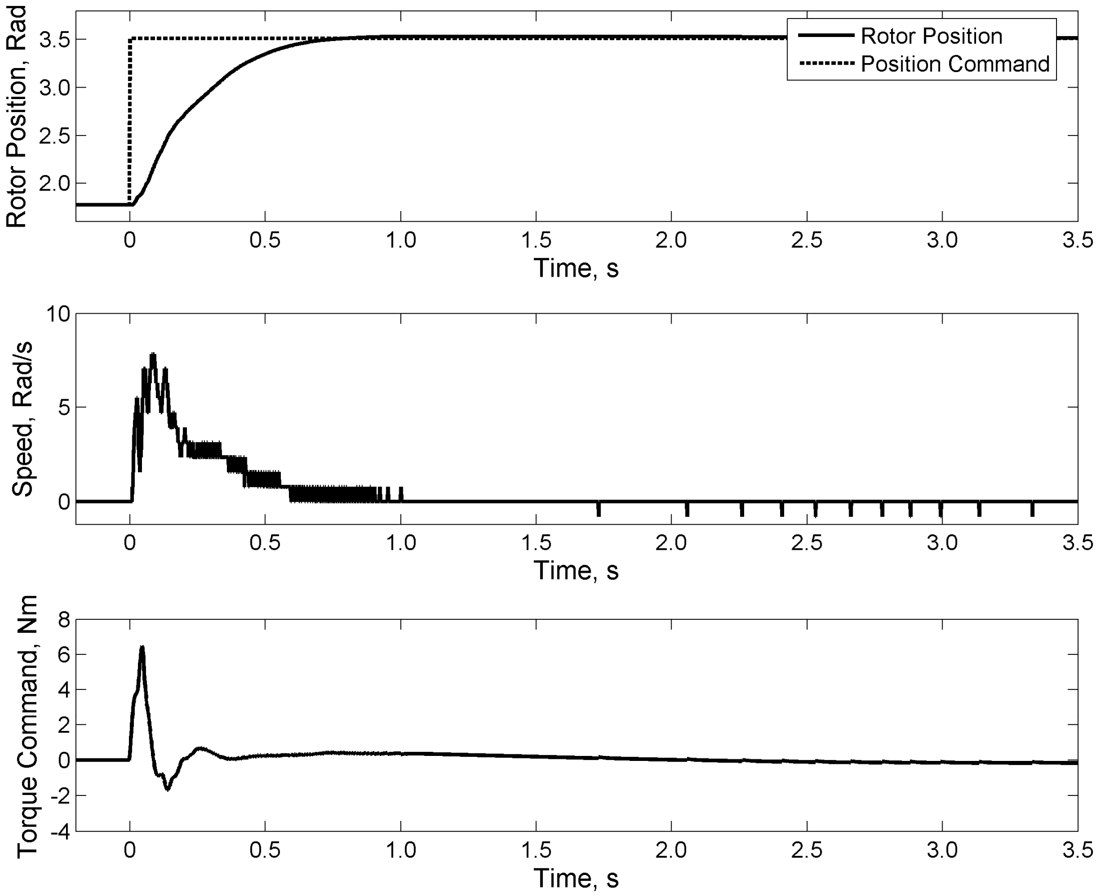

Fig. 6.8 Rotor position, speed and torque command with a step change in position command

The response to a change in disturbance is depicted in Fig. 6.9. When a load torque of 1.6 Nm is applied to the dynamometer at 0 s, the rotor position changes momentarily and is then restored to the commanded position. It demonstrates that the system has good dynamic responses with no steady-state error.

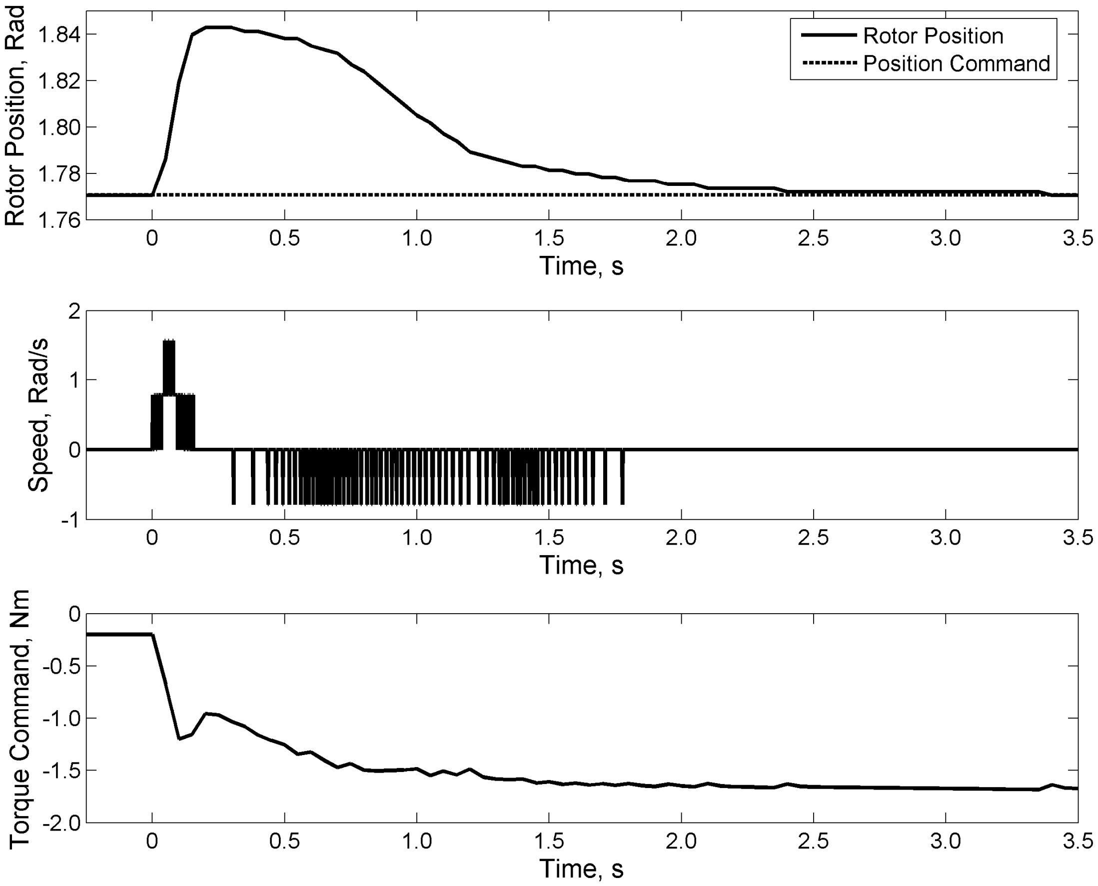

Fig. 6.9 Rotor position, speed and torque command when a load torque is applied at 0 s

It should be noted that the displacement of the rotor position of the system against disturbance in the experiment is smaller than that of the simulation shown in Fig. 6.6. When the load torque is increased by injecting current into the armature winding of the dynamometer, the winding inductance limits the rate of rise of the current and hence the load torque. In fact, the change of the load disturbance in the experiment is a slope instead of the ideal step change. Therefore, the controller has more time to react on the disturbance, before the rotor position is changed. In addition, the dead zone due to the mechanical couplings and the static torque of the dynamometer are not modelled in the simulation, which increase the settling time of the system near zero speed.

To test the robustness of the controller against parameter variations, the modelled moment of inertia of the controller is mathematically changed, in turn, to 50% and 150% of the original value. The rotor positions with a step position input are plotted in Fig. 6.10. Although the modelled parameters are significantly different from the actual values, the controller can nonetheless regulate the rotor positions to track the command.

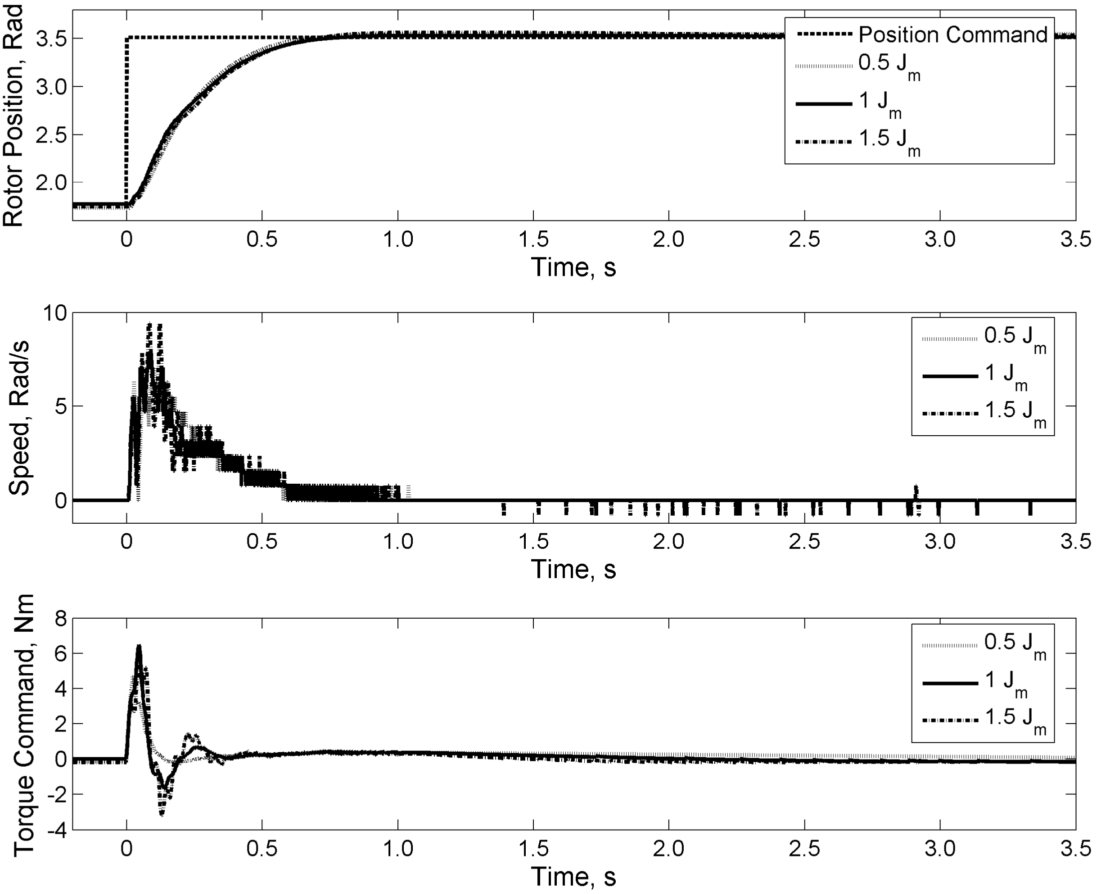

Fig. 6.10 Rotor positions, speeds and torque commands with different modelled moment of inertia J_m

6.5 Summary

This chapter presents an algorithm to control the rotor position of an SRM. By regulating the co-energy in accordance to a co-energy profile, which is derived from the low-current magnetic characteristics, the electromagnetic torque is controlled. An on-line co-energy estimator, based on the magnetic data at low-current and the aligned position, is developed to estimate the co-energy of each phase. The controllers of electrical and mechanical systems are designed using the approximated mathematical models of the machine and principles of two-degree of freedom internal model control. The only customised parameters are the time constants of the output responses. With the proposed methodology, the design process is greatly simplified. Simulation and experimental results confirm that the system can track the position command, even under external disturbances. The controller is insensitive to parameter variations. It also demonstrates that the four-quadrant torque controller proposed in the Chapter 5 is suitable for application requiring high-dynamic performance, such as servo control.

7 Conclusions and Future Research

This thesis focuses on the design and performance optimisation of SRMs. The aims are to simulate the performances, reduce torque ripple outputs, and derive a motion control solution of SRMs. In order to realise optimisation study, this thesis proposes a computer simulation model and an online instantaneous torque estimator for general multi-phase SRMs as a platform for performance analysis. It also develops a torque controller and a position controller. This chapter concludes the main contributions and findings of this thesis with suggestions for possible areas of future research on SRM.

7.1 Computer simulation model

A computer simulation model combining both circuit and signal oriented approach is developed under MATLAB/SimPowerSystems environment. The magnetic non-linearities among rotor position, phase current, flux-linkage and torque are simulated. Mutual couplings between phases are also taken into account. Mechanical system of SRM is also simulated. User inputs the magnetic data and basic mechanical parameters of the machine, and configures the power drive and control algorithm using the graphical user interface provided by MATLAB/Simulink. The simulator allows the users to visualise variables, which are difficult or impossible to be measured during experiments, such as flux-linkage, co-energy, phase torque outputs and torque ripples. The simulation results of the simulation model are found to be accurately matching experimental measurements.

The proposed model requires neither manual translation of power electronic circuit into signal flow diagram, nor conversion of digital controller into equivalent electronic circuit, which is however necessary for traditional simulation models that use either circuit or signal oriented model. In fact, the simulation model provides convenient means to develop and evaluate the performances of power drive and control algorithm via computer simulation before the implementation of hardware prototype.

7.2 Online instantaneous torque estimation

For online assessment of torque output and torque ripple, an online instantaneous torque estimation algorithm for SRM with hysteresis current control is presented. Based only on a few pre-measured machine data and machine terminal quantities, the co-energy of each phase is estimated online. The stored data are used to estimate the instantaneous torque using the principle of co-energy. As the estimation of co-energy takes care of magnetic saturation, the torque estimator can function in both unsaturated and saturating regions. Simulation results show that the torque outputs of the proposed estimator are in good agreement with those obtained with cubic spline model.

Comparing with conventional torque estimators, the proposed algorithm reduces the amount of premeasured magnetic data, while the accuracy of the outputs is similar. Thus, the requirement of computer memory space is reduced. As the algorithm requires little mathematical manipulation, it is suitable for online operation.

7.3 Instantaneous torque control based on co-energy control

This thesis also presents an instantaneous torque controller based on co-energy control for the purpose of torque ripple reduction. A one-dimensional co-energy profile is first developed from pre-measured low-current magnetic characteristics offline. It is applied to both unsaturated and saturated regions to calculate the required co-energy for the desired torque. As described earlier, the co-energy is controlled to track the command. Simulation and experiment results verify the effectiveness of the controller in instantaneous torque control and ripple reduction.

The torque controller is then further developed for four-quadrant operation. According to the direction of torque command, the relative rotor position of each phase is calculated. Hence, the direction and magnitude of the torque output can be controlled. Simulation and laboratory measurements show that the SRM can produce outputs with reduced torque ripples according to the torque command in both motoring and generating modes, using the control algorithm.

The proposed torque controller involves relatively few premeasured magnetic data. The computational burden is also light. In contrast to conventional current-profiling scheme, the co-energy controller simplifies the tuning of parameters of the feedback controller. It is because the effect of phase inductance on the gain of the control process is greatly reduced.

7.4 Position control

A rotor position control algorithm is developed on top of the four-quadrant torque control scheme. With the knowledge of basic machine parameters, the position controller is designed using the principles of 2-degree of freedom internal model control. Simulations and experiments prove that the controller can stably control the rotor position to track the position command, while rejecting external disturbances. It is also robust against variation of machine parameters.

With the proposed algorithm, the design problem of the controller is simplified to the selection of response time constants, because of the use of internal model control. In fact, the parameters of the controller are expressed in terms of basic machine parameters or the time constants. No feedforward is necessary as the control can automatically eliminate the effect of disturbance. In addition, the implementation of the controller is simple in that it only requires a few online computations.

7.5 Suggestion for future research

Although the algorithms proposed in this thesis output promising performances of SRM, especially in torque ripple reduction and motion control, there are rooms for further investigations and improvement.

7.5.1 Self-tuning position controller

Even though the position controller proposed in this thesis is robust against variations of machine parameters, it is necessary to set the parameters of the controller according to machine characteristics. Obviously, an automatic tuning scheme for the controller is preferred. A self-tuning controller can also be developed for rotor position control. The scheme should be able to estimate the machine parameters online and then set the controller parameters accordingly. With such feature, the efforts of the user to measure and input the parameters of the machine during commissioning and maintenance would be reduced substantially. Possible algorithms of the tuning scheme are genetic algorithm and adaptive control.

7.5.2 Position sensorless algorithm

The schemes presented in this thesis require a rotary encoder to acquire the information about rotor position. To enhance the robustness and reduce the cost of system hardware, the rotary encoder can be replaced by the use of a sensorless algorithm which estimates the rotor position based on machine magnetic characteristics, terminal flux linkage and current.

7.5.3 Optimisation in high speed region and for efficiency

This thesis focuses on the optimisations of performances in low speed operations and position control. However, SRM often operates in both low speed and high speed regions. Further investigation in optimising the performance of SRM in the high speed region is possible. In this region, SRM cannot be controlled via voltage control, as the back EMF is higher than the supply voltage. Instead, only the turn on and turn off angles can be altered.

The efficiency of SRM has not been studied explicitly in this thesis. However, energy efficiency is gaining attention in recent years, because of the rise of oil price and global warming. As the efficiency of SRM is dependent on many factors, such as conduction angle, current profile, switching scheme and circuit topology, the study of it is a topic of its own. Possible research directions are efficiency optimisation via electronic control, machine geometrical design and the use of efficient power electronic circuit.

7.5.4 DSP and FPGA implementation

The digital controllers of the experiments of this thesis are realised with dSpace controller board. Although it offers a wealth of useful features, such as PWM outputs and analogue-to-digital converters, its computational power barely meets the requirements of real-time machine control. It may hinder the development of more superior control and sensorless algorithms. For future development, advanced digital signal processors (DSP) or field programmable gate arrays (FPGA), which are now widely used in industries, can be applied. The beauty of these new controllers is that they all can implement digital control algorithms with a high sampling rate. FPGA even possesses parallel processing capability which is needed for sensorless control.

8 Appendices

8.1 Acquisition of magnetic characteristics

The flux linkage data of the 8/6 motor are evaluated using a voltage pulse method. The flow chart of the measurement is shown in Fig. 8.1. While the rotor is mechanically secured at a known position, a voltage pulse is applied to a phase winding via IGBTs for 40 ms. The voltage across and the current through the winding are measured via, respectively, a differential voltage amplifier and a LEM current sensor. Both the voltage and current signals picked up are amplified via signal conditioning circuits and these signals are acquired by a digital signal processor (DSP) card dSpace 1102 once every 1 ms. The flux is calculated according to (2.1) to give the self-flux - current characteristic at various rotor positions. Since the application of voltage and current lasts only for a very short period, the temperature rise of the winding is small and the resistance is assumed constant. After allowing the SRM to cool down, the measurement is repeated for different positions between 0° and 30° at 2.5° interval (Fig. 8.2). Because of the symmetry about the aligned position, the measured data are mirrored along 30° to reproduce the data between 30° and 60°. As for other phases, the data are similar, but have a 15° phase shift between phases.

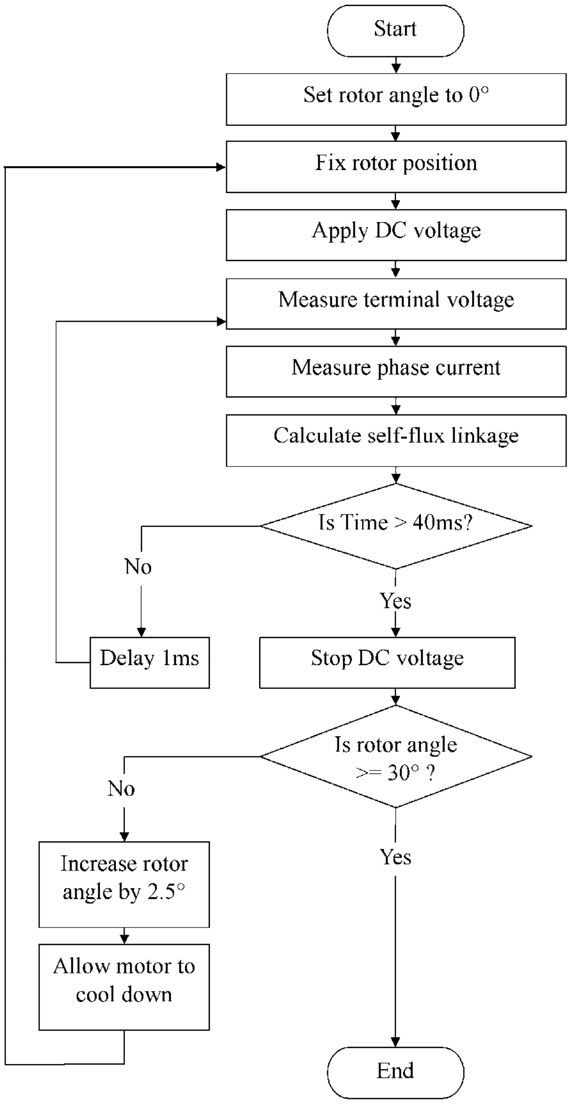

Fig. 8.1 Flow chart of self-flux linkage measurement

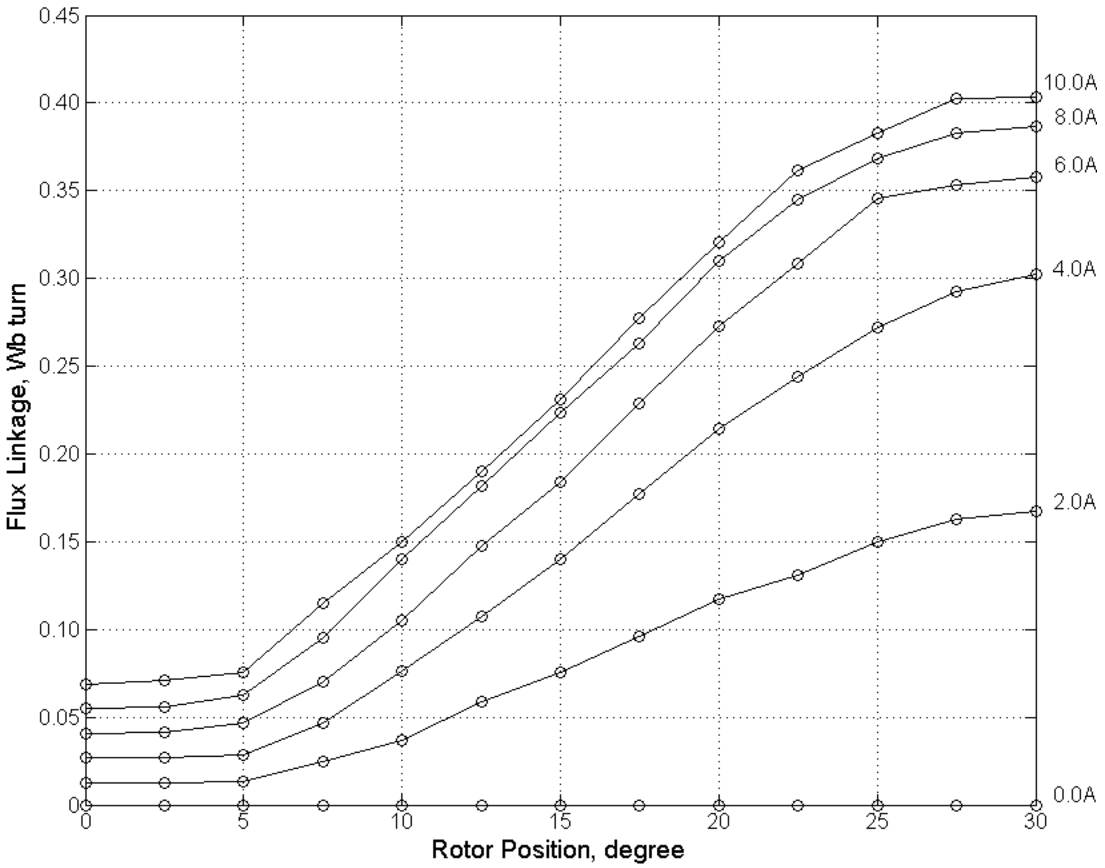

Fig. 8.2 Self-flux linkage characteristics

If the measured value contains significant noise the data should be smoothened, using curve fitting techniques such as cubic smoothing spline, before the data are being stored in look-up tables for subsequent simulation. For the motor being studied, such data smoothing procedure is not implemented because the measured data are found to be sufficiently smooth.

It should be noted that the voltage drop on connector leads, which is about several millivolts, may affect the accuracy measurement. To minimise the associated error, the magnitude of the applied voltage pulse should be substantially higher than the voltage drop. In this measurement, the applied voltage is more than 6 V, so the error due to voltage drop becomes negligible.

As for mutual-flux linkage, a similar setup is used. Fig. 8.3 shows the flow chart of the measurement. During the measurement, one phase is excited by a voltage pulse and the current flowing in this phase as well as the induced open circuit voltage in the other phases is measured. The measured voltage is integrated to give the flux linkage:

$$\lambda_{jk} = \int v_j \, dt \tag{8.1}$$

where λ_{jk} represents the mutual flux linkage of phase j due to the current in phase k, v_j denotes the applied voltage on phase j. By repeating the measurement, the mutual-flux linkage – current relationship between 0° and 60° is obtained (Fig. 8.4).

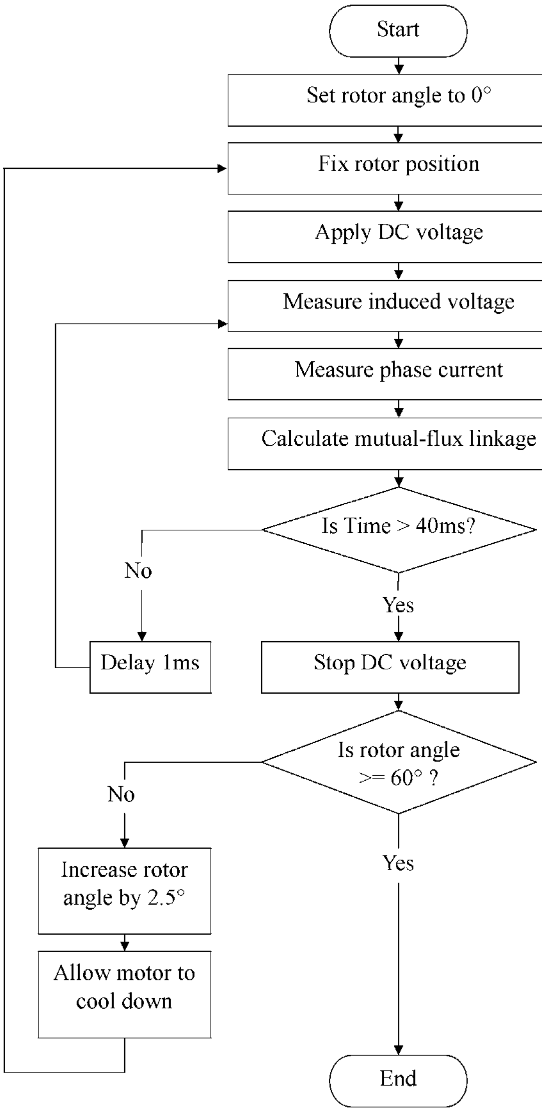

Fig. 8.3 Flow chart of mutual-flux linkage measurement

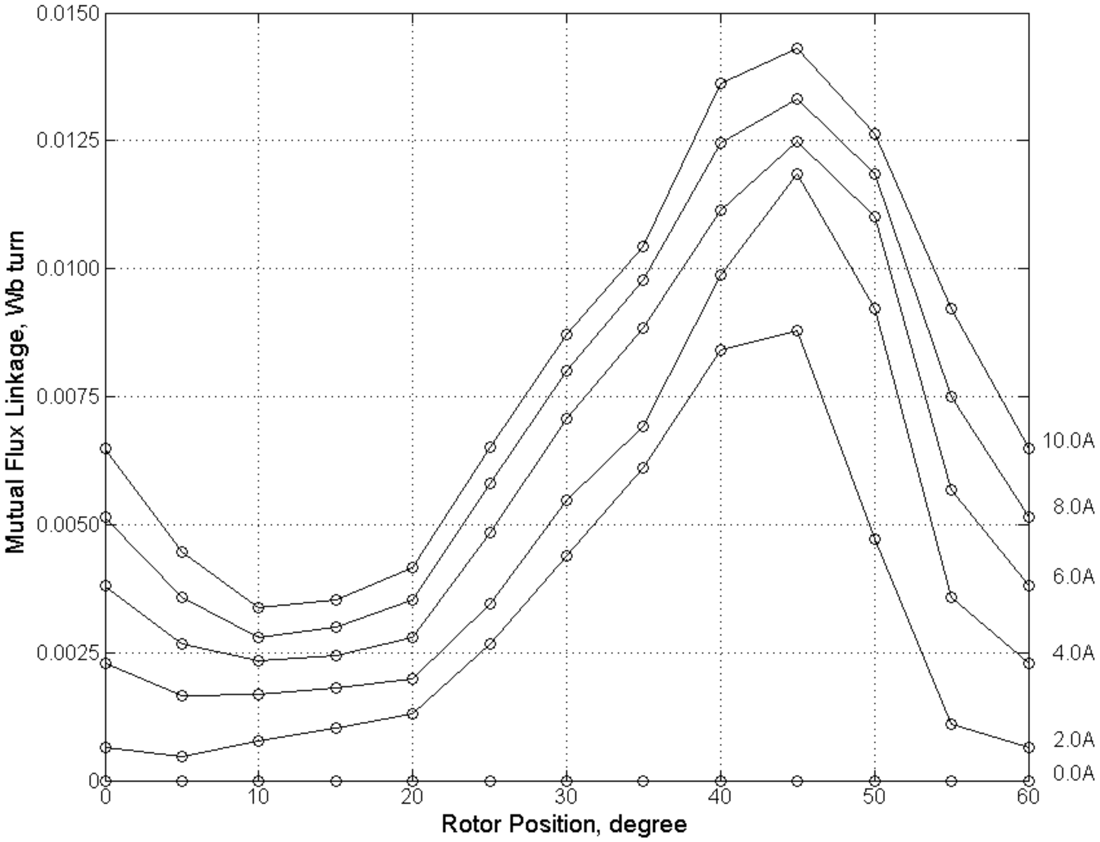

Fig. 8.4 Mutual-flux linkage of phase 2 with exciting current in phase 1

8.2 Hardware prototype of SRM controller

The schematic diagrams of the sensor board, power drive, connection cable and wiring are illustrated in Fig. 8.5 to Fig. 8.8. Print circuit boards (PCBs) are designed and assembled for the sensor board and power drive. The sensor board consists of transducers and amplifiers, which sense the phase currents and DC-link voltage of a 4-phase SRM, and amplify the signals. The signals are then fed to the dSpace 1104 controller board. To obtain information about rotor position, a 1000 count/rev incremental rotary encoder is coupled to the SRM. With some interfacing circuit, the outputs of the encoder are connected to the controller board. The power drive is made up of four independent asymmetric half bridges, each of which is connected to the phase winding of SRM. The power electronic switches of the power drive are controlled by switching signals from dSpace 1104.

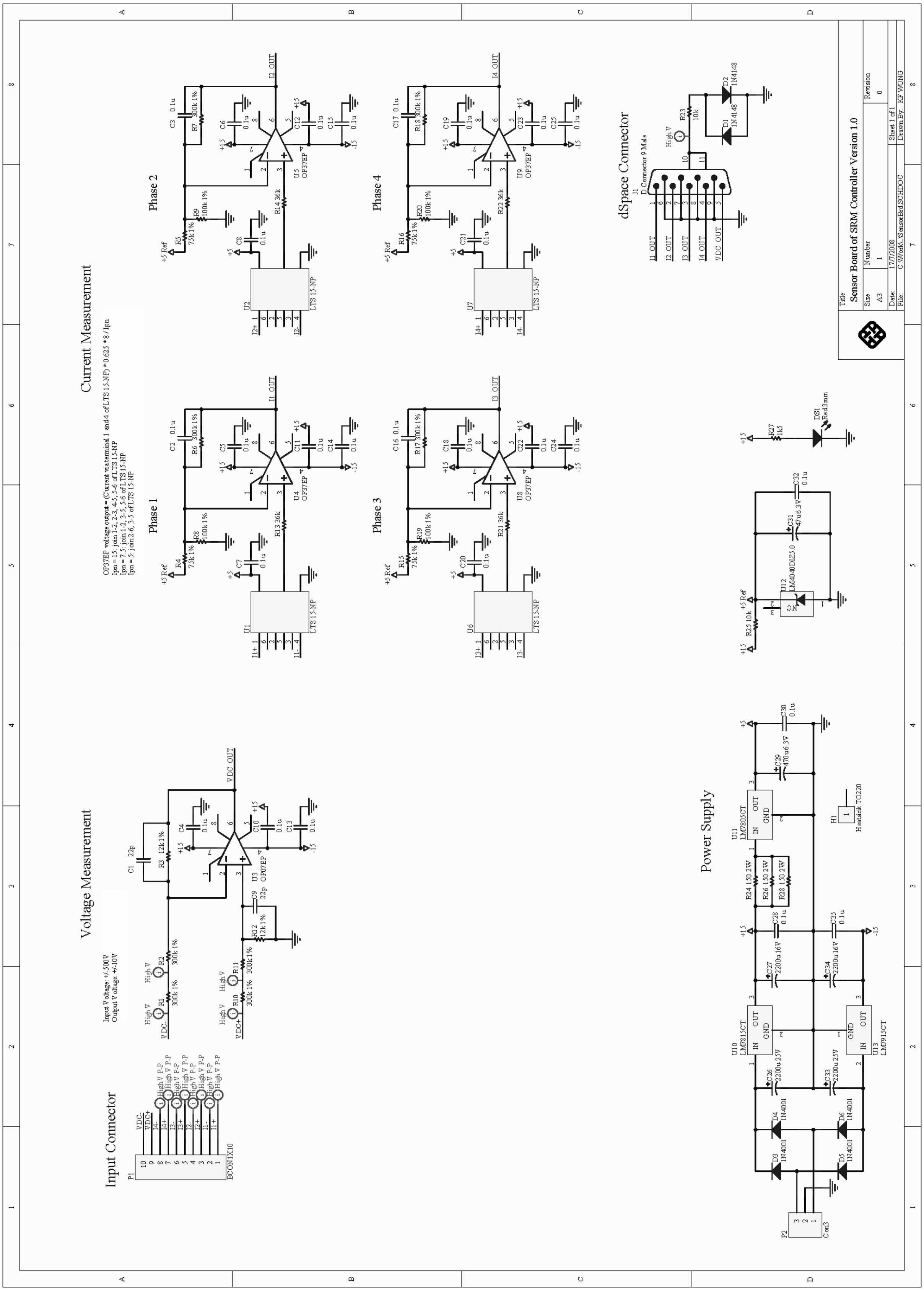

Fig. 8.5 Schematic of sensor board

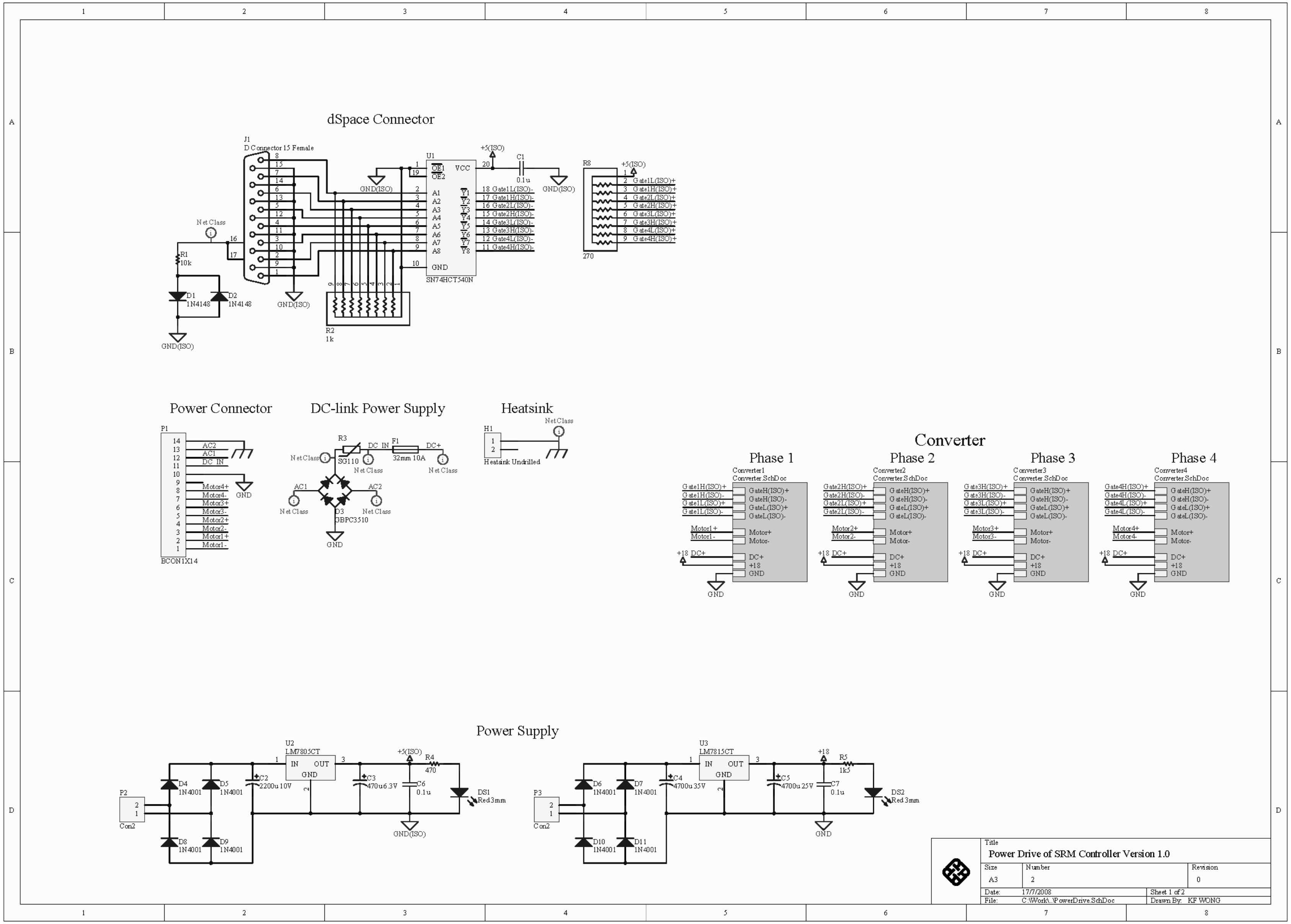
dSpace Connector
J1
D Connector 15 Female
U1
SN74HCT540N
VCC
GND
+5(ISO)
GND(ISO)
C1
0.1u
R8
270
Gate1L(ISO)+
Gate1H(ISO)+
Gate2L(ISO)+
Gate2H(ISO)+
Gate3L(ISO)+
Gate3H(ISO)+
Gate4L(ISO)+
Gate4H(ISO)+
Gate1L(ISO)-
Gate1H(ISO)-
Gate2L(ISO)-
Gate2H(ISO)-
Gate3L(ISO)-
Gate3H(ISO)-
Gate4L(ISO)-
Gate4H(ISO)-
Net Class
R1
10k
D1
1N4148
D2
1N4148
R2
1k
Power Connector
P1
BCON1X14
AC2
AC1
DC IN
Motor4+
Motor4-
Motor3+
Motor3-
Motor2+
Motor2-
Motor1+
Motor1-
DC-link Power Supply
R3
SG110
F1
32mm 10A
DC+
D3
GBPC3510
Heatsink
H1
Heatsink Undrilled
Converter
Phase 1
Phase 2
Phase 3
Phase 4
Converter1
Converter.SchDoc
Converter2
Converter3
Converter4
GateH(ISO)+
GateH(ISO)-
GateL(ISO)+
GateL(ISO)-
Motor+
Motor-
DC+
+18
Power Supply
P2
Con2
P3
D4
D5
D6
D7
D8
D9
D10
D11
1N4001
U2
LM7805CT
U3
LM7815CT
IN
OUT
C2
2200u 10V
C3
470u 6.3V
C4
4700u 35V
C5
4700u 25V
C6
0.1u
C7
0.1u
R4
470
R5
1k5
DS1
DS2
Red 3mm
Title
Power Drive of SRM Controller Version 1.0
Size
A3
Number
2
Revision
0
Date:
17/7/2008
Sheet 1 of 2
File:
C:\Work\..\PowerDrive.SchDoc
Drawn By:
KF WONG

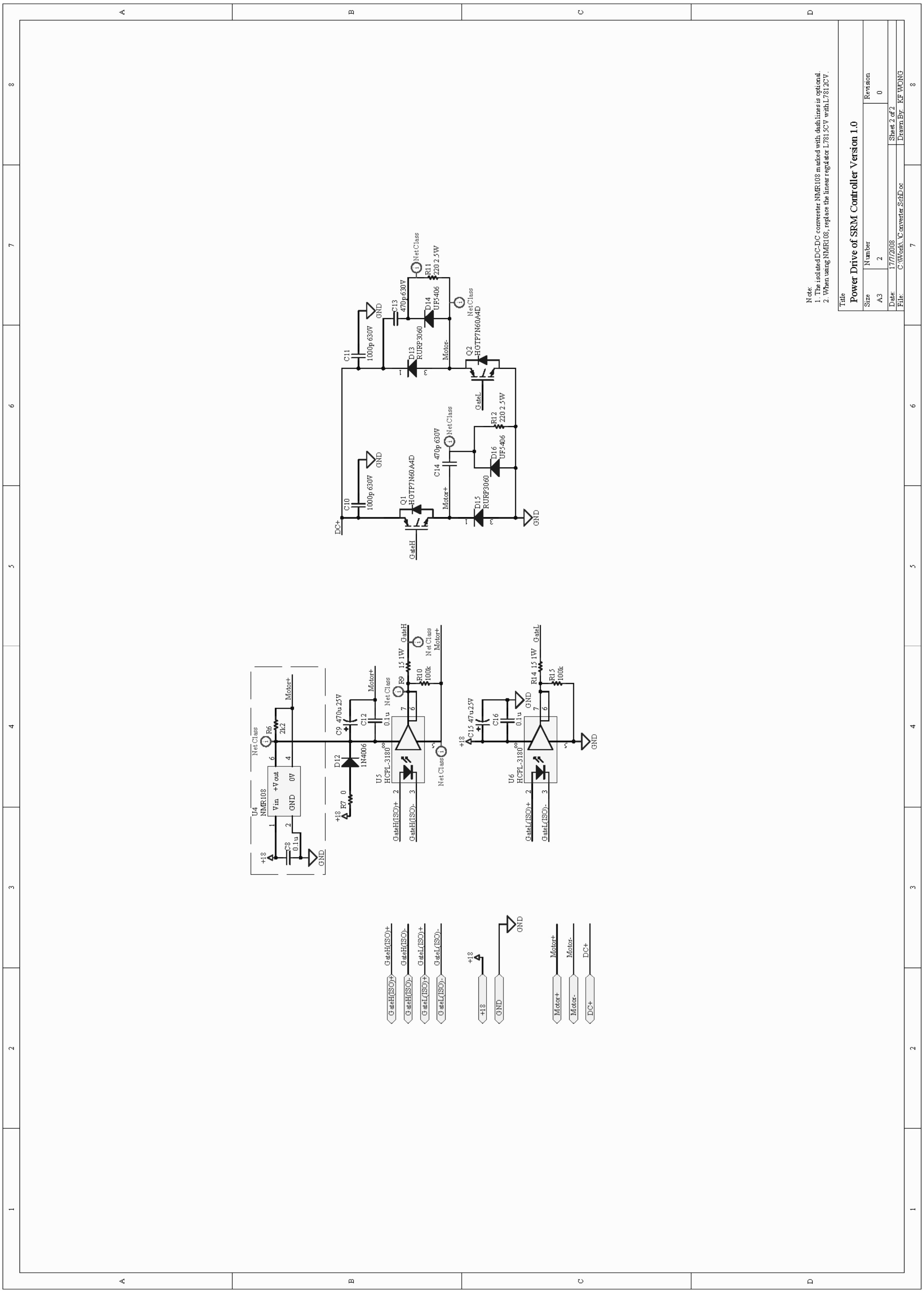

Fig. 8.6 Schematic of power drive

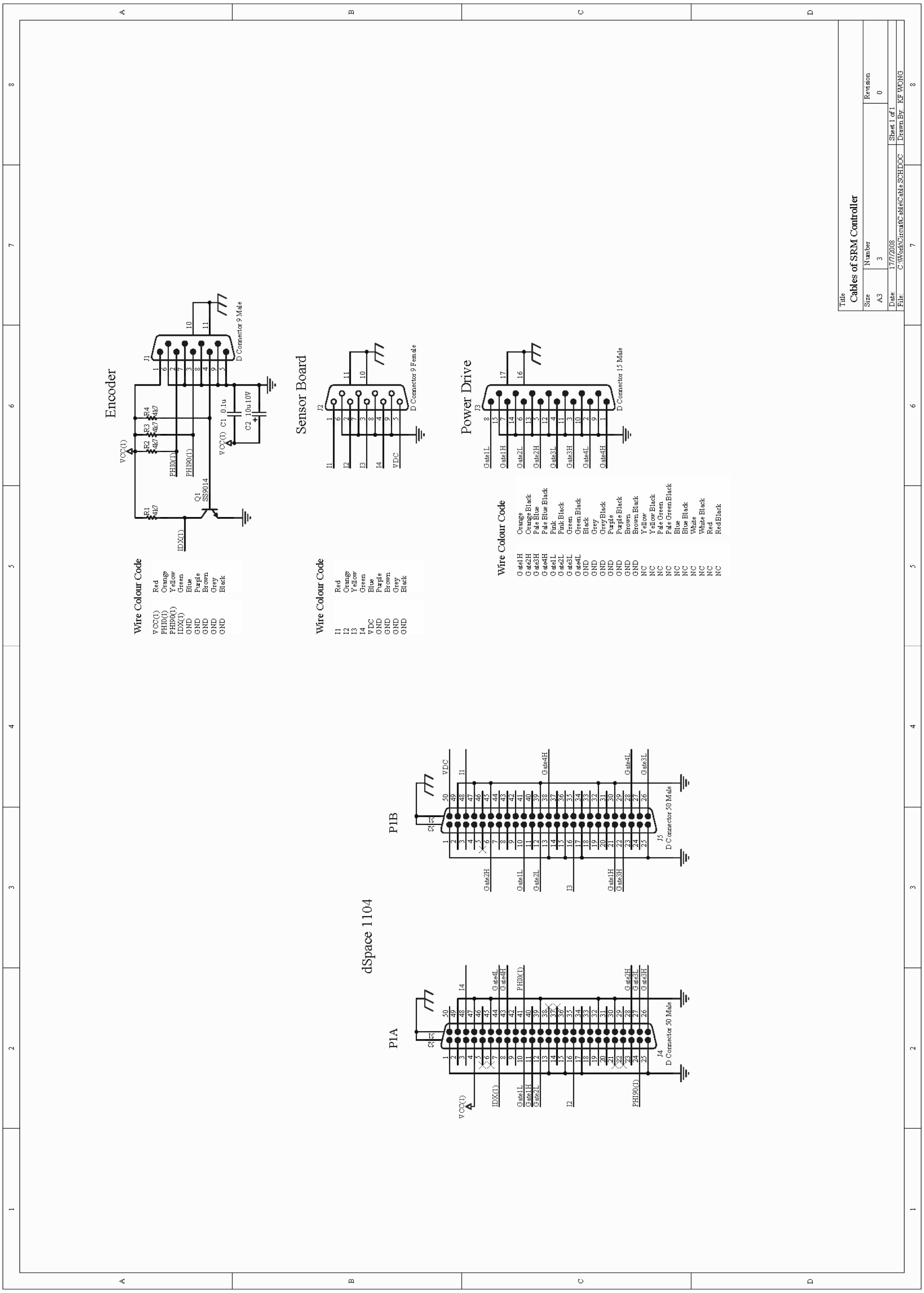

Fig. 8.7 Schematic of connection cable

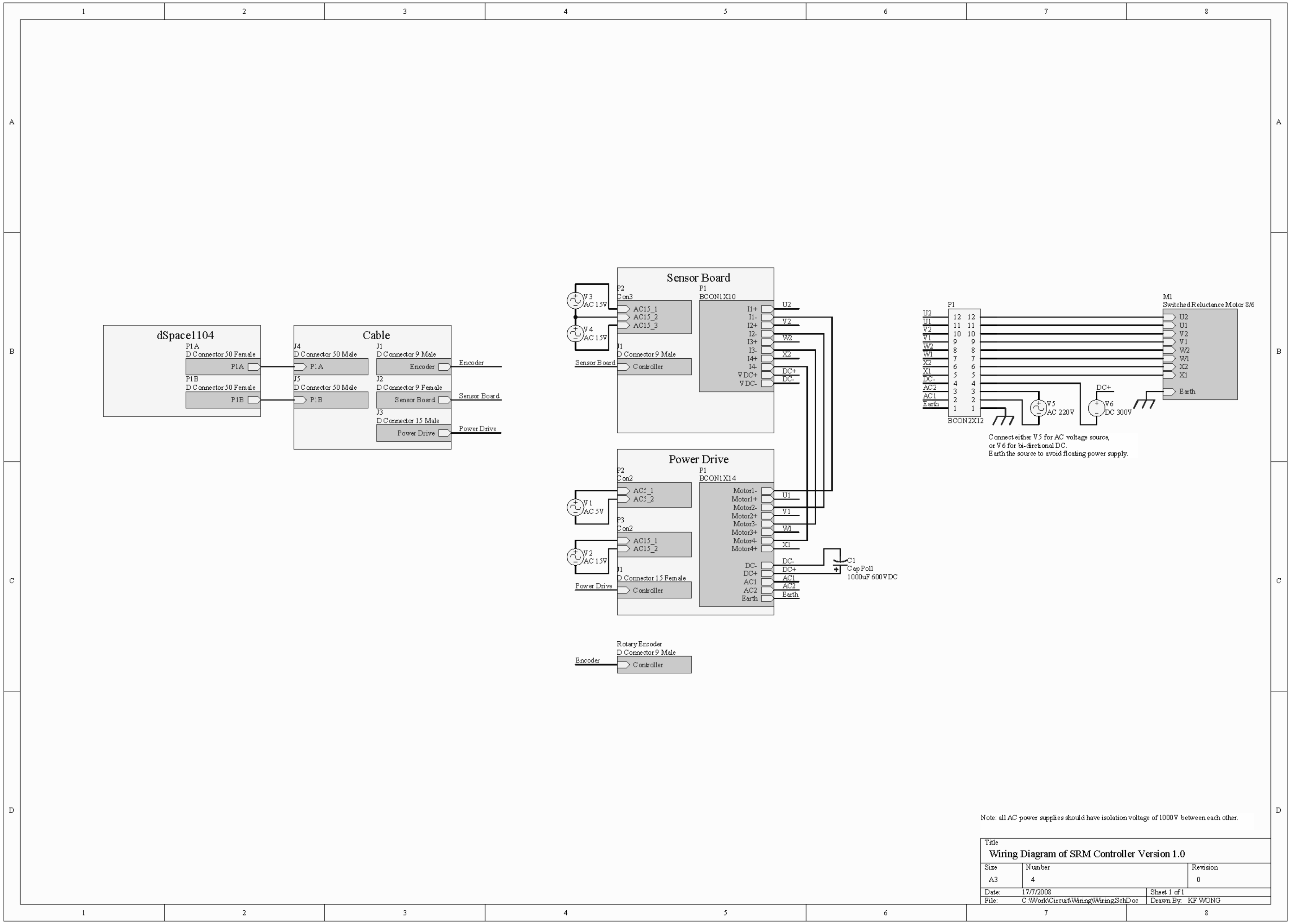

Fig. 8.8 Wiring diagram

9 References

[1] Miller, T. J. E.: ‘Switched reluctance motors and their control’ (Magna Physics Publishing, 1993)

[2] Anderson, A. F.: ‘Development history’, in Miller T. J. E. (Ed.): ‘Electronic Control of Switched Reluctance Machines’ (Newnes, 2001), pp. 6–33

[3] Bose, B. K. Miller, T. J. E., Szczesny, P. M., and Bicknell, W. H.: ‘Microcomputer control of switched reluctance motor’, *IEEE Trans. on Ind. Appl.*, 1986, **IA-22**, (4), pp. 708–715

[4] Bose, B. K., and Latham N. Y.: ‘Control system for switched reluctance motor’. United States Patent 4707650, November 1987

[5] Stephenson, J. M., and Blake, R. J.: ‘The design and performance of a range of general-purpose industrial SR drives for 1 kW to 110 kW’. Conference Record of the 1989 IEEE Industry Applications Society Annual Meeting, San Diego, United States, 1–5 Oct 1989, pp. 99–107

[6] Cossar, C., and Miller T. J. E.: ‘Application experience in switched reluctance motor control using ASIC technology’. IEE Colloquium on ASIC Technology for Power Electronics Equipment, London, United Kingdom, 20 Feb 1992, pp. 5/1–5/4

[7] Fuengwarodsakul, N. H., Radermacher, H., and De Doncker, R.W.: 'Rapid prototyping tool for switched reluctance drive controls in traction applications'. The Fifth International Conference on Power Electronics and Drive Systems, 2003, Singapore, 17–20 Nov. 2003, pp. 927

[8] Cossar, C., and Kelly, L.: 'Drive development and test', in Miller T. J. E. (Ed.): 'Electronic Control of Switched Reluctance Machines' (Newnes, 2001), pp. 201–226

[9] Krishnan, R.: 'Switched reluctance motor drives: modeling, simulation, analysis, design, and applications' (CRC, 2001)

[10] Miller, T. J. E.: 'Brushless permanent-magnet and reluctance motor drives' (Oxford Science Publications, 1989, Reprint, 1993)

[11] Miller, T. J. E.: 'Electromagnetic energy conversion', in Miller T. J. E. (Ed.): 'Electronic Control of Switched Reluctance Machines' (Newnes, 2001), pp. 34–61

[12] DiRenzo, M. T., Masten, M. K., and Cole, C. P.: 'Switched reluctance motor control techniques'. Proceedings of the 1997 American Control Conference, Albuquerque, United States, 4–6 Jun. 1997, pp. 272–277

[13] Rizzo, M., Savini, A., and Turowski, J.: ‘3-D finite element analysis of a linear reluctance motor by using difference scalar potential’, *IEEE Trans. on Magnet.*, 1996, **32**, (3), pp. 1533–1536

[14] Benhama, A., Williamson, A. C., and Reece, A. B. J.: ‘Force and torque computation from 2-D and 3-D finite element field solutions’, *IEE Proc. Electr. Power Appl.*, 1989, **146**, (1), pp. 25–31

[15] Preston, M. A., and Lyons, J. P.: ‘A switched reluctance motor model with mutual coupling and multi-phase excitation’, *IEEE Trans. on Magnet.*, 1991, **27**, (6), pp. 5423–5425

[16] Miller, T. J. E.: ‘Optimal design of switched reluctance motors’, *IEEE Trans. on Ind. Electron.*, 2002, **49**, (1), pp. 15–27

[17] Koibuchi, K., Ohno, T., and Sawa, K.: ‘A basic study for optimal design of switched reluctance motor by finite element method’, *IEEE Trans. on Magnet.*, 1997, **33**, (2), pp. 2077–2080

[18] Pan, J. F.: ‘A 2D variable reluctance planar motor’. PhD thesis, The Hong Kong Polytechnic University, 2006

[19] Xue, X. D., Cheng, K. W. E., and Ho, S. L.: ‘Simulation of switched reluctance motor drives using two-dimensional bicubic spline’, *IEEE Trans. on Energy Conversion*, 2002, **17,** (4), pp. 471–477

[20] Xue, X. D., Cheng, K. W. E., and Ho, S. L.: ‘An algorithm for solving initial value problems of multiphase switched reluctance motors taking into account of mutual coupling’, *Elec. Power Comp. Syst.*, 2002, **30,** (7), pp. 637–651

[21] Miller, T. J. E.: ‘Nonlinear theory of the switched reluctance motor for rapid computer-aided design’ *IEE Proc. B Electr. Power Appl.*, 1990, **137**, (6), pp. 337–347

[22] Mahdavi, J., Suresh, G., Fahimi, B., and Ehsani, M.: ‘Dynamic modeling of nonlinear SRM drive with Pspice’. Conference Record of the 1997 IEEE Industry Applications Conference, 1997, Thirty-Second IAS Annual Meeting, New Orleans, Louisiana, United States, 5–9 Oct. 1997, pp. 661–667

[23] Ichinokura, O., Onda, T., Kimura, M., Watanabe, T., Yanada, T., and Guo, H. J.: ‘Analysis of dynamic characteristics of switched reluctance motor based on SPICE’, *IEEE Trans. on Magnet.*, 1998, **34**, (4), pp. 2147–2149

[24] Rolim, L. G. B., Suemitsu, W. I., Watanabe, E. H., and Hanitsch, R.: ‘Development of an improved switched reluctance motor drive using a soft-switching converter’, *IEE Proc. Electr. Power Appl.*, 1999, **146**, (5), pp. 488–494

[25] Franceschini, G., Pirani, S., Rinaldi, M., and Tassoni, C.: ‘SPICE-assisted simulation of controlled electric drives: an application to switched reluctance drives’, *IEEE Trans. on Ind. Appl.*, 1991, **27**, (6), pp. 1103–1110

[26] Moson, I., Iwan, K., and Nieznanski, J.: ‘Circuit-oriented model of the switched reluctance motor for drive systems simulation’. IEEE 2002 28th Annual Conference of the Industrial Electronics Society, Sevilla, Spain, 5–8 Nov. 2002, pp. 497–501

[27] Yeung, Y. P. B.: ‘Resonant switched reluctance motor drive and its power conditioning with switched-capacitor techniques’. PhD thesis, The Hong Kong Polytechnic University, 2004

[28] Cao S., and Tseng, K. J.: ‘Dynamic modeling of SRM including neighboring phase coupling effects’, *Electr. Mach. And Power Sys.*, 2000, **28**, (12), pp. 1141–1163

[29] Henao, H., Capolino, G. A., Bassily, E., and Poloujadoff, M.: ‘Current control algorithms for switched reluctance machine servo drive’, *Electr. Power Comp. Sys.*, 1998, **26**, (10), pp. 1019–1033

[30] Rajapakse, A. D., Gole, A. M., and Muthumani, D.: ‘Development and interfacing of a generic switched reluctance motor model for an EMTP’. Canadian Conference on Electrical and Computer Engineering 2004, Niagara Falls, Ontario, Canada, 2–5 May 2004, pp. 237–240

[31] Schulz, S. E., and Rahman, K. M.: ‘High-performance digital PI current regulator for EV switched reluctance motor drives’, *IEEE Trans. on Ind. Appl.*, 2003, **39**, (4), pp. 1118–1126

[32] Chi, H. P., Lin, R. L., and Chen, J. F.: ‘Simplified flux-linkage model for switched-reluctance motors’, *IEE Proc. Electr. Power Appl.*, 2005, **152**, (3), pp. 577–583

[33] Soares, F., and Costa Branco, P. J.: ‘Simulation of a 6/4 switched reluctance motor based on Matlab/Simulink environment’, *IEEE Trans. on Aerospace and Elec. Syst.*, 2001, **37**, (3), pp. 989–1009

[34] Chancharoensook, P., and Rahman, M. F.: ‘Dynamic modeling of a four-phase 8/6 switched reluctance motor using current and torque look-up tables’. IEEE 2002 28th Annual Conference of the Industrial Electronics Society, Sevilla, Spain, 5–8 Nov. 2002, pp. 491–496

[35] Kim, C. C., Hur, J., and Hyun, D. S.: ‘Simulation of a switched reluctance motors using Matlab/M-file’. IEEE 2002 28th Annual Conference of the Industrial Electronics Society, Sevilla, Spain, 5–8 Nov. 2002, pp. 1066–1071

[36] Xie, D., Yan, X., and Zhang, Y: ‘A direct field-circuit-motion coupled modeling of switched reluctance motor’, *IEEE Trans. on Maget.*, 2004, **40**, (2), pp. 573–576

[37] Xu, L., and Ruckstadter, E.: ‘Direct modeling of switched reluctance machine by coupled field-circuit method’, *IEEE Trans. on Energy Conversion*, 1995, **10**, (3), pp. 446–454

[38] Kamper, M. J., Rasmeni, S. W., and Wang, R. J.: ‘Finite-element time-step simulation of the switched reluctance machine drive under single pulse mode operation’, *IEEE Trans. on Maget.*, 2007, **43**, (7), pp. 3202–3208

[39] Geldhof, K. R., Vyncke, T. J., De Belie, F. M. L. L., Vandevelde, L., Melkebeek, J. A. A., and Boel, R. K.: ‘Embedded Runge-Kutta methods for the integration of a current control loop in an SRM dynamic finite element model’, *IET Sci. Meas. Technol.*, 2007, **1**, (1), pp. 17–20

[40] Jiang W., Chen B., Liu Q., and Quan, L.: ‘Simulation and analysis of switched reluctance motor applied in the automobile based on Ansoft’, *J. of Agricultural Mechanization Research*, 2005, (3), pp. 271–277 (In Chinese)

[41] Inderka, R. B., and De Doncker, R. W.: ‘High-dynamic direct average torque control for switched reluctance drives’, *IEEE Trans. on Ind. Appl.*, 2003, **39**, (4), pp. 1040–1045

[42] Inderka, R. B., De Doncker, R., and Krehenbrink, M.: ‘On-line estimation of instantaneous torque in switched reluctance machine control’. Proc. of the IEEE International Symposium on Industrial Electronics, Cholula, Puebla, Mexico, 4–8 Dec. 2000, pp. 385–389

[43] Fuengwarodsakul, N. H., Menne, M., Inderka, R. B., and De Doncker, R. W.: ‘High-dynamic four-quadrant switched reluctance drive based on DITC’, *IEEE Trans. on Ind. Appl.*, 2005, **41**, (5), pp. 1232–1242

[44] Sahoo, S. K., Zheng, Q., Panda, S. K., and Xu, J. X.: 'Model-based torque estimator for switched reluctance motors'. The Fifth International Conference on Power Electronics and Drive Systems, Singapore, 17–20 Nov. 2003, pp. 959–963

[45] Stiebler, M., and Liu K.: 'An analytical model of switched reluctance machines', *IEEE Trans. on Energy Conversion*, 1999, **14**, (4), pp. 1100–1107

[46] Torrey, D. A., Niu, X. M., and Unkauf, E. J.: 'Analytical modelling of variable-reluctance machine magnetisation characteristics', *IEE Proc. Electr. Power Appl.*, 1995, **142**, (1), pp. 14–22

[47] Ramamurthy, S. S., and Balda, J. C.: 'Intelligent and adaptive on-line direct electromagnetic torque estimator for switched reluctance motors based on artificial neural networks'. IEEE International Electric Machines and Drives Conference, Cambridge, Massachusetts, United States, 17–20 Jun. 2001, pp. 826–830

[48] Wallace, R. S., and Taylor, D. G.: 'Low-torque-ripple switched reluctance motors for direct-drive robotics', *IEEE Trans. Robotics and Automation*, 1991, **7**, (6), pp. 733–742

[49] Luk, P. C. K., and Jinupun, K. P.: 'Direct work control for a three-stack switched reluctance motor'. IEEE 36th Conference on Power Electron. Specialists 2005, Recife, Brazil, 12–18 Jun. 2005, pp. 2462–2466

[50] Schramm, D. S., Williams, B. W., and Green, T. C.: ‘Optimum commutation-current profile on torque linearization of switched reluctance motors’. Proc. Int. Conference on Electrical Machines, Manchester, United Kingdom, Sep. 1992, pp. 484–488

[51] Stankovic, A. M., Tadmor, G., Coric, Z. J., and Agirman, I.: ‘On torque ripple reduction in current-fed switched reluctance motors’, *IEEE Trans. Ind. Electron.*, 1999, **46**, (1), pp. 177–183

[52] Ishikawa, H., Wang, D., and Naitoh, H.: ‘A new switched reluctance motor drive circuit for torque ripple reduction’. Proc. of the Power Conversion Conference 2002, Osaka, Japan, Apr. 2002, pp. 683–688

[53] Husain I., and Ehsani, M.: ‘Torque ripple minimization in switched reluctance motor drives by PWM current control’, *IEEE Trans. Power Electron.*, 1996, **11**, (1), pp. 83–88

[54] Islam, M. S., and Husain, J.: ‘Torque-ripple minimization with indirect position and speed sensing for switched reluctance motors’, *IEEE Trans. Ind. Electron.*, 2000, **47**, (5), pp. 1126–1133

[55] Hossain, S., Husain, I., Klode, H., Lequesne, B., and Omekanda, A.: ‘Four-quadrant control of a switched reluctance motor for a highly dynamic actuator load’. Seventeenth Annual IEEE Applied Power Electronics Conference and Exposition 2002, Dallas, United States, Mar. 2002, pp. 41–47

[56] Moreira, J. C.: ‘Torque ripple minimization in switched reluctance motors via bi-cubic spline interpolation’. Proc. IEEE Power Electron. Specialists Conference 1992, Cairns, Queensland, Australia, 29 Jun.–1 Jul. 1992, pp. 851–856

[57] Bae, H. K., and Krishnan, R.: ‘A study of current controllers and development of a novel current controller for high performance SRM drives’. Conference Record of the 1996 IEEE Industry Applications Conference 1996, Thirty-First IAS Annual Meeting, San Diego, United States, 6–10 Oct. 1996, pp. 68–75

[58] Russa, K., Husain, I., and Elbuluk, M. E.: ‘A self-tuning controller for switched reluctance motors’, *IEEE Trans. Power Electron.*, 2000, **15**, (3), pp. 545–552

[59] Agirman, I., Stankovic, A. M., Tadmor, G., and Lev-Ari, H.: ‘Adaptive torque-ripple minimization in switched reluctance motors’, *IEEE Trans. Ind. Electron.*, 2001, **48**, (3), pp. 664–672

[60] Ooi, H. S., and Green, T. C.: ‘Sensorless switched reflectance motor drive with torque ripple minimization’. IEEE 31st Annual Power Electron. Specialists Conference 2000, Galway, Ireland, 18–23 June 2000, pp. 1538–1543

[61] Rahman, K. M., Rajarathnam, A. V., and Ehsani, M.: ‘Optimized instantaneous torque control of switched reluctance motor by neural network’. Conference Record of the 1997 IEEE Ind. Appl. Conference, Thirty-Second IAS Annual Meeting, New Orleans, Louisiana, United States, 5–9 Oct. 1997, pp. 556–563

[62] Zhou, Y., Xia, C., He, Z., and Xie X.: ‘Torque ripple minimization in a sensorless switched reluctance motor based on flexible neural networks’. IEEE International Conference on Control and Automation, 2007, Guangzhou, China, 30 May–1 Jun. 2007, pp. 2340–2344

[63] Mir, S., Elbuluk, M. E., and Husain, I.: ‘Torque-ripple minimization in switched reluctance motors using adaptive fuzzy control’, *IEEE Trans. Ind. Appl.*, 1999, **35**, (2), pp. 461–468

[64] Inderka, R. B., and De Doncker, R. W.: ‘DITC-direct instantaneous torque control of switched reluctance drives’, *IEEE Trans. Ind. Appl.*, 2003, **39**, (4), pp. 1046–1051

[65] Neuhaus, C. R., Fuengwarodsakul, N. H., and De Doncker, R. W.: ‘Predictive PWM-based direct instantaneous torque control of switched reluctance drives’. 37th IEEE Power Electron. Specialists Conference 2006, Jeju, South Korea, 18-22 June 2006, pp. 1–7

[66] Lim, H. S., Krishnan, R., and Lobo, N. S.: ‘Design and control of a linear propulsion system for an elevator using linear switched reluctance motor drives’, *IEEE Trans. on Ind. Electron.*, 2008, **55**, (2), pp. 534–542

[67] Chen, C. G., and Liu, T. H.: ‘Nonlinear controller design for switched reluctance drive systems’, *IEEE Trans. on Aerospace and Electron. Syst.*, 2003, **39**, (4), pp. 1429–1440

[68] Pan, J. F., Cheung, N. C., and Yang, J. M.: ‘Auto-disturbance rejection controller for novel planar switched reluctance motor’, *IEE Proc. of Elec. Power Appl.*, 2006, **153**, (2), pp. 307–316

[69] Elmas, C., and Yigit, T.: ‘Genetic algorithm based on-line tuning of a PI controller for a switched reluctance motor drive’, *Elec. Power Comp. Syst.*, 2007, **35**, (6), pp. 675–691

[70] Muniraj, C., and Chandrasekar, S.: ‘Neural network based speed control for 6/4 switched reluctance motor’. International Conference on Computational Intelligence and Multimedia Applications, Sivakasi, Tamil Nadu, 13–15 Dec. 2007. pp. 227–231

[71] Kjaer, P. C., and Gribble, J. J.: ‘Instantaneous torque control’, in Miller T. J. E. (Ed.): ‘Electronic Control of Switched Reluctance Machines’ (Newnes, 2001), pp. 98–132

[72] Kjaer, P. C., Gribble, J. J., and Miller, T. J. E.: ‘High-grade control of switched reluctance machines’, *IEEE Trans. on Ind. Appl.*, 1997, **33**, (6), pp. 1583–1593

[73] Song, G., Sun, H., Huang, L., and Chu, J.: ‘Microstep position control of switched reluctance motors’. The Fifth International Conference on Power Electronics and Drive Systems, Singapore, 17–20 Nov. 2003, pp. 944–947

[74] Pan, J., Cheung, N. C., and Yang, Jinming: ‘High-precision position control of a novel planar switched reluctance motor’, *IEEE Trans. on Ind. Electron.*, **52**, (6), Dec. 2005, pp. 1644–1652

[75] Zhao, S. W., Cheung, N. C., Gan, W. C., Yang, J. M., and Pan, J. F.: ‘A self-tuning regulator for the high-precision position control of a linear switched reluctance motor’, *IEEE Trans. on Ind. Electron.*, **54**, (5), Oct. 2007, pp. 2425–2434

[76] Xue, X. D., Cheng, K. W. E., and Ho, S. L.: ‘Characterization of nonlinearaity using simplified modell for the electromagnetic behaviours of switched reluctance motors’. Sixth International Conference on Advances in Power System Control, Operation and Management, 2003, Hong Kong, China, 11–14 Nov. 2003, pp. 64–69

[77] Visinka R.: ‘3-Phase switched reluctance (SR) sensorless motor control using a 56F80x, 56F8100 or 56F8300 Device’ Application note AN1932, Freescale Semiconductor, 2005, Rev. 2

[78] Visinka R.: ‘Phase resistance estimation for sensorless control of switched reluctance motors’. IEEE 2002 28th Annual Conference of the Industrial Electronics Society, Sevilla, Spain, 5-8 Nov. 2002, pp. 1044-1049

[79] Bozorth R. M.: ‘Ferromagnetism’ (University Microfilms International, 1991), pp. 720

[80] Middleton, R. H., and Goodwin, G. C.: ‘Digital control and estimation: a unified approach’ (Prentice-Hall, 1990), pp. 456–461

[81] Boldea, I.: ‘Electric generators handbook, variable speed generators’ (CRC Press, Taylor & Francis Group, 2006), Chapter 9

[82] Brosilow, C., and Joseph, B.: ‘Techniques of model-based control’ (Prentice Hall PTR, 2002)

[83] Khalil A., and Husain I.: ‘A fourier series generalized geometry-based analytical model of switched reluctance machines’, *IEEE Trans. on Ind. Appl.*, **43**, (3), May.–Jun. 2007, pp. 673–684

[84] Radun A.: ‘Analytically computing the flux linked by a switched reluctance motor phase when the stator and rotor poles overlap’, *IEEE Trans. on Magn.*, **36**, 4, Jul. 2000, pp. 1996–2003